Modelling Geometrical Effects of SOFC Stacks

Pseudo-3D simulation with the GOOSE model

MSc. Thesis Aerospace Engineering:
Power & Propulsion

Aida van de Wetering

Delft University of Technology

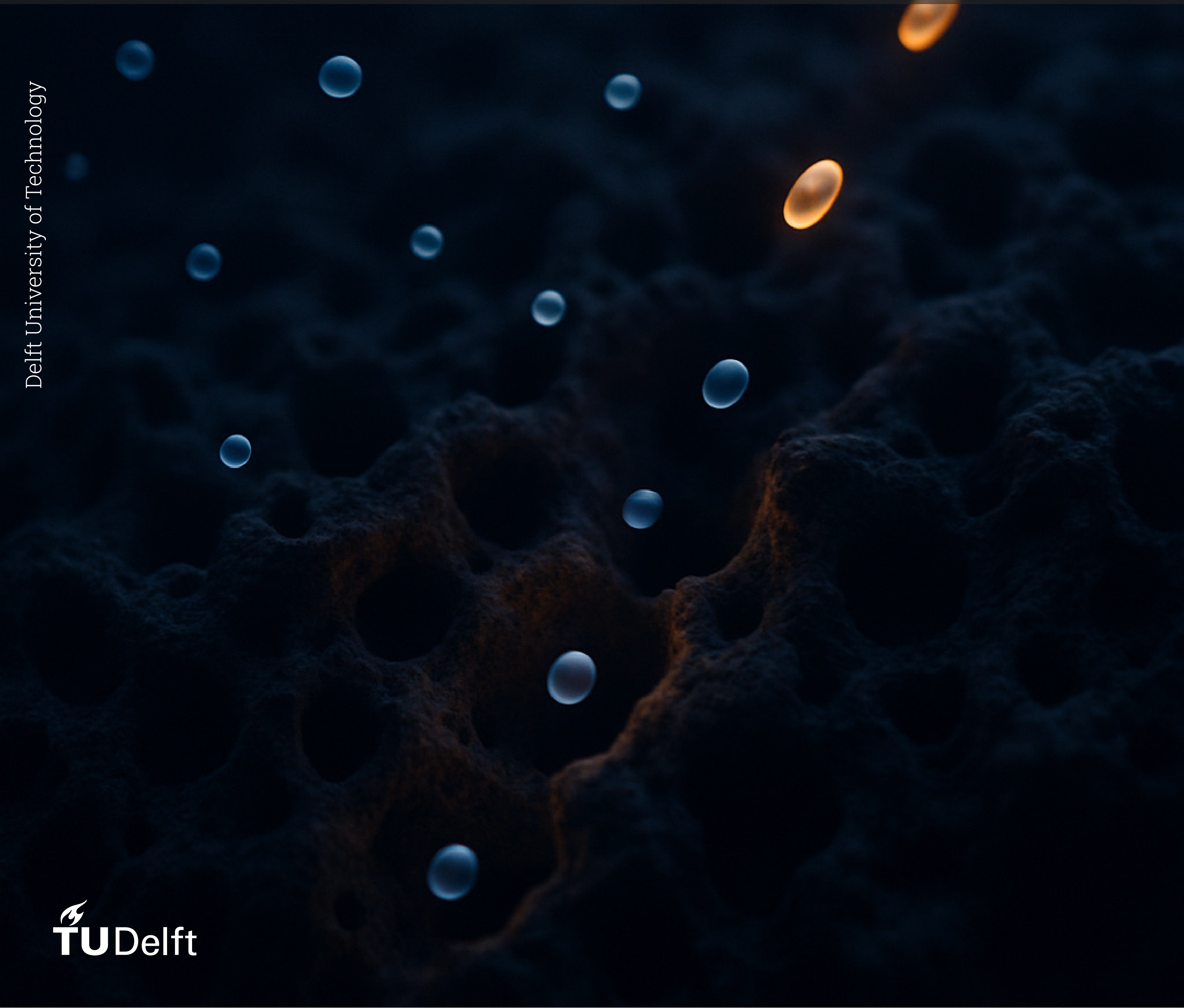

Modelling Geometrical Effects of SOFC Stacks

Pseudo-3D simulation with the GOOSE model

by

Aida van de Wetering

to obtain the degree of Master of Science
at the Delft University of Technology,
to be defended publicly on November 17, 2025 at 14:00.

Project Duration:	December, 2023 - November, 2025	
Faculty:	Faculty of Aerospace Engineering, TU Delft	
Thesis committee:	Prof. A.G. Rao,	TU Delft, supervisor
	Dr. Y. Tang,	TU Delft
	Dr. F. DeDominico	TU Delft

Cover: Impression of an SOFC anode.
(Own work created using Blender)

Abstract

In the search for renewable, alternative propulsion technologies for use in aviation, hybrid SOFC-jet-engine architectures are seen as very promising. The critical performance characteristics for a fuel cell in such an application differ greatly from those currently in use, however: Volumetric power density, fuel utilisation, and operating temperature are key criteria. One way to increase these characteristics is to use novel stack architectures, such as monolithic or tubular arrays. There is a large variation in exact implementations of such architectures, primarily geometrically– the size of fluid channels, skewedness, etc. As a first venture into this design- and optimisation space, a numerical model is developed that enables analysis for arbitrary three-dimensional geometries of SOFC stacks at steady-state conditions, implemented with ease of integration in mind. It is released as open source software for anyone to use. This model was extensively validated and verified, after which it was applied by performing sensitivity analyses on geometry parametrisations for three characteristic geometry classes: planar, tubular and corrugated monolithic. It was found that the stack geometry has only minor effects on the thermal performance, but strong implications on power density and fuel efficiency. Strong variations in the effects of similar changes exist between the different geometries. The core design consideration is also more complicated than a mere trade-off of power density and fuel efficiency, with certain parameters yielding improvements in both factors due to strong coupling of disparate processes. Miniaturisation increases power density for all geometries considered, but it is seen to come with diminishing returns. The results also give insight into the process of stack design itself: as an indicator of volumetric power density, current density alone has proven to be an unreliable indicator, despite being used analogously as such in existing literature.

Preface

To whomever it may concern...

This thesis hatched from a simple idea: that solid oxide fuel cells, if properly designed, might one day take to the skies. With the unique freedom compared to polymer membrane fuel cells in the ability to be freely geometrically shaped in many more ways, a whole new sky of possibilities opens up. Investigations into this fledgeling field have hardly taken off yet however, so new tooling would be a good first step: A tool to simulate different geometries and evaluate their performance — especially in terms of volumetric and gravimetric power density. And thus, GOOSE was born.

Geometric Oxide-cell Operating-point Simulation Environment (GOOSE) began as a small project, but quickly grew into something larger (as geese tend to do).

This thesis is the product of long hours, many failed attempts, fits of plucking my own feathers, turned into small breakthroughs, and a persistent belief that with the right tools (and perhaps a few feathers), we can take a meaningful step toward more efficient, flight-ready energy systems. All in the name of the wild goose chase for a world more in balance with mother earth. After all, our blue sphere is but a small pond, and we must all share the bread.

While this is a serious piece of academic work, I'd be remiss not to acknowledge the odd joy of naming scientific software after a large, occasionally irritable bird. GOOSE has waddled through debugging sessions, flapped through convergence issues, ruffled a few feathers in the mesh generation process, and yes —occasionally laid an egg or two in the form of a `NaN`. But after all that, it found its wings, passed the whole gaggle of tests, and could soar where others could only float.

Every silly goose needs a partner in crime. This work would not have been possible without the support of Jonathan, who did not only make an excellent rubber duck, but generally was always there to help me stay afloat. Without his critical honking, I would not have been able to discern the fowl from the flock. Now that we're giving out thanks- Stella helped with the pretty mesh diagrams seen in the parameter study chapter. Also thanks to Alex and Conor for (not revoking Tilda privilege and) occasionally giving refreshing insights over a cup of tea. The help from Tilda should not be understated either, for snoozing on my lap and keeping me sane over the past two years. A final word of thanks goes out to Arvind for supervising this endeavour.

I hope that the software as well as the results of the little study that follows prove useful to others in the field (or lake), or at the very least, mildly amusing. Either way, thank you for indulging this somewhat silly name –and the serious work that follows. To those who work in simulation, energy systems, or simply appreciate the elegance of a well-designed wing (literal or figurative), I invite you to take a gander, and offer this thesis, together with the GOOSE software, with humility and a touch of feathered humor.

Aida van de Wetering
Delft, October 2025

Contents

Glossary

Acronyms

API	Application Programming Interface. 35, 36, 84
CC	Current Collector. 4, 5, 7, 9, 11, 29, 30, 34, 37, 44, 48, 50, 54, 84, 100
CFD	Computational Fluid Dynamics. 3, 4, 40, 45, 49, 68
DGM	Dusty Gas Model. 70
ETBP	Extended Triple Boundary Point. 56
FFI	Foreign Function Interface. 36
GOOSE	Geometric Oxide-cell Operating-point Simulation Environment. ii, 3–8, 17, 20, 25, 35–37, 39, 40, 45, 49, 52–55, 62, 64, 67–71, 84, 85, 87, 88
HOR	Hydrogen Oxidation Reaction. ix, 16, 19
HYLENA	HYdrogen eLectrical Engine Novel Architecture. 1, 2
LSM	Lanthanum Strontium Manganite. 45, 56, 58
MIEC	Mixed Ion-Electron Conductor. 28
PEN	Positive (electrode)-Electrolyte-Negative (electrode). vi–viii, 4–7, 9–14, 24, 25, 27, 29–33, 37, 44, 46–50, 52–55, 59–62, 64, 67, 70–72, 84, 85, 100
SOFC	Solid Oxide Fuel Cell. vii, ix, 1–5, 7, 16, 19, 22, 23, 26, 34, 40, 42, 51, 52, 54–57, 63, 66, 68, 69, 71, 85
STEM	Science, Technology, Engineering and Mathematics. 35
TBP	Triple Boundary Point. vii, 9, 16, 21, 22, 25–28, 70, 72, 87
XDSM	eXtended Design Structure Matrix. 12–14
YSZ	Yttrium Stabilised Zirconia. viii, 28, 40, 45, 57

List of Symbols

Symbol	Description	Unit
A_n	Area between two neighbouring elements. For the PEN, its thickness times its depth in the Z-axis	m^2

Symbol	**Description**	**Unit**
A_{active}	Active cell area- the surface area of an SOFC (element) orthogonal to the flow that performs a reaction. For an individual element, this is its length along the Z-axis multiplied with its width	m^2
$A_{channel}$	Cross-sectional area of a fluid channel	m^2
C_i	Molar volume fraction of species i in a mixture	
D_p	Average pore diameter of a porous medium	m
$D_{A,B}$	Bulk (binary) diffusion coefficient for a two-component mixture consisting of fluids A and B	$\mathrm{m}^2\,\mathrm{s}^{-1}$
D_{hy}	Hydraulic diameter	m
D^i_{kn}	Knudsen diffusivity due to interactions with a porous medium for species i in a mixture	$\mathrm{m}^2\,\mathrm{s}^{-1}$
E_0	Standard cell potential	V
L_w	Length of an element in the edge direction (x-coordinate), orthogonal to the diffusion direction and the flow direction	m
L_z	Length of an element in the z (flow-wise coordinate) direction	m
M_i	Molecular weight of species i	$\mathrm{g\,mol}^{-1}$
P_{el}	Percolation probability	
P	Static pressure of a fluid (mixture)	Pa
R_x	Electrical resistance experienced inside of an elecrtrode x	Ω
R_{ion}	Ionic resistance experienced by an oxygen ion passing through the electrolyte	Ω
$R_{t,cond}$	Thermal resistance of conductivity between two elements	$\mathrm{W\,K}^{-1}$
$R_{x,hor}$	Electrical resistance orthogonal to the diffusion direction, along the plane of the active cell area for an electrode x of the PEN assembly	Ω
$R_{x,self}$	Electrical resistance experienced due to the short path that an electron has to take through an electrode x from the center at its TBP to the edge of its outer surface	Ω
T	Temperature	K
U_{Nernst}	Nernst potential of an electrochemical cell	V
U_{cell}	Effective voltage generated by a fuel cell, obtained after all the overpotentials have been applied	V
$Z_{el,el}$	Coordinate number for percolation theory	
ΔG	Gibbs free energy of a reaction	$\mathrm{J\,mol}^{-1}$
Δs	Molar (intensive) change in entropy due to a reaction	$\mathrm{J\,K}^{-1}\,\mathrm{mol}^{-1}$
Ω	Collision integral used in the Chapman-Enskog relation. Indicates a collision probability to fluid parameters	

Symbol	**Description**	**Unit**
χ	Parametrised humidity (vapour fraction) of fuel mixture. A value of 0.0 represents a fluid consisting purely of water, whereas a value of 1.0 represents a fluid consisting purely of hydrogen	
$\dot{H}$	Energy transfer associated with a mass flow leaving or entering the element with a certain temperature, causing a net convective term	W
$\dot{Q}_{cond}$	Heat conduction with a neighbouring element	W
$\dot{Q}_{conv}$	Convective heat transfer between a solid element and a fluid	W
$\dot{Q}_{gen}$	Heat generation due to (exothermic) irreversibility of the chemical reaction	W
$\dot{Q}_{ohm}$	Heat generation due to ohmic losses inside of the element	W
$\dot{Q}$	Heating power	W
$\dot{m}_i$	Mass flow rate of species i	$\mathrm{kg\,s^{-1}}$
$\dot{y}_i$	Mole flow rate of species i	$\mathrm{mol\,s^{-1}}$
$\epsilon_{A,B}$	Average Lennard-Jones potential of a binary mixture of fluids A and B	V
η_{act}	Activation overpotential	V
η_{conc}	Concentration overpotential	V
η_{ohm}	Ohmic overpotential	V
ν_i	Stoichiometric coefficient of the reaction for species i	
ϕ_{el}	Volume fraction of the electrically carrying phase in a composite electrode (1 is fully metallic, 0 is fully other material)	
σ_i	Lennard-Jones length of species i in a gas mixture	$\mathrm{\AA}$
$\sigma_{A,B}$	Average Lennard-Jones length of a binary fluid mixture consisting of species A and B	$\mathrm{\AA}$
σ_{el}	Electrical conductivity of the electrically carrying phase of an electrode (i.e. Nickel in the case of YSZ)	S
σ_{ion}	Ionic conductivity of the electrolyte	S
σ_x	Electrical conductivity of an electrode x	S
τ_x	Thickness of the component x	m
ε	Porosity, how much of the porous material is void	
ζ	Tortuosity factor, the ratio between the shortest (direct) pathway and real (material) distance that the species actually takes.	
a	Activity coefficient, indicating difference from ideal behaviour for a mixture of chemical compounds.	
f	Combined variable denoting an entire fluid, containing composition, temperature, and pressure information. Most often subscripted as f_a and f_f for air and fuel respectively	
g	Combined variable denoting the geometry of the PEN or element.	

Symbol	**Description**	**Unit**
h_a	Parametrised length of the air channel for a ribbed planar geometry	mm
h_f	Parametrised length of the fuel channel for a ribbed planar geometry	mm
h_i	Intensive (on mass basis) enthalpy value of species i relative to some reference value	$\mathrm{J\,mol^{-1}}$
h_t	Parametrised total channel height for a corrugated monolithic geometry	
h	Convective heat transfer coefficient	$\mathrm{W\,m^{-2}\,K^{-1}}$
j_0	Exchange current density of an electrode	$\mathrm{A\,m^{-2}}$
j	Current density	$\mathrm{A\,m^{-2}}$
m_i	Combined variable denoting the material (properties) of material i (associated with the component).	
p_i	Partial pressure of species i in a mixture.	Pa
r_t	Parametrised mean radius of a tubular fuel cell	
r	Reaction rate, causing a change in species	$\mathrm{mol\,s^{-1}}$
s_i	Intensive (on mass basis) entropic value of species i relative to some reference value	$\mathrm{J\,K^{-1}\,mol^{-1}}$
s_l	Parametrised slant for corrugated monolithic geometry	
s_r	Parametrised rib spacing for a ribbed planar geometry	mm
s_t	Parametrised spacing between two tubes in a tubular SOFC array	
u_{in}	Inflow speed of a fluid	$\mathrm{m\,s^{-1}}$
v_m^i	Mean molecular speed of species i, which can be either the root-mean-square molecular speed or the average molecular speed	$\mathrm{m\,s^{-1}}$
w_a	Parametrised flat straight section of the air channel for a corrugated monolithic geometry	
w_f	Parametrised flat straight section of the fuel channel for a corrugated monolithic geometry	
y_i	Amount of particles of species i	mol
z	Number of electrons transferred in the (redox) reaction (2 for HOR)	

List of Constants and Fixed Values

Symbol	**Description**	**Value**	**Unit**
F	Faraday constant, the amount of charge carried by one mole of electrons	96485	$\mathrm{C\,mol^{-1}}$
R	universal gas constant	8.3145	$\mathrm{J\,K^{-1}\,mol^{-1}}$
k_b	Boltzmann constant	1.38065	$\mathrm{J\,K^{-1}}$

1
Introduction

Global warming is one of the greatest existential threats not just humankind, but life on planet earth as a whole has ever faced. Our society must change, reducing consumption where possible, or finding alternative means where required [1]. The majority of this endeavour lies in the realm of politics, but technological challenges also remain. A paramount challenge still obstructing the path towards a green energy transition is the storage of energy for later use [2]. Energy storage plays a role on a grid level to buffer periods of low energy generation, but it also enables devices to operate while disconnected from the network; a direct tie into the transition to alternative fuels for the mobility sectors. Storage relies on using a medium, on option of which is chemical, most often in the form of hydrogen. This can be pure gaseous or cryogenic hydrogen, but hydrogen-based or hydrogen-derived compound such as ammonia come up in the greater discourse. Such fuels can be converted directly and relatively efficiently into electricity with the use of a fuel cell [2]. This makes fuel cells a key technology to the transition to alternative, sustainable fuels.

1.1. Solid-Oxide Fuel Cells in Aviation

The HYdrogen eLectrical Engine Novel Architecture (HYLENA) project that this work is a part of aims to integrate a Solid Oxide Fuel Cell (SOFC) running on hydrogen within the context of existing turbofan jet engines, constituting a hybrid propulsion system: electric power generated by the fuel cell carries the base load for the turbomachinery, while a conventional (combustion) cycle (also operating on hydrogen) is responsible for transients and peak loads [3].

As a pioneering project, best practices for hybrid engines of this class are largely unknown [4]. A very large design space must first be surveyed before concrete design choices can be made with confidence. In addition to the many questions confined to hydrogen combustion and engine integration, one major variable of this design space is the SOFC stack itself, as no previous cases of such a system being integrated into an aircraft engine are known. The goal of the research presented in this work attempts to aid in covering one large portion of the design space related to the fuel cell stack, ultimately aiming to gain insights that can help with making engineering decisions to make the engine envisioned by the HYLENA project a reality.

For the application of fuel cells in aviation specifically, it is important to design the fuel cell in such a way that it minimises system mass and space utilisation, all the while retaining a high power output. Research has shown the potential of using novel cell designs; changing the stack architecture from the conventional planar configuration to (micro-)tubular and monolithic geometries is generally associated with an increase in power density [5], [6], [7], [8]. While historically limited by manufacturing capabilities, these architectures have become especially enticing with the advent of additive manufacturing and other new techniques, allow construction of shapes and dimensions previously thought impossible while reducing cost [9], [10]. Problems with sealing that plague planar SOFC assemblies [11], [12] can largely be bypassed by laying out geometries in smarter ways as well [6].

1.2. Challenges in Novel Stack Design

Research into novel fuel cell stack designs has mostly been limited to a very high level. Novel concepts are covered qualitatively by stating their potential, but the impact of the specific design is hardly ever assessed quantitatively. It is known that their overall performance can be better than that of existing designs and architectures, but but detailed analysis on the most critical influence parameters are largely left unexplored.

Factors limiting the volumetric- and gravimetric **power density** of a fuel stack are mainly due to problems in thermal management [13], [14], and losses due to stacking inefficiency [15], [16].

Assessment of the **thermal performance** of novel fuel cells is largely unexplored as well. While the novel cell presented in these studies generate more power per volume, this goes hand in hand with an increase in generated (waste) heat that needs to be managed [6].

Similarly, the **ohmic performance** of novel cell designs has not been surveyed in great detail either. It is commonly understood that the physical electrical path length between electrodes and current collectors must be minimised to reduce ohmic losses [17], as this loss term (and accompanying heat generation mechanism) makes up a large part of the performance loss in conventional fuel cells. Therefore, it must be investigated how this knowledge is transferable to novel cell designs [18].

1.3. Simulation Tooling

All three of these matters tie into generalisation and transferability of knowledge: The increased complexity and larger amount of degrees of freedom of the geometries of these novel cell designs compared to conventional stacks means that previously established design rules and conventions are not guaranteed to always be applicable to real-life assemblies [5]. New tooling is required to perform initial analyses and gain an intuition for the key design considerations within this class of SOFC stacks for a project like HYLENA to succeed. Research focusing on the impact of the geometrical shaping of these cell designs can shed light on what are indicative of performance and limiting factors in their designs. The knowledge gained from such an exploratory research of the field can be used to constrain the search space. In the process, this can steer future, more detailed research by giving an indication of where large improvements can still be made, and what factors are of lesser importance.

Essential features of good tooling to be used in explorative design studies into novel SOFC designs is simulation software with a focus on execution speed and ease of use. The existence of such software would allow for rapid exploration of a broad design space, and even for initial optimisation studies.

2

Methodology

In this chapter, the theoretical inner working of the GOOSE model as well as its implementation will be described in detail.

First the high-level operation is discussed, introducing the division into sub-models, after which each one of these sub-models will be treated in more detail. For documentation on how to use the software, please see the documentation and Appendix A.

2.1. The Purpose of a Model

Fuel cell models aid in assessing performance of fuel cell configurations without needing to physically construct said device. A simulation is much faster to set up, saves the high cost of manufacturing prototypes, and allows for much more intricate analysis than what would be possible by physically placing potentially intrusive sensors in a fuel cell. It should go without saying that this approach is not a substitute for experimental studies, but merely a good first step while no concrete decisions have been made yet.

The goal of the model built is to enable rapid iteration and exploration of a broad design space, as introduced in chapter 1. For this, the model needs to be able to finish execution in a short amount of time, be easy to use, and trivial to integrate into existing pipelines.

2.1.1. Bottom-Up

To be able to give insight into the effects of changing geometries, it should be able to represent a great variety of configurations. This puts an emphasis on broadness of applicability while being as generic as possible to allow for arbitrary material characterisations and configurations to be considered. To be able to do this, the model needs to be generalised; it cannot depend on empirical estimations for entire systems that only hold for specific configurations. It needs to model everything from the bottom up, instead of top-down. This is different from the approach taken in the bulk of existing literature on fuel cell modelling, which work the other way around by trying to gain a deeper understanding of the underlying fundamentals or the details of a specific configuration by closely tying the implementation to a physical stack whose 'correct' values have been determined experimentally [19], [20], [21], [22], [23], [24], [25], [26], [27], [28].

2.1.2. Three-dimensionality

The focus on geometric configuration underlines the inherent three-dimensionality that must be resolved: stacking, thermal gradients, concentration differences, among others. Reducing a planar SOFC to a two-dimensional or even one-dimensional representation is possible as its gradients tend to follow the primary axes only due to uniformity and symmetry of the spatial distribution. Doing the same for a monolithic fuel cell is much harder, as the varying directions of interaction do not neatly allow for simplification of the domain. The model should be able to accurately represent gradients and change in state along all axes of interaction.

One way to do this is using a fully three-dimensional simulation. This is the approach followed with Computational Fluid

Dynamics (CFD) multiphysics simulations. Albeit practical and compatible with the aims of constructing the model from the ground up, such simulations are incredibly granular, resulting in computation times in the order of hours for rough models to days for fine models [18].

Ideally, a hybrid with the general applicability of a CFD approach, yet with the simplicity and speed of execution of a reduced order model would be devised. This can be realised by making the model quasi-three-dimensional: Processes that are able to be modelled accurately with a lower-order representation are modeled using said lower order approximations, while the interactions between all systems are still inherently three-dimensional by representing elements having neighbouring elements in any direction. This approach allows for making different assumptions per *process*, and not necessarily per *domain*. Generalisation outside of this domain will be much harder to do (unlike truly generic tooling that CFD aims to be), but assumptions about the domain will make some processes much simpler or less costly to calculate with appropriate domain-specific assumptions and simplifications.

2.1.3. Steady-State

With the amount of freedom still present in the field, finding one's footing is the most important first step. For this, having the ability to assess on-design conditions is the most important, although having some indication of what the performance on off-design conditions (e.g. lower temperature, lower than ideal air flow rate) gives more certainty and gravitas as to that the designed stack will not just work in isolation, but also in application. In reality, there is however also a transient part to the equation– states of imbalance, temporal gradients between such conditions; mass accumulations, blockages, and the period of start and shutdown are inherently time-dependent. At this stage in the design process, such conditions are much less critical, and a broad analysis of the design space more important. Therefore, a model for the purposes set out for the scope of this project limits itself to the assessment of steady-state conditions only.

2.2. From Micro to Macro

Breaking down the process of modelling an SOFC stack to its fundamentals, everything that needs to be resolved is the balance between an electrochemical potential, its losses in terms of overpotentials, and the resulting current running through the system. Everything else that might affect the solution to this balance equation, such as temperature, fluid concentrations, etc. only serve to solve this underlying problem. They are implicit– merely affecting the solution as *state*. Directly solving this balance system-wide is is the philosophy that zero-dimensional reduced order models take to heart. However, state varies quite significantly with the confines of a stack [29]. For example, fluid concentrations are much higher at the inlet, meaning higher local reaction rates, and hence more heat production. Discretising the state helps represent this, allowing modelling of the interaction processes between these discretised sections. In this work, these discretised sections will be referred to as *elements*. Elements are divided not only in the flow-wise direction (of which the convention used in this paper is the depth coordinate z), but also in the plane orthogonal to it. One ”slice” of the mesh may contain many elements, much like a fully 3D mesh. Contrary to what is often seen in CFD simulations, a mesh is not built up from volumes following a simple grid-like pattern. GOOSE categorises these elements into three distinct groups, all indicating regions where different processes are relevant:

1. Positive (electrode)-Electrolyte-Negative (electrode) (PEN) elements are compound sections named after its main constituents it is assembled from: A negative electrode, an electrolyte, and a positive electrode. It represents the part of the cell that are able to actively perform a reaction. It is by far the most complicated element type.

2. Current Collector (CC) are non-reactive parts of the assembly that function purely to form a full electron path: From one PEN to another for stacking, or to the edge of the

system/ They also play a secondary role in distributing heat within the assembly.

3. A *Fluid* is a volume filled with fluid with a certain composition, temperature, and pressure.

The relevant processes to be modeled inside on such PEN element are illustrated in Figure 2.1

Processes are modelled on a per-element basis, but some depend on not just their own state: Processes like heat transfer also depend on other elements in their direct vicinity. These other elements will be referred to as an element's *neighbours*. This is used to refer to the directly adjacent elements in all three dimensions: as will be elaborated upon in the next section, implying neighbours within the same mesh slice, but also in the flow-wise depth coordinate.

All elements have their own state: The PEN type and CC type are solid (and for the former, porous), represented by a volume-average state. Calculations between them are on a finite difference basis. The state of fluid volumes are represented as a linear profile, due to their inflow and outflow potentially being very different due to species production and consumption. All interaction with the solid elements is assumed to take place at the midpoint, at the average of their inflow and outflow. Calculations for this type of section is on a finite volume basis.

2.3. Computational Domain

It is already established that the model should represent spatiality by subdivision into *elements*, which each border other elements to represent gradients in state. Now the question is exactly *how* it can best be subdivided. This depends highly on the types of geometries that we want to be able to represent: Simpler geometries allow for simpler parametrisations and reduction to lower orders. Planar fuel cells, as their name suggests, would be very simple to model as purely two-dimensional. Very complicated cross-flow, monolithic geometries would require intricate meshing options. While keeping many options open, such an approach closes doors in simplifications that can be made on a tooling level, increasing required computational and development efforts.

To balance these two contradicting constraints, GOOSE makes one fundamental restriction into the types of mesh that can be represented: all fluid flows need to be along one primary axis. This means that **cross-flow** configurations cannot be considered, but co-flow and counter-flow configurations are possible to model. This is a admissible simplification, as such configurations are generally more promising for high-performance cells [22], [30]. With this restriction on the mesh, the mesh can easily be divided up into *slices* along the main flow axis (This axis will be referred to as the z or *depth* axis from here on out). Each of these layers will have a collection of elements: PENs, CCs, and fluids (allowing an arbitrary amount of air channels, fuel channels, etc. that do not mix).

The second simplification is that it is assumed that the geometry is constant along this depth axis. All ducts are straight (no diverging ducts) and have the same cross section, opening up the ability to define only one cross section and re-using that along the entire z-depth. It also naturally follows from this restriction that every element has two additional neighbours: its geometrically identical counterparts in the slice before it, and the slice after it. Two exceptions from this are all the elements at the first and last layer. These two layers are assumed to have a Neumann boundary condition with the environment.

SOFC geometries follow some rules, and these rules can be exploited in the mesh creation process. The anode always needs to be adjacent to a fuel (hydrogen) channel, and the cathode always needs to be adjacent to an oxidiser (air) channel. The two electrode layers are always separated by a layer of electrolyte, and the fluids are (almost) always separated (either by the PEN itself, or using some sort of sealant on top of a current collector). In other words, the components along the edges between the fluid channels defines the mesh. This can be leveraged into representing the mesh as a

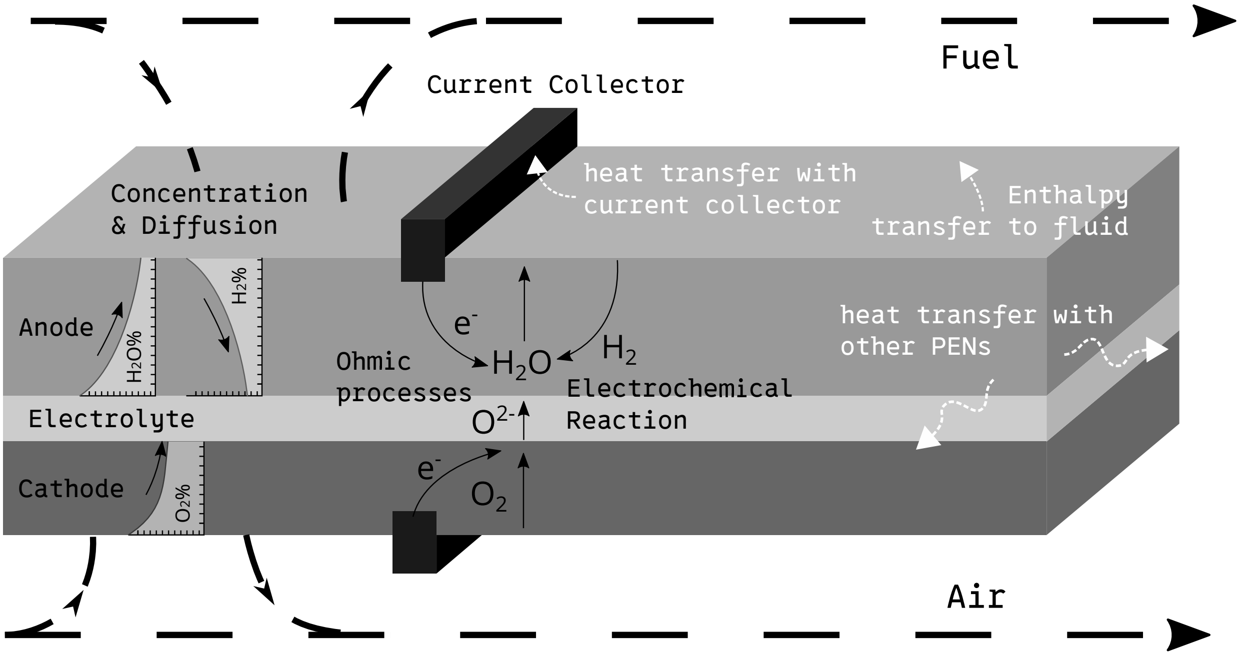

Figure 2.1: An illustrative depiction of all the relevant processes that need to be modelled locally for every PEN element.

graph: A series of vertices with edges between them, where the edges are instances of some type of element. The edges can be subdivided to get a higher spatial resolution for the elements. This is visualised in Figure 2.2.

Along an edge, elements can only have two neighbours: One further along the line, and one further back. This increases the amount of neighbours for most elements to four. The exception to this is for any elements that are the first or the last of their kind on a line, directly next to a vertex. For these elements, it can be said that their neighbours are all the other elements that neighbour this same vertex. The interface between these elements is more complicated however– they are not placed flat against each other, but placed in some n-gon around a point. To compensate for the reduction in effective surface area, the surface area with such neighbours is evenly divided. An example of one such mesh constructed with this framework is visualised in Figure 2.3.

Simulating a full mesh of a very large amount of many repeating sections is still very expensive. Instead, the inherent constant patterning of a fuel cell stack can be used to simplify both the definition of the mesh and alleviate some of this computational pressure by only simulating one repeating section, and representing patterning by using boundary conditions. Such cyclic boundaries can then be handled by defining *coincidence* of vertices: every element that neighbours one vertex, must also neighbour all the elements bordering the other. Effectively, this works as mixed Neumann-Dirichlet boundary conditions depending on the model being evaluated.

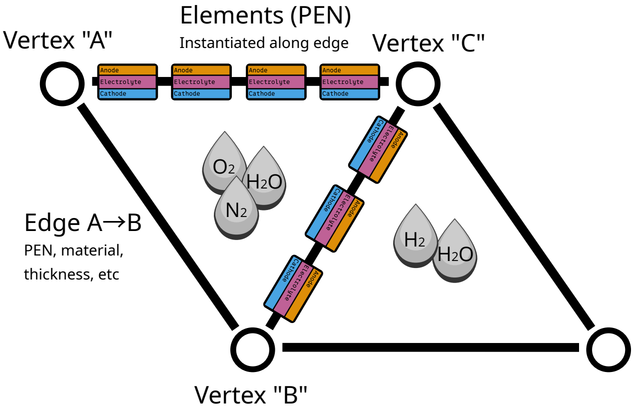

Figure 2.2: A graphical summary of how meshes are represented in GOOSE as a collection of vertices connected by edges, along which elements are instantiated.

It immediately becomes apparent that there will always be sections that overlap. The theoretical representation of the mesh as a collection of lines has one severe discrepancy with reality: components are not infinitely thin. This is a problem at the current collector to PEN interface, where the two components meet at an orthogonal interface. In reality, this joint causes part of the electrodes to be *shadowed* by the current collector in some places; a **dead zone** , an area where the local current generation is severely limited due to the absence of reactants. The direct exposure of the electrode to the fluid is interrupted, and diffusion processes now need to take a much more indirect path to move past this obstruction. A mechanism is implemented to represent this in the mesh: it will still consider such a shadowed element as a PEN, but it will not be able to freely exchange fluid with the bulk flow.

More details on how dead zones are handled is given in subsection 2.8.6.

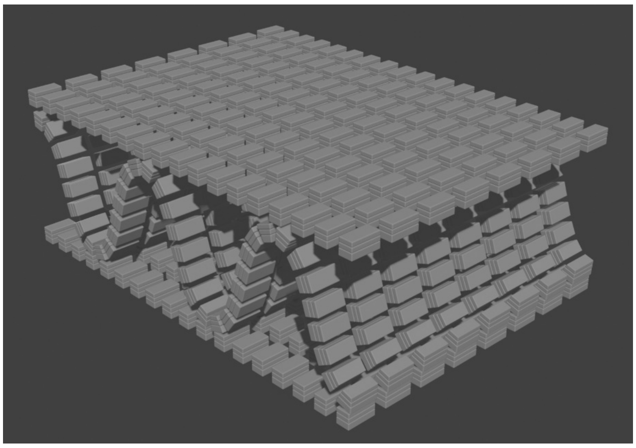

Figure 2.3: A render of a three-dimensional mesh of a corrugated monolithic SOFC, as represented in GOOSE.

2.4. Solving Scheme

The dependency on the solution of one element to that of another introduces a discrepancy in calculability in the model: There is an implicit relationship. As many of the relevant processes are strictly non-linear, the model can therefore only be solved iteratively.

Embracing the iterative nature of solving such a problem also reveals a strength of this approach: Evaluations can be done in parallel for each element. In the computational representation of the state of the model it must however be guaranteed that the value of the state of a neighbouring element must not be modified while reading from it. This is a concurrency problem often solved using *mutexes*, but this approach has a significant associated overhead, meaning a lot of computational time is lost acquiring and releasing locks. To be able to execute as many calculations as possible in parallel in the shortest amount of time, mutexes are avoided, and newly calculated values are written to a buffer that is only later used to overwrite the old values. This means that on a high level (between elements), the model works with Jacobi iteration exclusively. Figure 2.4 graphically summarises this high-level main iteration loop of the program covered up to now.

Using just the previous solution as the next best guess of state in iteration is a good start, but because of the large amount of coupling variables present, such an approach can lead to a very stiff system, which takes a long time to reach convergence. If the value is further out, it would take a long time for the result to migrate over to this new value incrementally. To make the process of resolving faster, one can choose to intentionally destabilise the system: Instead of using the value that it has right now *exactly*, its previous values can be looked at to determine a trend, which can be extrapolated to obtain a value that it might expect next. This is implemented based on second order polynomial reconstructions from the last three iterations, with a tunable aggression factor for the end-user. The application of such an algorithm makes calculations among boundaries of the system as a whole slightly more unstable, but significantly faster to reach convergence.

2.5. Subdivision into Sub-models

So far, the overall high-level structure of the program has been covered. The division of the model into three distinct element types has been established: PEN, CC and fluid. The computational domain is also explained, assigning relations between the aforementioned

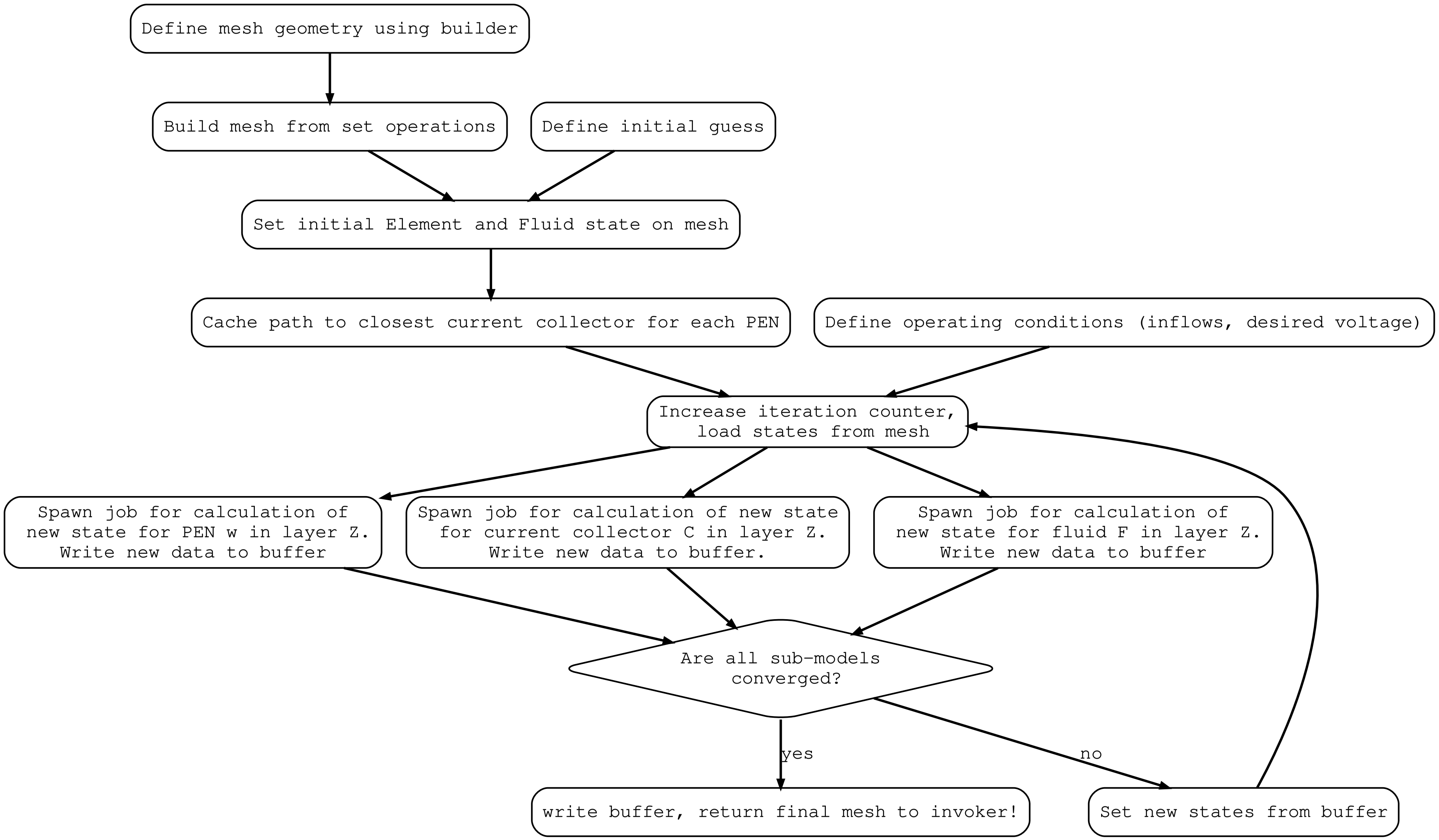

Figure 2.4: A visualisation of the high-level calculation scheme used in GOOSE. The model works using Jacobi iteration on a per-element basis, using a collector architecture.

elements. What remains now is the framework in which they interoperate, and how new state is ultimately calculated.

All three element types have some shared patterns and functionality to calculate a new state, but each also possess unique ones. For example, both the current collector and the PEN can conduct heat, but only the PEN experiences a source term of heating due to chemical reaction. Modelling all the processes as one monolithic block is a sure-fire way to make a model incredibly hard to digest for the human mind, if not impossible due to interrelations of all the processes. Therefore, to reduce calculation duplication and break up the model into understandable, individually testable and interpretable chunks, the *Determine new state* operation in Figure 2.4 is divided up into smaller chunks, or *sub-models*.

1. The PEN and CC both represent solid elements (although the PEN is porous, meaning there is an inherent interrelation with fluid). Both of these need to account for heat transfer. The **Thermal Model** is responsible for calculating a new temperature based on a heat balance. The main calculation is the same, but the contributing terms differ for the PEN and CC.
2. The **Activation Model**, as the name suggests, determines the activation overpotential, also yielding a current density.
3. Ohmic losses are in reality the result of three disparate loss mechanisms: Losses due to the oxygen ion having to penetrate through the electrolyte, losses due to the electron path spanning part of the anode to reach a current collector, and the same but now for the cathode. Determining these losses is the responsibility of the **Ohmic Model**.
4. The **Electrochemical Model** uses the overpotentials calculated in other sub-models to determine an operating voltage. It is closely linked to the *Activation Model*, and together with it returns the operating point of the fuel cell as a voltage-current density pair.
5. Bulk fluid exchange with the fluid trapped inside the porous electrodes is the domain of the **Concentration Model**. It links the PEN state to the species composition at the TBP.
6. The fluids inherently work slightly differently from the solid elements. Therefore, all of its functionality is joined together into a **Fluid Model**, which is responsible for solving energy conservation and mass conservation equations on a fluid level.

The PEN element represents a structure consisting of different materials. The ohmic model and thermal model must take this into consideration. For the CC element, this is much simpler as it is a single material only.

All of these models are run on each individual instance of their respective elements. As there is some interdependence of the models, it makes sense to link them together to form Gauss-Siedel iteration within an element where possible: For example, the results of the ohmic model directly feed into the electrochemical model (overpotentials) and the thermal model (ohmic heating). Similarly, the concentration model is only used to determine a concentration overpotential. It therefore makes sense to use the newly calculated values from these sub-models directly, instead of first writing them to the state of the PEN element, and using it in the next iteration. This calculation scheme is visualised in Figure 2.5.

Almost exactly the same process holds for a CC, but it uses its own specialisation of the thermal model, while also not having to consider any electrochemical or concentration effects. Its ohmic model also does not need to resolve a composite structure, and can simply use material properties directly. In effect, it is merely a simplified scheme of the same models already implemented for the PEN elements. A figure similar to Figure 2.5 is made for the CC in Figure 2.6 to show this difference, and its implication on solving order.

The flowcharts in Figure 2.5, Figure 2.6 and Figure 2.4 are presented to aid in visualising the

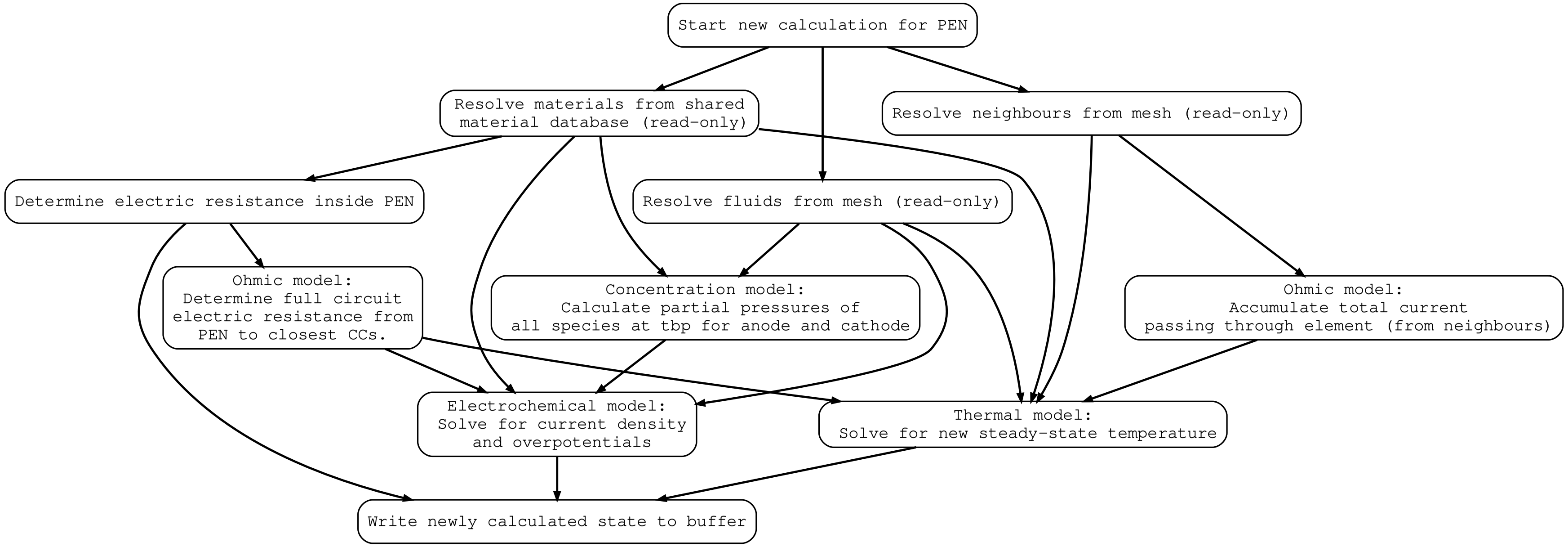

Figure 2.5: A visualisation of the calculation scheme used for calculating the next value of the iteration for the PEN element type. It displays the partial independence of the sub-models, which lends itself well to hybrid Gauss-Siedel/Jacobi iteration to enable fast calculation using parallelisation while not making the tasks too small by using shared values. Also seen is the resolving of materials, neighbours, and fluids (See subsection 2.13.5).

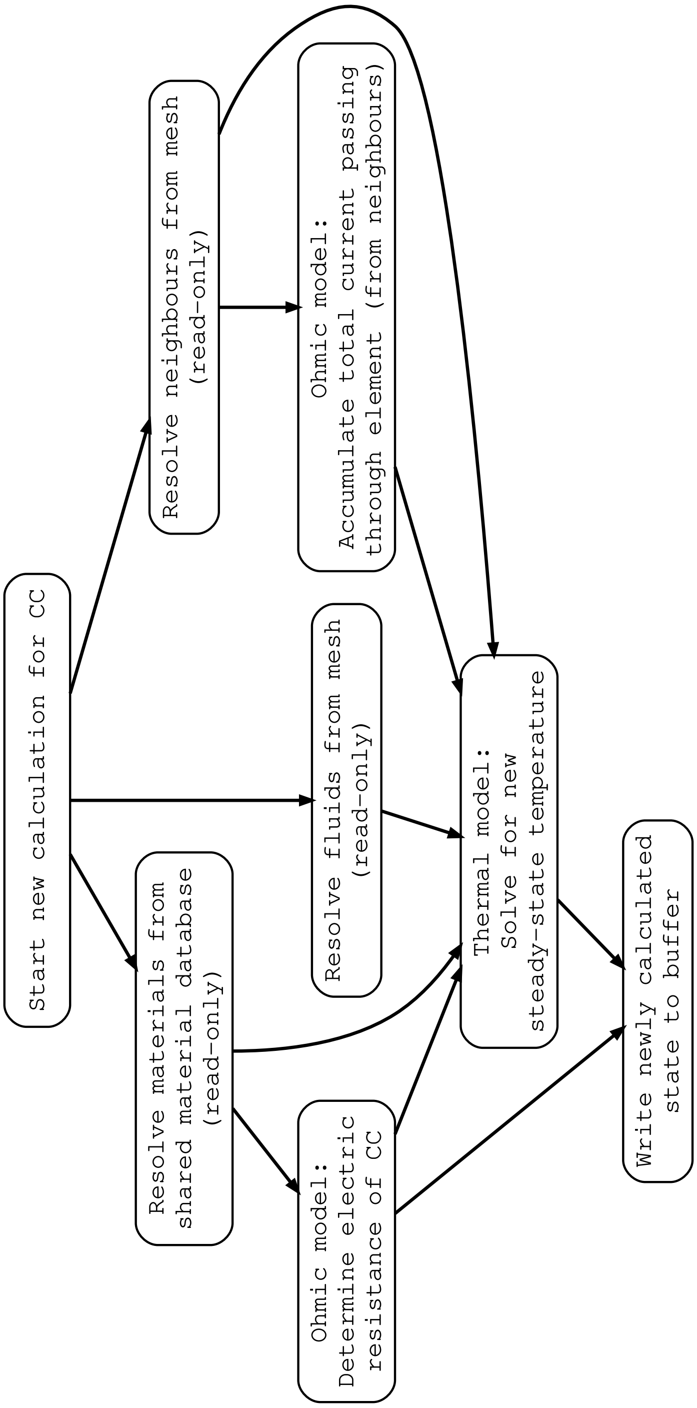

Figure 2.6: A visualisation of the calculation scheme used for calculating the next value of the iteration for the CC element type. It functions very similar to the PEN (see Figure 2.5), but has fewer sub-models.

solving order and logical organisation of the (sub-)models and solvers, but does not demonstrate anything about their interactions, or the flow of data. For that purpose, an eXtended Design Structure Matrix (XDSM) diagram is presented in Figure 2.7, with a detail of the PEN element calculations in Figure 2.8 [31]. Though not necessarily conventional, this was serves to improve overall legibility of the diagrams, as embedding them all in a single figure would make it challenging to digest.

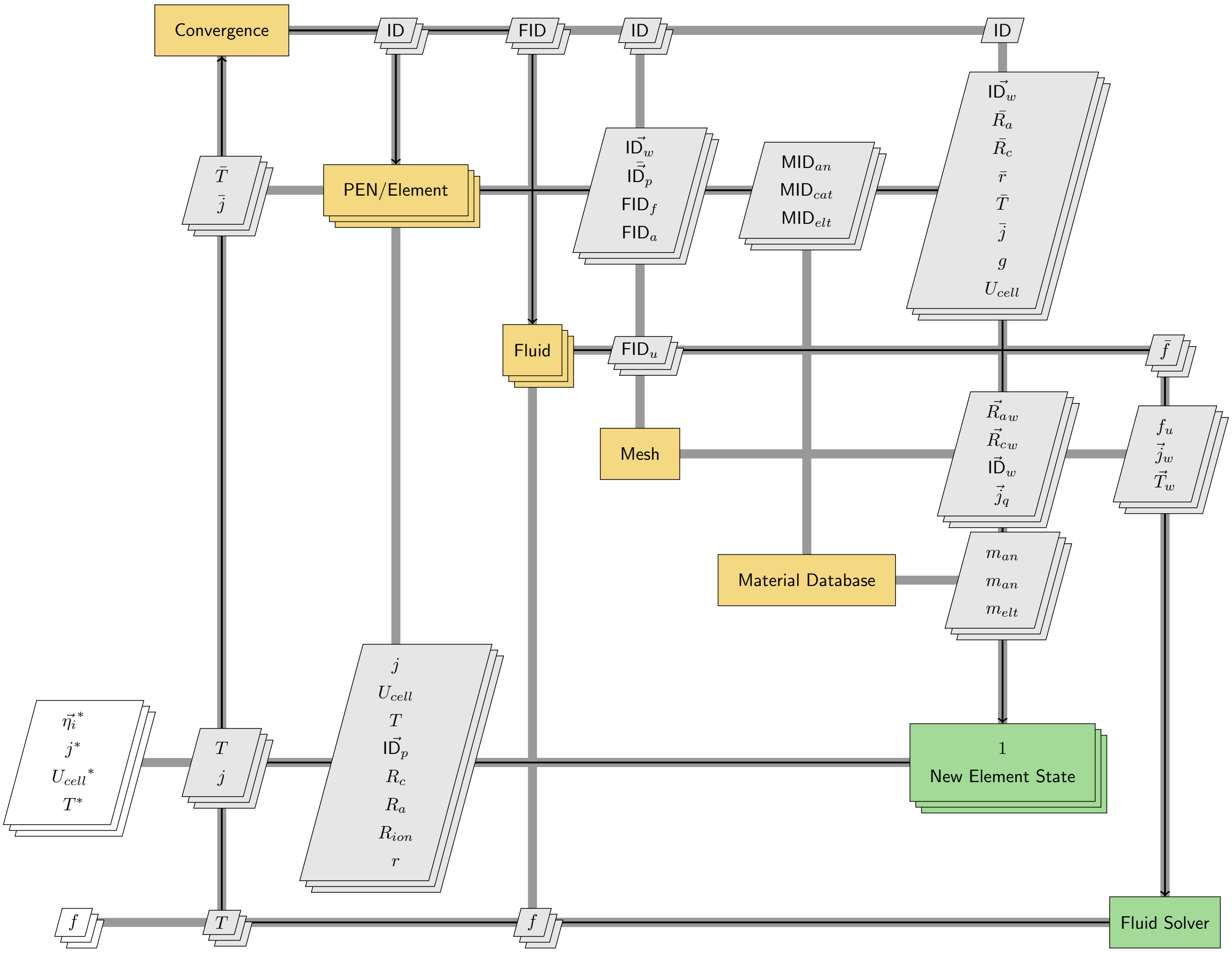

Figure 2.7: An XDSM of the high level of the program. Values with a $super^t$ are coupling variables, as in Lambe and Martins [31]. An extension is made with the introduction of $b\bar{a}r$ for are values that are stored on the mesh/element at that iteration. Vectors $\vec{v}$ are used to denote an array of (multiple) values, and calculations that are run per-element are displayed as stacked. All the symbols used are consistent with the rest of the text, but some new concepts are introduced for compactness: g is the Combined variable denoting the geometry of the PEN or element. m_i is the Combined variable denoting the material (properties) of material i (associated with the component). f is the Combined variable denoting an entire fluid, containing composition, temperature, and pressure information. Most often subscripted as f_a and f_f for air and fuel respectively.

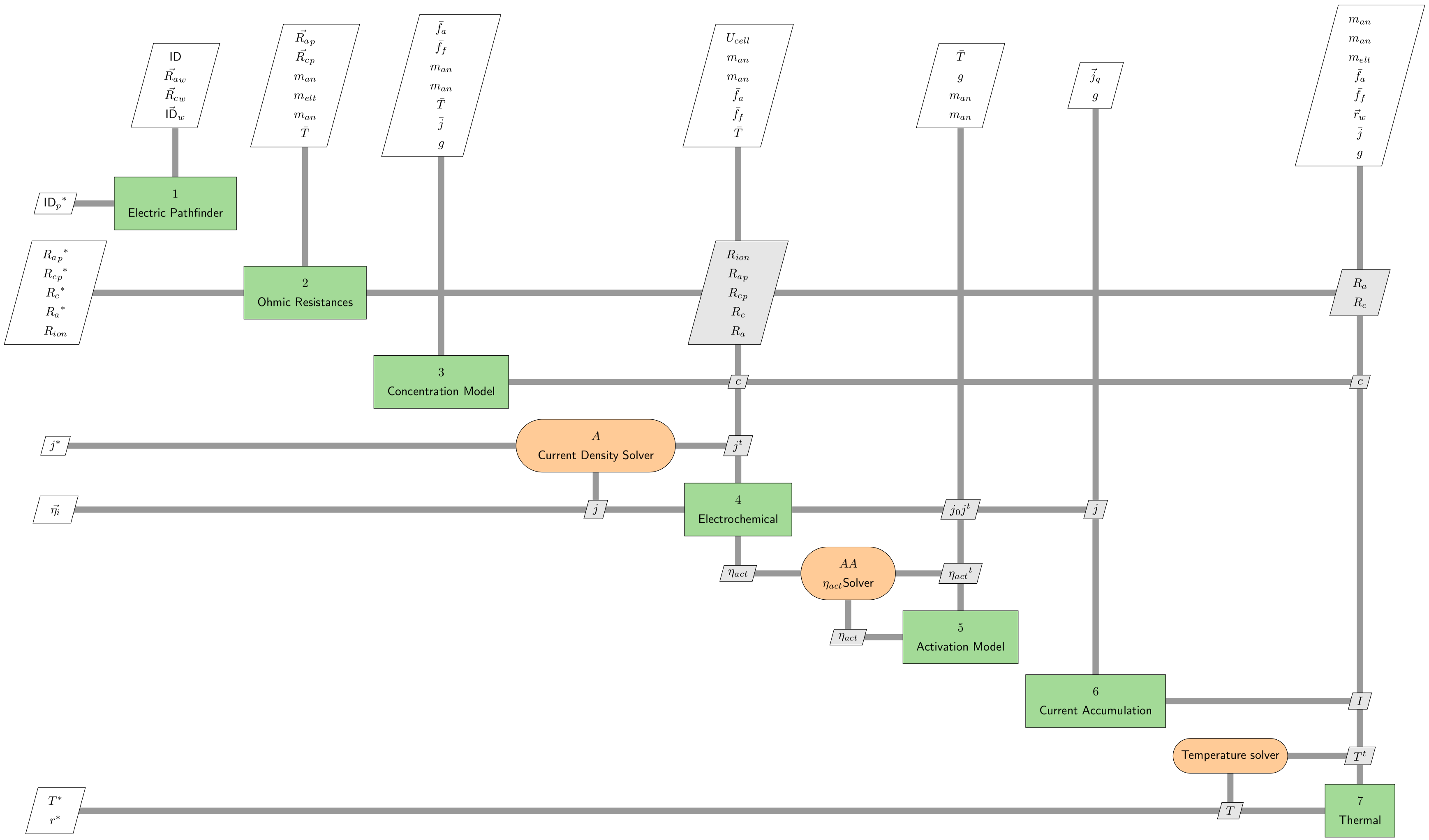

Figure 2.8: A detail of the full XDSM diagram shown in Figure 2.7, specifically for the calculation of a new PEN state. Values flowing in from the higher-level scheme are interspersed with constants as global inputs, and output variables are returned to the high-level solver.

2.6. Electrochemical Model

Functioning as a central connecting piece, linking all disparate sub-models together into one large model, is the electrochemical model. Its purpose can be boiled down to solving for a cell voltage and a corresponding current density in a potential balance, given in Equation 2.1.

Equation 2.1 describes the resulting cell voltage to be some theoretical maximum cell potential, corrected with some loss terms.

$$\begin{aligned} U_{cell}(j) = U_{Nernst} - \eta_{ohm,elt}(j) \\ - (\eta_{ohm,an}(j) + \eta_{conc,an}(j) + \eta_{act,an}(j)) \\ - (\eta_{ohm,cat}(j) + \eta_{conc,cat}(j) + \eta_{act,cat}(j)) \end{aligned} \tag{2.1}$$

j	Current density
U_{cell}	Effective voltage generated by a fuel cell, obtained after all the overpotentials have been applied
U_{Nernst}	Nernst potential of an electrochemical cell
η_{ohm}	Ohmic overpotential
η_{act}	Activation overpotential
η_{conc}	Concentration overpotential

The electrochemical system of equations has one free variable (as will become apparent in Equation 2.7). Traditionally, simplified fuel cells are represented as a current-voltage curve for this reason. To be able to determine an operating point on the current density - voltage curve as this model requires, either a target cell voltage or current density must be given. Either option is chiefly used in literature [18]. Many theoretical modelling papers restrict themselves to prescribing a fixed voltage however, on ground of this value being much more stable in magnitude, with many operations assuming a value of $0.7\,\mathrm{V}$ across different fuel cell stacks [18], [32], [33]. Were this condition to not be met, cross-currents would occur [34]. For this model, it was therefore also chosen to fix the **voltage** as an input parameter. In an experimental context, the voltage therefore also easier to unidirectionally measure. Another benefit of this approach is that the current density j is a rather non-linear function, while the voltage can always be explicitly stated. This makes the current density j a logical place to decouple the solving scheme, as will be covered in more detail in subsection 2.6.3.

2.6.1. Nernst Potential

The theoretical maximum cell potential at a specific fuel- and oxidiser combination is represented by the **Nernst potential**, which is given by Equation 2.2.

$$U_{Nernst} = E_0 - \frac{RT}{2F} \ln\left(\frac{a_{\mathrm{H_2}}\sqrt{a_{\mathrm{O_2}}}}{a_{\mathrm{H_2O}}}\right) \tag{2.2}$$

$$a_i = \frac{p_i}{p_{ref}} \tag{2.3}$$

U_{Nernst}	Nernst potential of an electrochemical cell
E_0	Standard cell potential
T	Temperature
a	Activity coefficient, indicating difference from ideal behaviour for a mixture of chemical compounds.
p_i	Partial pressure of species i in a mixture.
R	universal gas constant
F	Faraday constant, the amount of charge carried by one mole of electrons

The working principle behind a fuel cell relies on there being a potential difference between the two electrodes where half-reactions take place, allowing an electron to be captured [35]. The potential difference between the two electrodes in an electrochemical cell is expressed in Equation 2.4. This relation assumes that the reaction takes place at stoichiometric conditions. Under these conditions, the highest possible voltage can be obtained. This potential is referred to as the **standard cell potential**. Operation almost never takes place under exact stoichiometric conditions however [36]. To compensate for this non-ideal condition, an alternative expression of Equation 2.4 can be given as Equation 2.2, which is dependent on the **species activity**. This quantity is indicative of the degree of availability of reactant [34]. At a higher molar fraction, reactant that is used up is more readily replaced by a new molecule. The same holds for a higher pressure. The species activity for gaseous compounds can be related to its partial pressure relative to some reference condition p_0 with a value of $1\,\mathrm{bar}$ using Equation 2.3 [37], [38]. The voltage obtained is evidently directly dependent on the partial pressure of the reactants. Note that this is separate from the effects of species unavailability due to diffusion effects, which is covered in section 2.8.

$$U_{Nernst_{\mathrm{ideal}}} = E_0 = -\frac{\Delta G}{zF} \tag{2.4}$$

E_0	Standard cell potential
ΔG	Gibbs free energy of a reaction
z	Number of electrons transferred in the (redox) reaction (2 for HOR)

The standard cell potential only differs per reaction and temperature, as given in Equation 2.4. The term ΔG is the difference in the Gibbs free energy of the product and the reactant, which can be calculated using Equation 2.6. As the Gibbs free energy is dependent on the temperature, the standard cell potential is also a function of temperature. For standard conditions at $20\,^{\circ}\mathrm{C}$, this yields a result of $1.23\,\mathrm{V}$. While undesirable, fuel cells generally do not operate at standard conditions. Taking the operating temperature to be at $800\,^{\circ}\mathrm{C}$ (which would be a high operating temperature for a SOFC), the standard cell potential drops to $0.977\,\mathrm{V}$. In this model, the Gibbs free energy change is therefore modelled directly so that it can be used at different temperatures.

$$2\,\mathrm{H_2} + \mathrm{O_2} \leftrightharpoons 2\,\mathrm{H_2O} \tag{2.5}$$

$$\Delta G = \sum_p \nu_p h_p(T) - s_p(T) - \sum_r \nu_r h_r(T) - s_r(T) \tag{2.6}$$

ν_i	Stoichiometric coefficient of the reaction for species i
h_i	Intensive (on mass basis) enthalpy value of species i relative to some reference value
s_i	Intensive (on mass basis) entropic value of species i relative to some reference value

Here ν is the stoichiometry of the species in the reaction: in order of appearance, 2, 1, and 2 respectively. Subscripts p are the products, and r the reactants respectively.

Based on the unique states of each individual element, specific enthalpies and specific entropies are calculated based on polynomial fits Burcat and Ruscic [39][1] for the overall reaction given in Equation 2.5.

2.6.2. Linked Overpotentials

Up to this point, none of the other loss terms (η) have been described yet. This is because they are not part of the electrochemical model *directly*. The electrochemical model interacts with virtually all other sub-models to offload and modularise the calculation of intermediate values that are required to determine the overpotentials. As is shown in Figure 2.8, it takes the outputs of the *ohmic model*, and *concentration model*: A build-up of electrical resistances, and the partial pressures at both TBPs respectively. These directly lead to overpotentials $\eta_{ohm,an}$, $\eta_{ohm,cat}$, $\eta_{conc,an}$ and $\eta_{conc,cat}$. As for why these intermediate values returned, and not the overpotentials directly: recall from Equation 2.1 that all of these behaviours are functions of the local current density. By returning the intermediate value, the results of the other models can be reused to solve implicitly for the current density as much as possible, without requiring all the models to be completely re-run for each evaluation of the electrochemical model. This works for the ohmic model: As described in section 2.9 the ohmic overpotential is simple and linearly related to the sum of all resistances and the current density. As will be covered in section 2.8, for the concentration model, this works less well. Equations Equation 2.15 and Equation 2.17 could be decoupled, but Equation 2.16 cannot easily be inverted. The same holds for the activation overpotential. The linking of other overpotentials is therefore tied tightly into the solving scheme for the entire electrochemical model.

---

[1] Data of which can be retrieved from `https://respecth.elte.hu/burcat.php`

2.6.3. Solving for Current Density

Equation 2.1 implies that two conditions must be met for a solution to be valid:

1. The source voltage and overpotentials must balance out to be the required voltage.
2. The current densities these voltages are evaluated must all be the same.

To find a solution that satisfies both of these conditions, the problem must be decoupled. Hence, in this model the electrochemical model needs to iteratively solve Equation 2.1 by varying the current density j. With the voltage being set explicitly, the current density is essentially left as a coupling variable. Some current density j must be chosen, after which it must be checked if it meets the first condition. The most logical place to put this decoupling is at the most non-linear step, as it saves having to solve that specific step. This is the *Activation Overpotential Model* (see section 3.5). This specific overpotential can be partially decoupled from the equation and used to solve for the value of the current density that results in the activation overpotential and ohmic overpotential that solves the system, together with a new best-guess for the current density. Because of the decision to leave the voltage as a design variable (and not the current density), the activation overpotential model can also be directly nested into the electrochemical model instead of being coupled two-way, significantly reducing numerical stiffness.

The problem is reduced to one of error minimisation over a single variable, which can be solved with a root-finding method. All of the root-finding in GOOSE is done using Brent's method [40], and this model is no exception. The bounds are set to be 0 as a minimum (negative current densities are unphysical for fuel cell systems) and a user parameter for the maximum.

Some values used in this process do not rely on the current density. This includes the values used to calculate the overpotentials covered earlier in subsection 2.6.2. These values can be calculated once, outside of the root-finding loop. Their results are reused in the calculation to reduce unnecessary re-calculation of the same values. This is done for the Nernst potential, the electrical and ionic resistances.

Inside of the root-finding procedure are only the terms that change depending on the current density: The activation overpotential, and the ohmic loss based on the constant resistance.

The high-level process this follows is expressed in the form of a diagram in Figure 2.9.

2.6.4. Outputs available for analysis

To enable detailed analysis using GOOSE, aside from the primary outputs (cell potential and current density), all the other overpotentials are also returned. They are not part of the model solving state, which is transferred between iterations, but rather they are intermediate values. Instead of being simply discarded when they have been used to determine a new state, they can optionally be captured and output as part of the final solution so that overpotential build-ups can be reconstructed. All terms returned this way are:

- Nernst potential
- electrolyte ionic ohmic overpotential
- overpotentials caused by the anode
- overpotentials caused by the cathode

And the last item, the overpotential associated with individual electrodes, for both the anode and the cathode:

- concentration overpotential
- ohmic overpotential due to the part of the electron path that is inside of this element
- ohmic overpotential due to the part of the electron path that is outside of this element (crosses through other elements)
- overpotential associated with loss due to contact resistance caused by an imperfect interface between the electrode and the current collector
- activation overpotential
- exchange current density (as an indicator of local operating point, a checking variable)

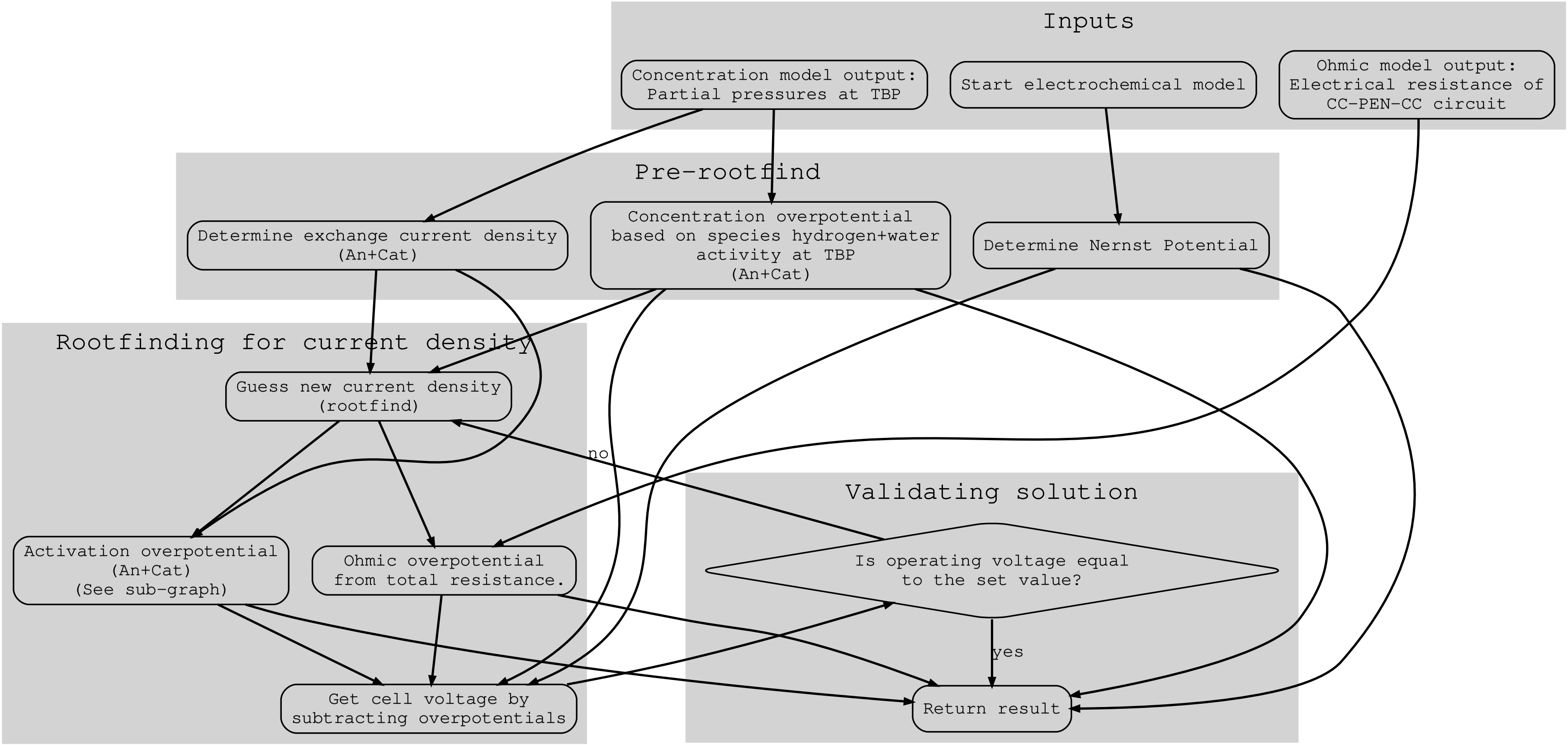

Figure 2.9: A visualisation of the calculation scheme used for solving the electrochemical model. This operation yields a cell potential and a current density.

2.7. Activation Overpotential Model

As covered in detail in subsection 2.6.3, the activation overpotential model is tightly coupled into the solving scheme for the electrochemical model. Unlike this complex integration, the physical process it represents is relatively straightforward.

As the name implies, the activation overpotential returned is simply an overpotential. One of the reasons why the real cell voltage is lower than the Nernst potential is that the activation barrier for the electrochemical reaction: The electrochemical reaction happens spontaneously, but only after a certain energy threshold has been overcome. In addition, a price must be paid: Something to offset the energy lost due to the transfer of charges between the electronic and ionic conductors. This reduces the effective energy freed in overall reaction, which can be expressed in the form of a reduction in potential as the energy is supplied by the electromotive force [13]. As this process happens at both electrodes simultaneously, this overpotential term must be accounted for on both the electrodes separately. The activation overpotential depends not only on the material properties of the electrodes where the reaction takes place, but also on its microstructure, temperature, and the partial pressures of the reactants [41].

What the electromotive force physically prescribes is a reaction speed (reaction rate). Since the reaction rate also determines the amount of electrons being circulated, it can therefore be said that for higher currents there will be a higher activation loss term [41]. The central relation between the current density and the corresponding voltage (drop) per electrode (half-reaction) is described in the Butler-Volmer equation, given in Equation 2.7.

$$j = j_0 \left(\exp \frac{\alpha_f z F \eta_{act}}{RT} - \exp \frac{(1-\alpha_b) z F \eta_{act}}{RT} \right) \tag{2.7}$$

j	Current density
h_i	Intensive (on mass basis) enthalpy value of species i relative to some reference value
j_0	Exchange current density of an electrode
z	Number of electrons transferred in the (redox) reaction (2 for HOR)

2.7.1. Determining the Charge Transfer Coefficient

In this representation of the Butler-Volmer equation, α is the charge transfer coefficient. This number gives an indication as to which direction in the half-reaction is favoured: α_f for the forward reaction, and α_b for the backwards reaction [42]. A higher value means that the activation energy required at the cathode is higher than that at the anode, and vice versa [43], [44]. It differs per material, but it can also differ per operating condition [44]. If both directions are similarly favoured, this value is $\alpha_f = \alpha_b = 0.5$.

Different characteristic values and their characteristic tafel curves are depicted in Figure 2.10.

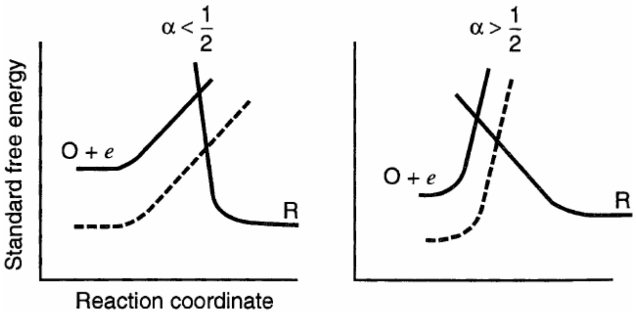

Figure 2.10: Quantitative depiction the transfer coefficient as an indicator of the symmetry of the barrier to reaction, showing the dependence of free energy on reaction coordinate. Image adapted from Bard and Faulkner [43].

A commonly made assumption in fuel cell modelling is that the charge transfer coefficient is always equal to 0.5. This is however not always the case, and as such a generic model must leave the ability open to supply them individually [42].

This is not the only assumption that is often used, but not able to represent the operational domain of an SOFC. In literature, an often-made simplification is that of collapsing the individual half-reaction Butler-Volmer equations into a surrogate equation that has embedded in it the characteristics of both. Such a Butler-Volmer represents a full reaction, instead of a half-reaction. This, combined with the unfortunately alternative name for the *forward* and *backward* subscripts as *anodic charge coefficient* and *cathodic charge coefficient* (where the *anodic* and *cathodic* does not refer to the electrode it takes place on, but to the reaction itself– an anodic reaction being equal to a forward reaction), might cause a misunderstanding that there are only two charge coefficients for the two electrodes, instead a sum total of four [45]. In this model, all four are individually representable, but simplified input with the above assumptions is still possible.

2.7.2. Solving for Activation Overpotential

The purpose of the activation overpotential model is to return an activation overpotential. The keen eye might have already spotted that the Butler-Volmer equation (Equation 2.7) is implicit, and cannot be explicitly rewritten as a function of current density. This means that the equation must be solved iteratively, or alternatively, an explicit approximative function must be used. GOOSE uses an algorithm that switches between the two methods depending on the operating regime.

2.7.3. Tafel Approximation

One approximation that can be used if the current density is *high* is the **Tafel approximation** (alternatively also referred to as the high-field approximation in literature). What constitutes *high*, literature suggests that this equation is adequately accurate for $\frac{j}{j_0} > 4$ [46], [47]. As the activation overpotential of the electrode approaches infinity, the forwards reaction becomes dominant, as apparent in Figure 2.11. Simplifying the equation by assuming the non-dominant term is zero, one can explicitly solve the Butler-Volmer equation. This mimics the Tafel behaviour, lending to its name. This can now be inverted, and explicitly rewritten for an overpotential, as seen in Equation 2.8.

$$\eta_{act,el} \approx \frac{RT}{\alpha_f F} \ln\left(\frac{j}{j_0}\right) \tag{2.8}$$

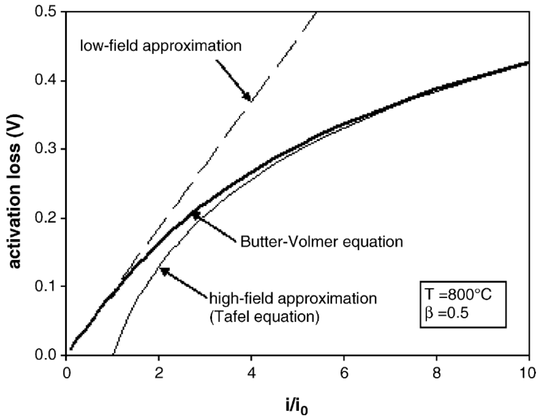

Figure 2.11: Comparison of the activation overpotential from three different calculation methods. This specific curve shows the values for a symmetrical charge transfer coefficient at a temperature of $800\,^{\circ}\mathrm{C}$. It can be seen that the error for the low-field approximation becomes smaller as the current density approaches 0, and that the error for the high-field approximation becomes smaller as the current density approaches ∞. Figure originally from Noren and Hoffman [46].

2.7.4. Low-Field Approximation

As the activation overpotential of the electrode approaches zero, the backwards term of the Butler-Volmer reaction equation becomes dominant. Using a similar approach as used in the tafel approximation, this can be solved explicitly as the **low-field approximation**, given in Equation 2.9. This equation is said to hold if $\frac{j}{j_0} < 1$ [46].

$$\eta_{act,el} \approx \frac{RT}{F}\left(\frac{j}{j_0}\right) \tag{2.9}$$

2.7.5. Implicit Solving

There exists a region between where neither of these two approximations provide good results, as seen in Figure 2.11. Here, the Butler-Volmer equation must be solved implicitly using iteration. This operation is computationally significantly costlier, and hence will only be used as a fallback if it has been determined that using either of the approximative methods yields an unacceptably erroneous result. This is an important computation performance consideration, as the activation overpotential model is the model that is run the most often, given that it is placed inside of the electrochemical model, which itself is solved iteratively.

If it must be solved implicitly, the generalised root-finding algorithm also used for the electrochemical model can be reused here, but with several small tweaks: The upper bound is set to $1.5\,\mathrm{V}$. The activation overpotential can only ever be as high as the theoretically maximum voltage generated. This voltage would then also be reduced further by still requiring some voltage as headroom, given by the desired cell operating potential. However, the dynamic iterative stepping could mean that these could be locally violated, and hence a small buffer is provided in the upward direction. The lower bound is still $0\,\mathrm{V}$, as there cannot be a negative overpotential. The convergence criterion should scale with the current density itself; It should converge based on relative error, i.e. for smaller current densities allow only a smaller error. This is done by setting the convergence criterion as $\frac{j}{j_0} \times 10^{-5}$ (which can be overridden as part of the solver settings).

2.7.6. Switching Between Solving Methods

In their respective sections, references to literature have already been made for alleged validity regions of the low-field and Tafel approximations. Despite being used quite broadly in existing research, these bounds do not seem to take into consideration the effect that changing the charge transfer coefficient has.

Indeed, the error is at its lowest for $\alpha_f = \alpha_b = 0.5$, but it increases for asymmetry. As the charge transfer coefficient $\alpha_f = 0.7$ and $\alpha_b = 0.3$ is used, the error of the low-field approximation increases to 4% at the point $\frac{j}{j_0}$. Increasing it even more indicates that the rate of increase is directly related to the asymmetry, as $\alpha_f = 0.8$ and $\alpha_b = 0.2$ causes an error of 6%.

The effect of imbalance in the charge transfer coefficients on the error is even larger: given a $\alpha_f = 0.2$ and $\alpha_b = 1.0$, the error with the exact solution increases to 10%.

To combat this discrepancy in the applied use case and region of validity in this more general context, a penalty system is introduced to create an algorithm that discourages picking approximative methods if the charge transfer coefficients are not symmetrical. If the normalised current density does not meet the threshold ($\frac{j}{j_0} > x_{tafel}$ for the tafel approximation and $\frac{j}{j_0} < x_{low-field}$ for the low-field approximation), then the fallback method of using root-finding will be used instead. The numerical parameters in the penalty as given in Equation 2.10 and Equation 2.11 were determined based on minimising error to at most 1% for a temperature of $800\,^{\circ}\mathrm{C}$, and various combinations of asymmetric and imbalanced charge transfer coefficients up to a deviation of 0.4. They have no physical basis, but have admissible results. At a temperature of $1000\,^{\circ}\mathrm{C}$, the error increases to 1.5%, which is still considered acceptable.

$$c_{as} = 8 \cdot |\alpha_f - \alpha_b| \tag{2.10}$$

$$c_{imb} = 18 \cdot |1 - |\alpha_f + \alpha_b||^3 \tag{2.11}$$

$$x_{tafel} = 10 \cdot (1 + c_{as} + c_{imb}) \tag{2.12}$$

$$x_{low-field} = 0.15/(1 + c_{as} + c_{imb}) \tag{2.13}$$

2.8. Species availability at the TBP

The operation of a fuel cell usually happens with a known species composition in the bulk flow. Here, perfect mixing and hence uniform species availability is a valid assumption. The reaction does not take place here, however: This model, like many others, assumes that the reaction only takes place on a very small region where electrode, electrolyte, and cavity (where fluid can penetrate into) come together: the Triple Boundary Point (TBP). Establishing what is the fluid state and species availability is the responsibility of the **Concentration Model**.

Ionic conductivity of the electrodes is significantly lower compared to its electrical conductivity. Reactions that occur further away would incur a very high ohmic loss to be able to move an ion through the electrode lattice, directly proportional to the distance away from the electrode-electrolyte interface. In practice, the activity further away from the TBP is so low that it is safe to assume that effectively no reaction takes place here, and all reactions take place at the TBP instead, as the activity dies off after several hundred nanometres [48], [49], [50].

On top of the non-stoichiometry at which the electrochemical reaction takes place, which is what Equation 2.2 represents, there is an additional loss due to the fact that the species availability in the bulk fluid flow is not the same as the species availability at the location where the reaction actually takes place. This holds for any type of fuel cell, but is especially relevant in the case of a SOFC, where the electrodes function as a porous medium where instantaneous perfect mixing and equal distribution cannot be assumed. The porous nature of the electrodes causes an imbalance as fluid flows are limited by physical obstruction and other diffusive processes. While the chemical reaction proceeds, reactants are used up and products are created. With non-instantaneous replenishment, this means that the local reactant availability is lower, and the local product presence is heightened. Both of these changes in concentration inhibit further reaction, as with less reactants available, there is nothing to react. There exists an inherent inertia to the equalisation of the species concentration. This can cause local concentrations and gradients in both the spatial and temporal domains if some process changes the composition of the mixture [51]. As a result, local concentrations and depletions occur. In the case of the anode, there is less hydrogen available for the reaction at the TBP, and for the cathode there is less oxygen available at the TBP. This deviation from ideal species availability can be expressed as an additional overpotential.

In addition to species *consumption*, the anode also suffers from *production*: a local increase in water content. A higher product presence means a move even further away from the reaction equilibrium, physically obstructing locations where the reaction can take place and lowering the reaction probability.

The concentration model accommodates the process of diffusion into the porous medium to balance out these consumption and production terms. It models the effect of the difference in local concentrations with respect to the bulk flow and expresses it in a way that can be related to an overpotential. This is done by determining the partial pressures at the TBPs.

2.8.1. Partial Pressures at the triple boundary point

In literature, diffusion in porous media of binary mixtures is often modeled using Fick's diffusion model, as given in Equation 2.14, while also considering an extra Knudsen diffusion term to compensate for surface effects [20], [52], [53], [54], [55], [56]. Other literature advocates for modelling the diffusion process using a *dusty gas model*, which models the solid part of the porous medium as immovable 'dust' particles [51]. The former is used in this model, as it is easier to implement, and deemed sufficiently accurate for the purposes of this model.

$$\dot{m}_i = -\frac{D^i_{eff}}{RT}\frac{\partial(y_i P)}{\partial x} \tag{2.14}$$

$\dot{m}_i$	Mass flow rate of species i
y_i	Amount of particles of species i

Modelling diffusion as Fick's diffusion allows for the derivation of an explicit formula for the partial pressures at any depth into the porous medium as a function of the local consumption rate, which is directly related to the current density. Following conservation of mass in steady state, water creation should happen at exactly the same rate as the dispersion of water moving out of the porous medium, and vice versa for hydrogen- and oxygen consumption. Then, with a Dirichlet boundary condition at the electrode surface (at the bulk fluid), the following relations can be derived for the partial pressures of water, oxygen, and hydrogen in equations 2.15 2.16, and 2.17

$$p_{\mathrm{H_2},TBP} = p_{\mathrm{H_2},bulk} - j\frac{RT\ \tau_{an}}{2F\ D^{i}_{eff,an}} \tag{2.15}$$

$$p_{\mathrm{O_2},TBP} = P_{bulk} - (P_{bulk} - p_{\mathrm{O_2},bulk})e^{j\ \frac{RT\ \tau_{cat}}{4F\ D^{i}_{eff,cat}}} \tag{2.16}$$

$$p_{\mathrm{H_2O},TBP} = p_{\mathrm{H_2O},bulk} - j\frac{RT\ \tau_{an}}{2F\ D^{i}_{eff,an}} \tag{2.17}$$

p_i	Partial pressure of species i in a mixture.
τ_x	Thickness of the component x
P	Static pressure of a fluid (mixture)

2.8.2. Effective Diffusion Coefficients

One ubiquitous term in equations 2.15 2.16, and 2.17 is the *effective diffusion coefficient* D_{eff}. The effective diffusion coefficient is obtained by combining the natural diffusion coefficient of the gas together with some correction for it happening inside of a porous medium. The **Chapman-Enskog** model is used to determine a binary mixture diffusion coefficient, after which it is combined with a Knudsen term in the Bosanquet equation (Equation 2.18) to obtain this value [20]. The Bosanquet equation is adequately applicable for the domain and operating ranges considered for most SOFC operations [57]. In this equation, ζ is the tortuosity of the material, which is the degree of indirectness of that path that a particle takes, with $\zeta = 1$ being a straight path, and higher values being longer paths. ε is the porosity of the material, which is the fraction of the material volume that is empty, and therefore permeable by the fluid.

$$D_{eff} = \frac{\varepsilon}{\zeta}\left(\frac{1}{D_{A,B}} + \frac{1}{D_{A,B_{kn}}}\right) \tag{2.18}$$

ε	Porosity, how much of the porous material is void
ζ	Tortuosity factor, the ratio between the shortest (direct) pathway and real (material) distance that the species actually takes.

2.8.3. Binary Mixture Diffusion Coefficients

The **Chapman-Enskog** method of determining the binary mixture diffusion coefficient is widely used in fuel cell modelling [56], [58], [59]. It relies on relating the materials' Lennard-Jones characteristics to a collision integral, representing the likelihoods of particles exchanging energy and momentum [60], [61]. σ_{AB} is the average Lennard-Jones length for materials A and B, simply given by Equation 2.20.

$$D_{A,B} = 0.001858\frac{T^{3}2}{P\sigma^2_{A,B}\Omega}\sqrt{\frac{1}{M_A} + \frac{1}{M_B}} \tag{2.19}$$

$$\sigma_{A,B} = \frac{\sigma_A + \sigma_B}{2} \tag{2.20}$$

$D_{A,B}$	Bulk (binary) diffusion coefficient for a two-component mixture consisting of fluids A and B
P	Static pressure of a fluid (mixture)
Ω	Collision integral used in the Chapman-Enskog relation. Indicates a collision probability to fluid parameters
M_i	Molecular weight of species i
$\sigma_{A,B}$	Average Lennard-Jones length of a binary fluid mixture consisting of species A and B
σ_i	Lennard-Jones length of species i in a gas mixture

This equation does not use standard SI units; being an empirical relation, it requires values to be input using the following units:

1. P is the static pressure in atmosphere (In the literature there is no consensus on the units to be used. Some sources prefer bar, but the oldest sources the author could find were in atmosphere).
2. σ_{AB} is the average Lennard-Jones length in Angstrom (1 Å = $1 \times 10^{-10}\,\mathrm{m}$). The average Lennard-Jones length can be calculated from the **fluid property** Lennard-Jones length as $\sigma_{AB} = (\sigma_A + \sigma_B)/2$.
3. M_A and M_B are the molecular weights of species A and B (order does not matter) in $\mathrm{g\,mol^{-1}}$ (i.e. Oxygen $\approx 32\,\mathrm{g\,mol^{-1}}$).

2.8.4. Collision Integral

The term Ω is the collision integral, which relates the collision probability to some more material properties and the temperature, indexed as $\Omega = f(\frac{kT}{\varepsilon_{A,B}})$. The actual shape of this function is almost universally based on experimental findings- specifically, a series of studies carried out by J. O. Hirschfelder and Bird [62], who tabulated a large range of values. A polynomial fit as given in Equation 2.21 by Poling et al. [61] was verified to have an error of less than 0.5% in the relevant regions.

$$\Omega = \frac{A}{x^B} + \frac{C}{\exp(Dx)} + \frac{E}{\exp(Fx)} + \frac{G}{\exp(Hx)} \tag{2.21}$$

$$x = \frac{k_b T}{\epsilon_{AB}} = \frac{T}{\sqrt{\epsilon_B / k \cdot \epsilon_B / k}} \tag{2.22}$$

k_b	Boltzmann constant
$\epsilon_{A,B}$	Average Lennard-Jones potential of a binary mixture of fluids A and B

In Equation 2.21, the substitution of the argument with x as done in Equation 2.22 is made for the sake of brevity. The following constants are used:

- $A = 1.06036$
- $B = 0.15610$
- $C = 0.19300$
- $D = 0.47635$
- $E = 1.03587$
- $F = 1.52996$
- $G = 1.76474$
- $H = 3.89411$

As for how to index this function: All the material differences are represented by the (non-dimensionalised) argument of the function. The set of the collision integral is the same for any material. ϵ_i is the Lennard-Jones potential, which is a fluid property, most often experimentally determined from viscosities, for which large tabulated datasets exist [60], [61] scaled relative to the Boltzmann constant k_b. These fluid properties must be combined to get a combined Lennard-Jones energy, which can be done as given in Equation 2.22

2.8.5. Knudsen Diffusion

Knudsen diffusion is modelled using a method similar to Yakabe et al. [58] and Asaeda et al. [63]. The Knudsen diffusion coefficient is given in Equation 2.23, which is an empirical relation depending on a molecular speed v_m and the mean pore radius r. As the molecular speed is not the same for individual every particle, a value representing all speeds must be used. The molecular speed follows a Maxwell-Boltzmann distribution, so different options are available [64]. How this is resolved is left as a solver parameter, giving the option to choose between the mean square molecular speed, given in Equation 2.24 [65], and the average molecular speed, given in Equation 2.25 [64]. Here, M is the molar mass of the specie in question.

$$D^i_{kn} = \frac{1}{3} D_{pore} v^i_m \tag{2.23}$$

$$v^i_{mrms} = \sqrt{\frac{3RT}{M_i}} \tag{2.24}$$

$$v^i_{mavg} = \sqrt{\frac{8RT}{\pi M_i}} \tag{2.25}$$

D^i_{kn}	Knudsen diffusivity due to interactions with a porous medium for species i in a mixture
D_p	Average pore diameter of a porous medium
v^i_m	Mean molecular speed of species i, which can be either the root-mean-square molecular speed or the average molecular speed
M_i	Molecular weight of species i

2.8.6. Non-Orthogonal Diffusion for Regions Not Exposed to Fluid

The astute reader might have noticed that the assumption that diffusion occurs exclusively orthogonal to the bulk fluid flow cannot hold for every part of the PEN. **Dead zones**, areas of the PEN that might still be active, but are not directly exposed to the bulk fluids, exist at the interface of the current collector and the PEN. In reality, there is a small amount of fluid that penetrates not just into the electrode, but also sideways. This sideways diffusion however comes at the price of a drastically increased diffusion path, leading to a significant increase in concentration overpotential. As a result, the activity of this area is significantly reduced [48], [66].

It can be shown using Equation 2.15 and Equation 2.16 and the data used in the validation case based on Su et al. [32] that the effect of increasing the diffusion path length on the concentration overpotential is severe. At distances larger than $d > 4\tau$, the partial pressure drops to less than 20%. This compounds threefold, as this effect compounds for all the active species on both the anode and the cathode side. Even in the case of asymmetric current collector placement the effect is significant. Concentration overpotential now locally forms the majority of the voltage, reducing the generated current density to less than 8% of the value in PENs directly exposed to fluids.

As such, the activity in dead zones is assumed to be negligible in this model. In reality, there will still be *some* reaction at these locations, with the made assumption being a simplification. In GOOSE, these dead zones are represented by a different element type. They have many of the same properties as a PEN element, but lack the electrochemical activity. As the diffusion into these elements is not actually modelled. Fluid-derived properties such as the thermal conductivity are assumed to still work with the values of its TBP as if it were connected to a bulk flow directly. In essence, they are just passive, notcontributing to the overall reaction, while still functioning like a PEN for current density carrying and thermal conduction.

2.9. Ohmic overpotentials

The ohmic model yields an ohmic overpotential, which itself is actually comprised of three different overpotentials: A loss due to the oxygen ion having to conduct through the electrolyte, and a loss for each of the electrodes due to closing of an electron path between the TBP and the current collector. First the ionic loss will be covered. The ohmic loss for electrodes will be covered for a generic electrode, because the method is identical for both electrodes. It must be stressed that they are independent however: the shortest path and resistances are stored per electrode, not per PEN.

Using Ohm's law (Equation 2.26), both losses can relate a resistance to an overpotential The overall goal for each term is hence to obtain a representative resistance.

$$R = \frac{U}{I} \tag{2.26}$$

The practical approach to determining the electrical resistance of an electrode is very similar to that of the ionic resistance, with two caveats: The primary one is that the path length is much more complicated, as it needs to span form the current collector to the TBP. A secondary difference arises in how the electrical conductivity is determined for the material, as the porous structure of the component needs to be taken into account. subsection 2.9.2 covers the determination of this path, while subsection 2.9.3 focuses on how exactly the conductivity for an element is determined.

2.9.1. Ionic Loss

As detailed in section 2.8, all reactions are assumed to take place at the TBP, an infinitely thin plane where the electrode interfaces the electrolyte. Ionic transfer through the electrode need not be considered, yet there is still the ionic transfer through the electrolyte. To model the ionic loss, it is assumed that the ion moves in a straight line through the electrolyte, from one TBP to the other. In reality, it needs to move from vacancy to vacancy through the electrolyte, but in a brick-layer polycrystalline material, which is what most electrolyte materials can be represented as, this is a valid assumption [17], [67], [68], [69]. The ionic resistivity can then be approximated using a electrical conductivity term, σ_{ion}. The total distance the ion needs to move is simply the thickness of the electrolyte, τ_{elt}.

The ionic resistance can then be expressed as

Equation 2.27.

$$R_{ion} = \frac{\tau_{elt}}{\sigma_{ion} A_{active}} \tag{2.27}$$

R_{ion}	Ionic resistance experienced by an oxygen ion passing through the electrolyte
τ_x	Thickness of the component x
σ_{ion}	Ionic conductivity of the electrolyte
A_{active}	Active cell area- the surface area of an SOFC (element) orthogonal to the flow that performs a reaction. For an individual element, this is its length along the Z-axis multiplied with its width

The cross-sectional area that the ion flux moves through is equal to the contact area of the electrode and electrolyte, which will be defined as the *active surface area* A_{active}. This follows from the dimensions of the element: The width of the element along the edge it is instantiated on, and the depth into the z-coordinate.

2.9.2. Electrical Path

In section 2.2 the neighbour system is described, where every element holds an identifier that can be used to get a reference to the elements in its direct vicinity. This makes the collection of elements behave like a linked-list adjacency representation of a graph. The problem of finding the shortest path (with the lowest electrical resistance) can be reduced to pathfinding on this graph, from the current node to the closest current collector. Because the cross-section of the mesh is constant in the Z-axis, the shortest path will always be along the same depth coordinate, except if the in-plane temperature gradient changes so drastically that the change in conductivity is significant. It is assumed that this will never be the case, and hence all paths are in-plane. Therefore, the search space reduces to only two physical dimensions, which speeds up the pathfinding algorithm. The electrical path should be closed to whatever current collector might have the path of least resistance, even in the case where multiple current collectors are available. The problem, now reduced to finding a representative electrical resistance for all of the elements that this path passes through, is graphically abstracted using Figure 2.12.

Without a good heuristic function, because of the unstructured graph, this problem can best be solved using a (greedy) breadth-first search [70] sorted based on a cost function equal to the resistance.

The path should go directly from the TBP to the edge of the current collector. This means that the path through every element, a straight line, has both a vertical (into the diffusion direction) and a horizontal (along mesh edge) component. The definition of the horizontal component is the same for every element– it is equal its width– but the vertical component depends on the horizontal separation. This component stems from the angle that the path needs to make to cross the thickness of the electrode. Solving such a problem is possible, but would require a lot of extra trigonometry, distributed over several elements, meaning many more steps in the pathfinding process. As the pathfinding is already very resource-intensive (compared to the rest of the program), two simplifications are made:

- All reactions take place at the center of the element
- The vertical part of the electron path is fully within the first element itself, and any neighbouring elements that the current needs to pass through only have a horizontal component.

Applying these assumptions simplify the problem: the path described would be like as if the current first moves out diagonally from the TBP to the edge of the electrode, and then moves horizontally along the outer shell. Since the horizontal distance through an element is only directly related to its dimension, this component of the resistance is constant. The horizontal orientation of this path implies that the cross-sectional area the current can pass through is comprised of the thickness of the electrode and the z-length of the element. As such, the horizontal resistance can be expressed as Equation 2.30. It will always slightly overestimate the total path length, but depending on the local state of the starting element it can either have the effect of

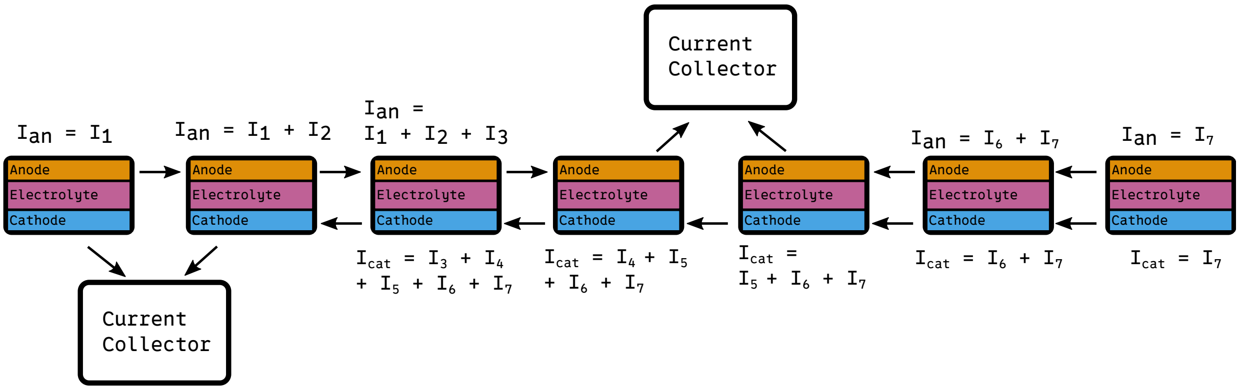

Figure 2.12: A graphical representation of the problem that the electric part of the ohmic model tries to solve, including the inverse path problem.

overestimating the resistance (if the temperature of the starting element is higher than that of the other elements its pat passes through), or underestimating the resistance (vice versa).

This allows the calculation of the horizontal resistance to be isolated from the rest of the path calculations. This component can be calculated once, and reused for all other elements whose electric path passes through it, significantly reducing the amount of arbitrary function evaluations required.

The final piece of the puzzle is the resistance of this diagonal partial path in the sourcing electrode. The resistance due to the path inside the source electrode can be determined geometrically as Equation 2.29. Since the path is diagonal, the average cross section of the active surface area (vertical direction) and the value used for the horizontal direction is used. Here L_w is the length of the element along the edge it is defined. τ_x is the thickness of the electrode. σ_x is the effective electrical conductivity of the electrode (which will be covered in subsection 2.9.3). z is the length of the element in the z-direction.

$$R_x = R_{x,self} + \sum_i R_{x,hor_i} \tag{2.28}$$

$$R_{x,self} = \frac{\sqrt{L_w^2 + \tau_x^2}}{\sigma_x \ \frac{1}{2}(A_{active} + \tau_x L_z)} \tag{2.29}$$

$$R_{x,hor} = \frac{L_w}{\sigma_x \tau_x z} \tag{2.30}$$

$R_{x,self}$	Electrical resistance experienced due to the short path that an electron has to take through an electrode x from the center at its TBP to the edge of its outer surface
$R_{x,hor}$	Electrical resistance orthogonal to the diffusion direction, along the plane of the active cell area for an electrode x of the PEN assembly
R_x	Electrical resistance experienced inside of an elecrtrode x
L_w	Length of an element in the edge direction (x-coordinate), orthogonal to the diffusion direction and the flow direction
τ_x	Thickness of the component x
σ_x	Electrical conductivity of an electrode x
L_z	Length of an element in the z (flow-wise coordinate) direction

Splitting up the resistances in this way also simplifies the process of storing the path resistances. Instead of storing the full path resistance, it the resistance can be reconstructed at runtime. To be able to get the resistances from any element, each PEN now only needs to retain a list of identifiers of all the elements that are between it and the closest current collector. When the ohmic model is evaluated, these elements can be resolved as described in subsection 2.13.5, and the horizontal resistances retrieved from them directly. New values for the horizontal component of the resistance are calculated as part of the iteration scheme for each individual element. The electrical conductivity must be evaluated either way to determine the vertical part, after which this value can be reused to determine the new horizontal resistance. For the ohmic model at iteration i, this means that the values used for the electrical resistance for any neighbouring elements will always be that of iteration $i - 1$, but as convergence approaches the error this introduces should approach zero.

Because calculating the shortest path between an electrode and the closest current collector is a relatively expensive operation, it is not done every operation. It is done every n iterations, where n is a setting that is exposed to the user (defaulting to 100).

It is once again emphasised that the path for the anode- and cathode side are independent, and might have unique solutions.

2.9.3. Electrode Conductivity

Determining the electrical conductivity of an electrode is not as straightforward as simply evaluating some material property. This model focuses on the use of multicomponent electrodes that have a distinct (metallic) current-carrying phase (Mixed Ion-Electron Conductor (MIEC)-type electrodes are not currently implemented). It is a fair assumption to say that all of the current is carried exclusively by this phase, as the electrical conductivity of the other phase is very low [71]. This means that all clusters of the metallic phase must be connected to be able to form a closed circuit.

The probability of this occurring is defined as the (electrical) **percolation probability**. Below a certain percolation threshold, such uninterrupted clusters do not occur [72]. When this threshold is met, it can be shown that most clusters that form do in fact form continuous clusters, meaning that all current can run through the electric phase from any point in the TBP [73]. The percolation probability is given in Equation 2.31. [55], [72], [74]. Here $Z_{el,el}$ is the average coordinate number for a particle of electrically conductive material to be in contact with another particle of the same phase. For random packing of equally sized spherical binary particles, this is directly proportional to the volume fraction of the electrical phase, as given in Equation 2.32 [74].

$$P_{el} = \left(1 - \left(\frac{4.236 - Z_{el,el}}{2.472}\right)^{2.5}\right)^{0.4} \tag{2.31}$$

$$Z_{el,el} \approx 6\phi_{el} \tag{2.32}$$

P_{el}	Percolation probability
$Z_{el,el}$	Coordinate number for percolation theory
ϕ_{el}	Volume fraction of the electrically carrying phase in a composite electrode (1 is fully metallic, 0 is fully other material)

The relation given in Equation 2.31 must be used with care however. At values higher than $\phi = 0.706$, the evaluated function yields a value of more than 1. Similarly, if the function is evaluated at a value of lower than $\phi = 0.162$, it also returns values higher than 1. Because this equation represents a probability, the output is clamped to the unit range 0-1.

This percolation probability and volume fraction can now be used to express an effective conductivity for the composite material that takes into consideration the indirectness of the path taken, as well as the unlikely event that there is no direct connection from one point to another, per Equation 2.33 [32], [33].

$$\sigma_{el_{eff}} = \sigma_{el}\left((1-\varepsilon)\phi_{el}P_{el}\right)^{3.5} \tag{2.33}$$

σ_{el}	Electrical conductivity of the electrically carrying phase of an electrode (i.e. Nickel in the case of YSZ)
ε	Porosity, how much of the porous material is void
ϕ_{el}	Volume fraction of the electrically carrying phase in a composite electrode (1 is fully metallic, 0 is fully other material)

2.9.4. Contact Resistance

The interface between the electrode and the current collector is never perfect. This introduces an additional resistance, which is expressed as a contact surface resistivity. This value is added at the end of every path, and is handled as a material parameter.

2.10. The Thermal Model

Because the model is only concerned with finding a steady-state temperature, a heat balance can be set up for every element, knowing that each local balance must sum to 0. What follows now is an outline of the terms that make up said balance, shown in Equation 2.34. In this equation, the subscript w is used to denote other neighbouring elements. The subscript v is used to denote other PEN elements whose shortest path to a current collector passes through this element (see subsection 2.9.2). f is used to describe the fluids that this element touches- for the PEN the fuel and oxidiser, but for a current collector this can be any.

As a reminder: The elements work on a finite difference basis. The temperature is assumed to be the same everywhere in the element. There are no local gradients inside the element, only *between* elements.

$$\dot{Q}_{gen} + \dot{Q}_{ohm} + \sum_{w} \dot{Q}_{ohm_v} + \sum_{w} \dot{Q}_{cond}(T, T_w) + \sum_{f} \dot{H}(T, T_f) + \sum_{f} \dot{Q}_{conv}(T, T_f) = 0 \quad (2.34)$$

$\dot{Q}$	Heating power
$\dot{Q}_{gen}$	Heat generation due to (exothermic) irreversibility of the chemical reaction
$\dot{Q}_{ohm}$	Heat generation due to ohmic losses inside of the element
$\dot{Q}_{cond}$	Heat conduction with a neighbouring element
$\dot{H}$	Energy transfer associated with a mass flow leaving or entering the element with a certain temperature, causing a net convective term
$\dot{Q}_{conv}$	Convective heat transfer between a solid element and a fluid

Both the PEN and CC elements have the same terms. They will only be elaborated upon for the PEN, but the implementation for the CC is effectively identical, notwithstanding some material property calculations. Both have conduction and convection terms. Also present is an ohmic heating term; $Q_{ohm_{v \to w}}$ represents heating due to the total current running through this element. For a CC, this is the total current collected. For a PEN this is the generated current, including the current that runs through here passively from other elements to reach a CC.

In addition to this commonality, the PEN elements have some additional terms:

- A source term due to the electrochemical reaction, as fuel cells operate exothermically.
- Fluid exchange with the bulk fluids for the fluid entrapped in the porous structure of the electrodes. This fluid leaves at the PEN temperature, and enters at the bulk fluid temperature, causing a net enthalpy flux.

2.10.1. Radiative Heat Transfer

The majority of models in literature do not consider radiative heat transfer. Stam et al. [75] concludes that the effects of radiative heat transfer are generally negligible. Ota et al. [76] presses that an exception to this general rule of thumb is loosely packed tubular fuel cells. No such research could be found into monolithic fuel cells concerning this assumption, but it can be shown that for more tightly packed and minified cell assemblies, the relative impact of radiative heat transfer decreases [26]. The added complexity and computational cost of implementing such functionality are prohibitive, and for the seemingly minimal gains in terms of accuracy achieved, it was therefore decided not to model this behaviour at this time.

2.10.2. Solver

For all solid and fluid elements, the local state implicitly depends on the element temperature. The heat and mass flux entering from other elements is determined using the temperature of the previous iteration. Almost all terms in Equation 2.34 are implicitly dependent on the temperature of the element. These must therefore be placed inside of the iteration loop. At this point the root finding procedure should be self-evident- The same root-finder as used in other parts of the code can be used to solve this balance, and the bounds and solver settings are exposed through the API.

2.10.3. Source due to Reaction

Part of the electrochemical reaction that takes place is irreversible, causing a heating term. An entropic loss therefore directly causes a heating term, Equation 2.35, proportional to the local reaction rate (posed in Equation 2.37) [14], [77].

$$-\dot{Q}_{gen} = rT\Delta s \tag{2.35}$$

$$\Delta s = \sum_p \nu_p s_p(T) - \sum_r \nu_r s_r(T) \tag{2.36}$$

$$r = \frac{jA_{active}}{zF} \tag{2.37}$$

r	Reaction rate, causing a change in species
Δs	Molar (intensive) change in entropy due to a reaction
ν_i	Stoichiometric coefficient of the reaction for species i
s_i	Intensive (on mass basis) entropic value of species i relative to some reference value

In Equation 2.35, Δs is the change in (specific) entropy per mole over the reaction. This is the entropy balance (Equation 2.36), for which the individual species' entropies are parametrised as a function of temperature using the same polynomials as used in subsection 2.6.1 [39]. Since this reaction (Equation 2.5) goes from more molecules to fewer molecules, this results in a negative number [78]. In Equation 2.37, $z = 2$ represents the amount of electrons transferred during the reaction.

2.10.4. Ohmic Heating

As described in subsection 2.9.2, both electrodes host an (independent) current. Electrical currents always incur a loss due to electrical resistance, which causes heating. Consequently, R_{ohm} has two components: one for the anode, and one for the cathode. The procedure following is described for a generic electrode, and applied twice respectively.

Determining the electrical resistance in the electrodes is already covered in detail in section 2.9. The electrical resistance for this element calculated in the ohmic model is reused. This can then be related to an ohmic heating term per Equation 2.38. The cached resistances already contains two values: One for the path along the entire element along the mesh edge (as seen by current that passes through this element), and one for the average path that the current generated in this element takes. The former is multiplied with the currents in the other elements whose current runs through this element (their currents are resolved using the method described in subsection 2.13.5), and the latter with the currents generated in this element. The two are them simply summed to get an all-encompassing heating term.

$$\dot{Q}_{ohm} = jA_{active}R + \sum_v j_v A_{active,v} R_{hor,v} \tag{2.38}$$

2.10.5. Conduction to Neighbouring Elements

The neighbours are resolved with the same method as described in subsection 2.13.5. However, since the resulting element can be either a PEN or a CC, this functionality is set up using a `trait` so that dynamic dispatch can be used to generalise behaviour for both element types. This sets up a shared interface for functionality such as determining the thermal conductivity.

This part of the thermal model works using the method of thermal resistances, expressing every interaction with other elements or fluids in analogy to a circuit [79]. For conduction, the thermal resistance is depicted in Equation 2.39. Here L is the length along which conduction takes place, which is the length of the element, and A_n is the area through which conduction takes place– A *normal* surface area along the edge. For the side of element, this is (the sum of) the thickness(es of each layer) multiplied with the length in the z-direction, $A_n = L_z\tau$.

Since the thermal conduction takes place between the two elements, the average thermal resistance of both this element and the other element is used.

$$R_{t,cond} = \frac{L_w}{\kappa_{eff} A_n} \tag{2.39}$$

$R_{t,cond}$	Thermal resistance of conductivity between two elements
L_w	Length of an element in the edge direction (x-coordinate), orthogonal to the diffusion direction and the flow direction
A_n	Area between two neighbouring elements. For the PEN, its thickness times its depth in the Z-axis

For the current collector, determining the thermal conductivity κ is relatively straightforward as it is simply a material property. For the PEN elements, this is not so simple as it is a compound of three different materials. All three components need to be represented by a single mean value, introducing the need for an averaging procedure. In reality this would best be done on a mass basis, but densities for the individual components are generally unavailable in literature. Instead, the thickness of the components is used as a weighing parameter, shown in Equation 2.40.

$$\kappa_{PEN} = \frac{\kappa_{eff,cat}\tau_{cat} + \kappa_{eff,an}\tau_{an} + \kappa_{elt}\tau_{elt}}{\tau_{an} + \tau_{elt} + \tau_{cat}} \tag{2.40}$$

The thermal conductivities of the electrodes are not only dependent on a material property, but also on the fluid entrapped in them. An effective thermal conductivity is defined in Equation 2.41. Here κ_f is the thermal conductivity of the fluid inside of the porous electrode.

$$\kappa_{eff,x} = \varepsilon\kappa_x + (1-\varepsilon)\kappa_f \tag{2.41}$$

It is assumed earlier in section 2.8 that the fluid only convects orthogonally to the bulk flow-directly into the electrode, towards the electrolyte. This is a simplification that has ramifications for the thermal model too. In reality, the thermal gradient between two elements would cause a convection term, causing the effective heat transfer between two neighbouring electrode sections to be even higher. The actual temperature gradients between elements directly next to each other is however generally not very high, so the net convective term is negligible [51]. Therefore, this is currently not modeled, and the assumption sustained.

This procedure is repeated for every neighbouring element, in case an element has multiple neighbours.

2.10.6. Enthalpy Flux with fluids

Oxygen and hydrogen are used up and water is created at a rate proportional to the current generated. The mole consumption rate for oxygen is given in Equation 2.45, and the mole consumption rate for hydrogen in Equation 2.46. As the system is in steady state, the mass balance states that the same amount of fluid needs to leave and enter the control volume. These flows have their own associated temperatures, driving an enthalpy flux term. It is assumed that only the species partaking in the reaction are exchanged; there is no forced enthalpy transfer due to the funnelling of species that don't partake in the reaction, such as nitrogen.

Hydrogen and oxygen enter at the temperature of the bulk fluid (which is almost always lower than the PEN temperature). It is assumed that the water is in equilibrium with the rest of the PEN, having reached the same temperature by the time it leaves. Water therefore leaves at the temperature of the PEN element.

Compounding all the previous statements into a mathematical equation, the heat contribution as enthalpy flux due to the entering and leaving species can be expressed as Equation 2.42 for oxygen and hydrogen, and as Equation 2.43 for water (both are specialised forms of Equation 2.44).

$$\dot{H}_{\mathrm{O_2},\mathrm{H_2}} = \dot{y}_i M \left(h(T_f) - h(T_{ref})\right) \tag{2.42}$$

$$\dot{H}_{\mathrm{H_2O}} = -\dot{y}_{\mathrm{H_2O}} M_{\mathrm{H_2O}} \left(h(T) - h(T_{ref})\right) \tag{2.43}$$

$\dot{H}$	Energy transfer associated with a mass flow leaving or entering the element with a certain temperature, causing a net convective term
$\dot{y}_i$	Mole flow rate of species i
M_i	Molecular weight of species i
h_i	Intensive (on mass basis) enthalpy value of species i relative to some reference value

As seen in Equation 2.42, the oxygen and hydrogen flows enter at the bulk fluid temperature. To the solver, it is only dependent on the reaction rate (which is itself only a function of current density, as given in Equation 2.37). These can therefore be calculated once, outside of the root-finding procedure, and reused. Note that the last flux term, enthalpy flux due to created water leaving, cannot be isolated, because it leaves with the temperature T.

The fluid enthalpies as a function of their temperature are evaluated using the same polynomials used everywhere else in this work [39].

2.10.7. Convection with Fluids

The convection with the fluids will be covered in subsection 2.12.3, but performed with variable solid element temperature and a fixed fluid temperature. Its sign is also flipped, as the equations in that section consider heat going from the fluid to the PEN as positive, instead of the other way around.

2.11. Fluid Mixture

Albeit not necessarily a model itself, certain functionality pertaining to fluids is reused throughout all the models that interact with the fluids in some way. This section covers how these common operations are performed. All fluids in this model are represented as mixtures of the three main components: Hydrogen, oxygen, water and nitrogen. Air is assumed to consist of nitrogen and oxygen only (no trace gases).

The core principle of how fluids are modeled is the translation of properties from an individual specie to that in a mixture. Tables showing all the properties used for each of the four main components can be found in Appendix B. Enthalpies, entropies (and compound quantities like Gibbs free energy) are modeled using polynomial fits from Burcat and Ruscic [39], which is a modern compilation often referred to as *NASA7 polynomials* or *NIST polynomials*.

A `FluidMixture` object is simply a collection of the total composition of the fluid on a rate basis: a mole rate of water, oxygen, hydrogen and nitrogen. As additional state, it holds a temperature and static pressure. It does not need definite information on its shape or alignment, but cross-sectional area is also contained, used for calculating velocities.

All 'fluid' properties are related to species properties of the components in the mixture. These single-specie properties are contained in a `FluidSpecieProperties` object, one of which exists for every specie. Individual enthalpy rates can be accessed this way, and mixture properties can be based on composition weighted by species presence. The mixture model is relatively simple, only taking summative or average values, and not attempting to model internal fluid interactions.

An example of a fluid mixture property that is determined by taking the sum of its components' values is the enthalpy rate (as used in the calculations for the secondary flows in the fluid model), as depicted in Equation 2.44. The same functionality exists for moles rates, and mass rates,

For average properties, generally averaging is done on a basis of mass: Thermal conductivity, enthalpy, dynamic viscosity, Prandtl number, etc.

Two particular average properties are averaged on a mole basis: specific gas constant, and average molar mass. Density is determined using the average specific gas constant, so this is indirectly also on a mole basis.

$$\sum_i \dot{y}_i M \left(h_i(T_f) - h_i(T_{ref})\right) \tag{2.44}$$

2.12. The Fluid Model

The fluid model works a little differently from the other sub-models, mostly in that it works almost exclusively on the fluid elements. Because these elements are on a finite volume basis instead of on a finite difference basis, implementation also differs. Conceptually, the fluid model works similarly to the thermal model, in that the central problem it solves a balance equation. Here the actual balance being solved is however twofold: conservation of energy as well as conservation of mass.

2.12.1. Conservation of Mass

The conservation of mass makes use of the fact that the directions of the mass flow are already known: There will always be an upstream mass flow entering from the z-coordinate prior to the one that this fluid is in. For the very first layer, the upstream is considered the provided inflow conditions.

Additional mass flows enter from the PENs, depending on their reaction rate and species production rate. These will be referred to *secondary incoming flows*. In the case of the fluid being used as a fuel, this entering mass flow is exclusively water, with each term being given as Equation 2.47. For the oxidiser fluid, only oxygen is extracted and no other fuel is returned back into this flow, so this term is zero.

There are also *secondary leaving flows*, which, as one might have come to expect, are flows that go into the PENs. These mole rates are quantified in Equation 2.46 and Equation 2.45 for the fuel and oxidiser respectively.

One term remains, which is the flow going downstream. This mass balance for each species i, constructed in Equation 2.48, can therefore be closed explicitly.

$$\dot{y}_{\mathrm{O_2}} = \frac{I}{4F} \tag{2.45}$$

$$\dot{y}_{\mathrm{H_2}} = \frac{I}{2F} \tag{2.46}$$

$$\dot{y}_{\mathrm{H_2O}} = \frac{I}{4F} \tag{2.47}$$

$$\dot{y}_{m,z} = \dot{y}_{m,z-1} + \sum_w \dot{y}_{m,w,in} - \sum_w \dot{y}_{m,w,out} \tag{2.48}$$

2.12.2. Energy Balance

Each of the flows described in subsection 2.12.1 has a certain enthalpy, meaning that they have an accompanying enthalpy flux. This was detailed in subsection 2.10.6. The largest term in the balance comes from upstream: A high mass flow rate with a certain enthalpy, as calculated according to the procedure in section 2.11.

The bookkeeping details required for the secondary flows is already covered in subsection 2.12.1; Flows of water coming from the PEN enters at the (elevated) temperature of the PEN, whereas flows diffusing into the PEN leave at the fluid bulk element temperature. Depending on the fluid, this term can be zero. For example, the oxidiser has no flow entering, so no net enthalpy flux.

An additional method of heat transfer from the solid elements exists as convection. The implementation of this is outlined in subsection 2.12.3.

This leaves one unknown term: the downstream leaving enthalpy flux, at a temperature of the fluid bulk.

This means there are $1 + n_w$ unknown terms where n_w is the amount of PENs that have a flow of hydrogen going into them from this element. Since the mass flow going downstream and into each of these elements is known, the mixture enthalpy can be implicitly solved for the temperature. This is again a job for a root-finder.

$$\dot{H}_{upstr} - \dot{H}_{downstr} + \sum_w \dot{Q}_{conv_w} + \sum \dot{H}_{w_{in}} - \sum \dot{H}_{w_{out}} \tag{2.49}$$

2.12.3. Convection with Solid Elements

In addition to heat transfer due to enthalpy fluxes, there is an additional heat transfer mechanism between the solid elements and the fluid. There always exists a boundary layer near

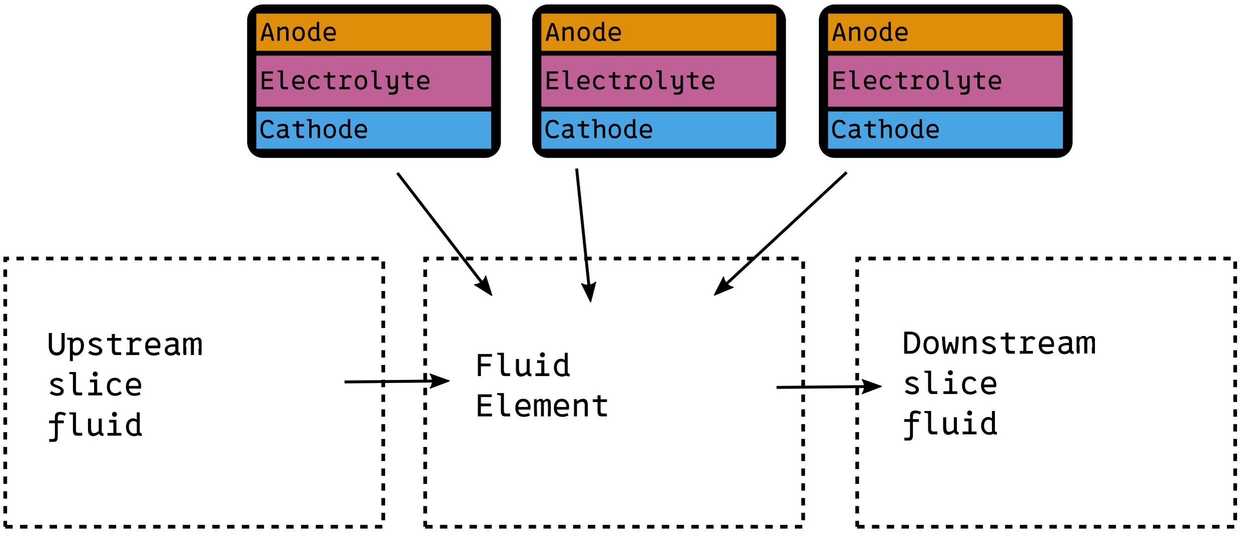

Figure 2.13: A visualisation of the balances set up in the fluid solver.

the edges of the fluid channels, meaning there is some form of convection.

This process is modeled using Newton's law of cooling, given in Equation 2.50. Here A_{active} is the active cell surface area of the element w (or equivalent for a CC). The convective heat transfer coefficient h is calculated from a Nusselt relation as given in Equation 2.51. Here D_{hy} is the characteristic length, which is equal to the hydraulic diameter of the fluid channel.

$$\dot{Q}_{conv} = hA_{active}\left(T_f - T_w\right) \tag{2.50}$$

$$h = \frac{\mathrm{Nu}\,\kappa_f}{D_{hy}} \tag{2.51}$$

h	Convective heat transfer coefficient
ε	Porosity, how much of the porous material is void
ϕ_{el}	Volume fraction of the electrically carrying phase in a composite electrode (1 is fully metallic, 0 is fully other material)
D_{hy}	Hydraulic diameter

The flow regime in SOFCs can vary significantly [29]. Nusselt number correlations are typically only applicable in certain ranges of Reynolds number and usually only apply to laminar or turbulent flow and for very specific geometries. Instead of trying to find a single relation that can represent all cases, three different schemes were implemented. To be able to provide a good estimate for a variety of conditions, a system was set up that automatically switches between calculation schemes based on local Reynolds number.

First is a method from Mills and Coimbra [79], which gives a constant Nusselt number of $\mathrm{Nu} = 3.66$ for a laminar internal flow of a Reynolds number less than 3000, as long as the length of the channel is much larger than the hydraulic diameter.

If the Reynolds number is lower than 10^6 but higher than 3000, the model switches to using the Gnielinski correlation (Equation 2.52), utilising Petukhov's formula (Equation 2.53) for the friction factor Φ. Mills and Coimbra [79] notes that the friction factor states that the Gnielinski correlation is valid for any low Reynolds value up to 5×10^6, which also holds as long as the boundary layer is fully developed, which is the case if the length of the channel is much larger than the hydraulic diameter.

$$\mathrm{Nu} = \frac{\frac{\Phi}{8}(\mathrm{Re} - 1000)\,\mathrm{Pr}}{\left(1 + 12.7\sqrt{\frac{\Phi}{8}}\right)\left(\mathrm{Pr}^{\frac{2}{3}} - 1\right)} \tag{2.52}$$

$$\Phi = \left(0.790\ln(\mathrm{Re}) - 1.64\right)^{-2} \tag{2.53}$$

If the Reynolds number is larger than 10^6, the model switches to the well-known Dittus-Boelter relation (Equation 2.54). It holds that solid elements are always higher in temperature than the fluids, as the solid elements could have source terms, whereas the fluids do not. Hence, the convection is always cooling (relative to the solid element), for which a value $n = 0.4$ is to be used [79].

$$\mathrm{Nu} = 0.023\,\mathrm{Re}^{\frac{4}{5}}\,\mathrm{Pr}^{n} \tag{2.54}$$

Equation 2.53 and Equation 2.54 rely on the Reynolds number, which is calculated relative to the hydraulic diameter of the fluid channel. It is planned to implement functionality to calculate this automatically from the geometry, but to reduce scope this value is to be input manually on an edge during mesh creation (and as such propagated to the elements). In addition, for Equation 2.54 the Prandtl number is calculated as given in section 2.11.

2.13. Architecture of the Program

A common problem with research- and engineering software is that they perform poorly, are unintuitive to use, ill-documented, not tested thoroughly, obfuscated or obtuse, not extendible, hard to read, or hard to integrate. A lot of thought was put into the architecture and implementation to ensure this is not the case for GOOSE.

The simulation software central to this work is implemented using **Rust**, a compiled systems programming language without garbage collection, and am emphasis on memory safety. Rust has quickly risen in popularity in the software engineering scene in recent years, and is slowly gaining popularity and adoption in STEM fields as well [80].

It lends itself very well to writing high-performance, fully parallelisable code (which is heavily used as covered in section 2.2), perfect for a high-speed library where calculation times are important. At present, the model is able to finish calculations for medium-resolution meshes (6000 elements) in the order of $30\,\mathrm{s}$, and for very high-resolution meshes (50000 nodes) in the order of $8\,\mathrm{min}$.

2.13.1. Extendability

Being a simulation software specifically built to be able to aid in exploration of a relatively unknown, quickly-evolving field, over a design space as wide as possible, it is unequivocal that some parts of the implementation as it exists now will be considered archaic in a short time frame. For research software like this, it is especially important to stay flexible, maintaining the option to extend to be able to keep up with recent development. This is why a very modular architecture is used, where swapping out parts should be possible even without knowing the ins and outs of every part of the entire program beforehand. Further enabling this is the diligent use of unit testing to ensure the boundaries and expected behaviours of individual sub-systems are respected even after heavy modification or refactoring, which is covered in more detail in section 3.2.

The implementation of the software in Rust also again aids in this process. The Rust toolchain is available on almost every platform, and building the program is done with a single command- no complex setup necessary.

The author of this work strongly believes that in the scientific spirit of collaborative advancement, open-sourcing software is of the utmost importance. Any party interested in aiding the further development of GOOSE is strongly encouraged to reach out and join in the continued development process.

2.13.2. Integration

Interoperability and integration into existing pipelines is very important for research and engineering software to ensure that it can be used efficiently and easily in a broad context[81], [82]. Although Rust is arguably a fantastic language for implementing simulation software in, many analyses and existing pipelines are centred around other tools and programming languages such as Python or MATLAB. To enable the software to be used with these tools, the program is implemented with an Application Programming Interface (API), which allows users to access its functionality without having to understand how the program is implemented. The main functionalities of the API can be split up in the following categories:

- Defining operating conditions, solver settings, and other static parameters to be used to run a simulation case
- Parametrically constructing a mesh to be simulated, using the mesher detailed in section A.2.
- Expose functionality for returning simulation data, be it by saving it to disk or returning it directly for further analysis integrated into the host pipeline process.

The simulation software is then packaged and distributed with several different bindings:

1. A Rust library, for integration with other Rust programs
2. A Python library, accessible through pip and PyPI.
3. A C Foreign Function Interface (FFI) interface, which can also be used in MATLAB or Simulink
4. An executable, allowing the program to be run on any computer directly. Instead of using an API, the executable is interacted with using text files, similar to other legacy tooling. It must be stressed that this exists as a fallback, and if possible, any of the other bindings should be preferred for streamlining interoperability and ease of use.

2.13.3. Compile-time Dimensional Analysis

Common mishaps in programming scientific software lie not in the misunderstanding of the fundamental physical phenomena that are being modelled (fortunately), but rather in small uncaught implementation errors that manage to slip through. The trivial- the obvious- forgetting a minus, making a mistake in unit conversion, and improperly balancing brackets. Some of these problems can only be caught by meticulous testing and review, which is why GOOSE uses extensive unit testing. Others can be brought to light with a more elegant, modern solution. Rust, being a statically typed language (all values have a 'type' which is known at compile time, akin to C, unlike Python), lends itself very well to compile-time dimensional analysis. Instead of representing a length, a speed, and time simply as a number (e.g. `f64`), they are assigned a unique type representing their dimensionality. Length and speed are treated inherently different at compile time. This ensures that operations like subtracting a length from time are caught by the compiler, instead of deferring this responsibility to the programmer. These types can be inferential: an operation like division can represent the division of length by time, yielding a value of type speed. Under the hood, all the values are stored in their SI base units. The notion of units only comes up when transforming the values out of their typed domain back into generic floating point containers by explicitly requiring a unit to be used. This is especially helpful as material parameters and electrochemical eqations rarely use base SI units. This also helps the user avoid such mistakes when inputting new material data.

The implementation of such a system in GOOSE ensures that a whole class of implementation errors could be avoided. This incurs a bit of cost in development time, but this greatly pays off at the time of testing, verifying, and even documenting the code.

2.13.4. Root-finding

As many of the equations this simulation paradigm are balance equations that need to be solved implicitly, the amount of function evaluations required to find the solution where a variable is zero can be reduced tremendously by using good general-use root-finding algorithms. Simple root-finding implementations exist in the Rust ecosystem, but there were technical challenges in returning additional state (other than the solution of the value itself, such as for the electrochemical system the build-up of all overpotentials). Additionally, error information is also typically not conserved, which is important in this simulation package to be able to find the root cause of problems faster. A root-finding procedure based on Brent's method [40] was developed and implemented, which did meet the above criteria. In the spirit of modularisation, this functionality has been released separately from the GOOSE package to be used in other applications as well.

2.13.5. Referencing Other Elements

Many operations inside the models rely on referencing other entities in the mesh. One example is the referencing of neighbours, solid elements that are adjacent to some solid element as described in section 2.2, to create gradients.

In most programming languages, this would most likely best be tackled by using *pointers*. Rust however, does not have the concept of pointers. Instead, it uses *references*, which are not nullable. An object can have any large amount of *non-mutable* references. Reading from memory is always safe if the address is not being written to. As soon as one wants to edit the value at that location in memory, this can not be guaranteed. In Rust, this concept is referred to as *mutability*. You can only write to a part of memory from one place at a time, which results in only a single mutable reference being allowed. As such, a mutable call also voids any non-mutable reference. Creating a reference to an object is called '*borrowing*'. Rust's borrowing system is very powerful, as it removes an entire family of memory management related bugs. However, for data structures where many instances keep interdependent relations, this becomes much trickier to handle:

Firstly, you need to be able to prove to the compiler that any references are valid for as long as an object can be interacted with. This is done by marking object and functions using *lifetimes*, which is widely considered as a notoriously hard and laborious process [83].

A second issue arises in writing to an object: Doing so mutably would void all the references, which is not allowed. The solution to this is wrapping these references in some sort of object that allows for temporary mutability. In threaded programming, this is usually done with *mutexes*. However, using mutexes introduces additional complexity, as well as significant overhead in locking and unlocking access to a shared object It would also not solve the first problem.

Given the amount of calls that reference other elements, a different, simpler alternative was used: Other elements and materials are stored with an identifier, which are resolved using the mesh and a centralised material database once at the start of every iteration as a non-mutable reference.

A `MaterialDatabase` is established which stores all the materials indexable with a material name. The `Mesh` struct contains all the elements and fluids already, so it gains the responsibility for the functionality to resolve elements and fluids.

The elements store constant identifiers that are used to resolve to the references at runtime. To retain the spirit of designing the program in the Rust way, it is best to try to catch errors at compile-time. Mixing up identifiers is avoided by ensuring that identifiers to the fluids, PENs and CCs should not be interchangeable. As a result, one cannot accidentally index a fluid with a PEN identifier and receive an unexpected fluid, which would be very hard to debug. Solid elements still have some shared functionality, such as in the thermal model. Therefore, the following two representations are defined for storing identifiers to other elements:

A `FluidId` is used uniquely only for fluids. A `SolidElementId` is used for both the current collector and PEN elements. It contains an extra field which defines the type of element it indexes: it can be either `Pen` or `CC`.

2.13.6. Material System

A similar problem in referencing other data at runtime as it does between elements exists for the material system. GOOSE allows for assigning materials to solid elements. All instances could have exactly the same material, or you could have multiple materials for more advanced (or experimental) fuel cell set-ups. However, in practice the amount of materials one will work with will most likely be relatively small. For this reason, as well as cache optimality, it makes more sense to store only one copy of the material data, and reference this when evaluating material properties. In the software implementation this is handled by a `MaterialDatabase`, of which only one can exist. It holds data separated by material type, separated for electrodes, electrolytes, and current collectors. Materials are registered against this database, and resolved by a string identifier from the mesh as described in subsection 2.13.5. For a list of material parameters to be input, see subsection A.3.5 and the sections following it.

There are various ways of actually encoding material parameters. Using a `EmpiricalFunction` object, the value can be given in several formats, with the software automatically resolving the type used in runtime. The following input formats are available:

- Constant value
- A linearly interpolated series of values for given temperatures
- A linear function of temperature in the form of $q = a + bT$
- An Arrhenius type function $f(T) = A\exp(-\frac{B}{T})$
- An Arrhenius-like function that is extra divided by the temperature $f(T) = \frac{A}{T}\exp(-\frac{B}{T})$
- An Arrhenius-like function with dependence on the partial pressures of oxygen, which is chiefly used in cathode to parametrise exchange current density, as given in Equation 2.56 [32], [33], [54], [76], [84]
- An Arrhenius-like function with dependence on the partial pressures of hydrogen and water, which is chiefly used in anode to parametrise exchange current density, as given in Equation 2.55 [32], [33], [54], [76], [84].
- An arbitrary function of temperature, implemented using a `closure` (anonymous function, or lambda)

$$j_{0_{an}} = j_{0_{ref}}^{an} \left(\frac{p_{\mathrm{H_2}}^{TBP}}{p_{\mathrm{H_2}}^{ref}}\right)^{A} \left(\frac{p_{\mathrm{H_2}\,O}^{TBP}}{p_{\mathrm{H_2O}}^{ref}}\right)^{B} \cdot \exp\left(-\frac{E_{act_{an}}}{R}\left(\frac{1}{T} - \frac{1}{T_{ref}}\right)\right) \quad (2.55)$$

$$j_{0_{cat}} = j_{0_{ref}}^{cat} \left(\frac{p_{\mathrm{O_2}}^{TBP}}{p_{\mathrm{O_2}}^{ref}}\right)^{C} \cdot \exp\left(-\frac{E_{act_{an}}}{R}\left(\frac{1}{T} - \frac{1}{T_{ref}}\right)\right) \quad (2.56)$$

Charge transfer coefficients used in electrodes always come in pairs, with a forward and a backward term. Simplified forms are also often used, and in the case of symmetry some calculations can be simplified. Such variations are made explicit by making a charge transfer coefficient its own data type, with convenience functions for symmetrical- and standard 0.5/0.5 pairs.

3

Verification and Validation

To prove that the model actually gives realistic results, a validation must be carried out. This chapter covers the validation of the model presented in this work. First, there is a foreword on the process of validating a holistic model, and the difficulties encountered, and why the verification and validation strategy that has been used is chosen. This is followed by several sub-sections detailing sub-system-level verification and validation. Closing this chapter, a larger full validation case is covered in section 3.11.

As a reminder– The entirety of GOOSE is written in such a way that compile-time dimensional analysis is performed, details of which can be found in subsection 2.13.3. While not verification in the traditional sense of the word, such a procedure also functions to reduce the amount of implementation errors, for which it is also briefly mentioned here.

3.1. On the Process of Finding Validation Data

To understand the choices taken in the process of validation and verification, some context must be provided. Validating a holistic model like the one presented in this work however is a tough endeavour.

Experimental data that can be used for this purpose is scarce. The majority of literature seems to focus on performance evaluation of button cells, with mostly uniform, controlled operating conditions [48], [85]. Unfortunately the results of these analyses do not always transfer over to performance in an actual stack, where variations in operational conditions along the geometry and depth play a large role. The reason for this bias in research is likely due to resource- and technological limitations. Full stack testing is much more expensive to carry out, and non-intrusive measurement in fuel cells stacks is much more complicated than on button cells [85].

Additionally, most papers reporting on experiments results only provide a very limited set of performance characteristics . The one thing that consistently is provided is a plot showing the current density over operating voltage: a so-called J-V curve (also called I-V in other literature). However, no information is given generally for the outflow: Resulting composition, temperature [19], [30], [86]. An operating temperature is frequently given, but only as a single value at the inflow condition. Rarer are the cases where an actual value measured in the stack is given. This means what it is measured is still only representative of one point in the stack (often the measuring point is also not given), making comparisons of gradients inside the stack impossible, nor is it impossible to quantify if the rest of the stack operates in the same ballpark.

Experimental data –albeit rare– does exist. However, another reason why validating based on said data proved to be very difficult is because of reproducibility of the data given in existing literature. This does not just pertain to the seemingly contradicting results, but is also a remark on the general incompleteness of parameters provided to set up a repetition in the first place. Almost every paper considered for validation leaves out crucial information on geometry, materials properties (or material names entirely), inflow composition, and even operating temperatures [19], [22], [30], [33], [58], [66], [76], [87], [88], [89], [90]. For every missing bit of information, the uncertainty of the validation grows, as these values now have to be assumed. Special attention must be given to the most commonly missing information: material data. This is especially unfortunate, as the majority of input data for GOOSE relates to material information. In the best case, actual values are provided, but in practice this is hardly ever the case. Sometimes material names are provided, but sometimes the names themselves are too non-specific. Simply stating the material is Ni-YSZ does not tell you anything about its percolation, doping or porosity- all of which strongly affect its material properties [91]. With the wide variety in SOFC materials used and their often times minor variations, it becomes a near-Sisyphean task to close the input parameters, as it now requires reverse-engineering the material based on very few known data points.

Many research endeavours sidestep the problem of having to represent material properties or complicated processes by instead simplifying many processes to a single emperical relationship, such as modelling the combined ohmic- activation- and concentration overpotentials using an equivalent electrical resistance, or fitting behaviour to a fuel utilisation factor [19], [21], [22], [23], [24], [25], [26], [27], [28], [92]. While such an approach allows for matching experimentally observed behaviour well, the insights from such a simulation are limited, as it cannot be used for inference in novel situations (different geometries, operating points, scales): it inherently has the same assumptions, limitations and processes directly embedded, allow only for analysis and comparison with other models and experiments of the exact same stack.

All this is to say that, out of many possible validation cases considered, only a single one provided sufficient information to adequately reproduce its results. Ideally, the validation of such a complex model is performed against multiple cases that test the model holistically. It must be emphasised: After immense effort has been put into finding suitable validation cases, validation could be performed against one complete model. Even this validation case properly covers the full extent of the model, so a more thorough procedure had to be devised. To compensate for this, the validation strategy was adapted: In addition to a fully wholistic validation, several smaller validation and verification procedures were carried out for the individual sub-models and modules.

There is always the possibility that more data might exist (e.g. in not openly accessible databases), but after the large volume of sources evaluated, emphasis here should be put on this being a hypothetical.

3.2. Validation in Parts

A grand total of 89 papers were considered for use as validation case for the model. Unfortunately not a single experimental source gives sufficient data to fully validate the model while also containing enough information on the experimental setup to be able to reproduce it. En lieu of alternatives, the search was expanded to also include other simulation-based works of literature. Mainly CFD papers were considered to this end, as they were the most likely to provide more detailed outputs and inputs. Unfortunately here too, reproducibility proved to be a large problem.

For this reason, it was decided to validate the model as best as possible, and to perform extensive verification in addition. Albeit not holistic, it can be shown that at least the subsystems of the model behave realistically. At time of writing total of 112 unit tests are implemented. As some are nested, the actual amount of cases tested is closer to 300, with actual validity checks (assertions) going over 1000+. This means the code base is approximately 90% test-covered. The remaining portion is mostly solver-specific code, and would hence be covered by validation.

Finally, one validation case is set up for system integration, based on the results found in Su et al. [32]. This paper gave the largest amount of output while still being mostly reproducible.

All of the tests mentioned in this section passed. This indicates internal consistency in the model, and shows that the results are as is physically expected.

3.3. Diffusion Model

The diffusion model was validated using data from Zhao et al. [59] and Poling et al. [61]. As described in section 3.3, the most important factor of the diffusion model is the determination of a diffusion coefficient. Zhao et al. [59] gives materials with different doping fractions as well as their measured Knudsen diffusion coefficients. The tortuosity given is matched, with open porosity interpreted as a percentage. A comparison of the resulting values for the Knudsen diffusion coefficients can be seen in Table 3.1 and Table 3.2.

Table 3.1: Knudsen diffusion coefficients for oxygen as determined by this model compared to experimentally obtained values from Zhao et al. [59].

Doping (%)	Model ($\mathrm{cm^2s^{-1}}$)	Reference ($\mathrm{cm^2s^{-1}}$)	Difference %
20	0.21986	0.22	-0.063
22.5	0.37497	0.375	-0.008
25	0.62507	0.624	+0.172
27.5	0.9593	0.959	+0.031

Table 3.2: Knudsen diffusion coefficients for nitrogen as determined by this model compared to experimentally obtained values from Zhao et al. [59].

Doping (%)	Model ($\mathrm{cm^2s^{-1}}$)	Reference ($\mathrm{cm^2s^{-1}}$)	Difference %
20	0.23498	0.235	+0.009
22.5	0.401	0.401	+0.007
25	0.6699	0.667	-0.015
27.5	1.0253	1.025	+0.029

The calculation of the binary diffusion coefficient is verified for known literature values of oxygen-nitrogen in [93]. These values are at lower temperatures, as high-temperature data could not be found. A comparison can be found in in Table 3.3.

Table 3.3: Binary gas mixture diffusion coefficient for nitrogen and oxygen, from this model compared to Astrath et al. [93].

Doping (%)	Model ($\mathrm{cm^2s^{-1}}$)	Reference ($\mathrm{cm^2s^{-1}}$)	Difference %
30	0.210	0.21	+0.180
80	0.274	0.26	+5.385

The same procedure to verify the binary diffusion coefficient was also performed for a nitrogen- and carbon dioxide mixture, presented in Table 3.4. Although not directly representative as this gas mixture is not commonly found in SOFCs, the high temperature makes it worthwhile anyway-high-temperature behaviour of the diffusion model is very important to verify, and this is the only compound where such high-temperature data was found for. As such a verification case in a representative temperature range was prioritised.

Table 3.4: Binary gas mixture diffusion coefficient for oxygen and carbon dioxide, from this model compared to Poling et al. [61].

Doping (%)	Model ($\mathrm{cm^2s^{-1}}$)	Reference ($\mathrm{cm^2s^{-1}}$)	Difference %
590	0.5098	0.52	-1.96

3.4. Electrochemical Model

The electrochemical model is the beating heart at the center of the entire model. It requires several input parameters from several other models, but it itself is not very complex. It needs to determine the Nernst potential, which it then combines with values from other models to get a current density.

One part of the Nernst potential is the standard potential, as given by Equation 2.4. This itself is backed by the Gibbs enthalpy change, which is also parametrised in the code.

To verify that this value is determined correctly, it is evaluated for several well-known temperatures and compared to known values in literature, as presented in Table 3.5. As can be seen, there is very good agreement between the implementation in this code and the reference data, especially at higher temperatures, which is the operating domain for SOFCs.

Table 3.5: Verification of the determined open standard potential with data from Mulder [77].

Temp. ($^{\circ}\mathrm{C}$)	Model (V)	Reference E_0 (V)	Difference %
25	-1.184	-1.23	-3.740
100	-1.167	-1.16	+0.603
400	-1.089	-1.09	-0.092
600	-1.034	-1.04	-0.577
800	-0.977	-0.977	-0.041

Table 3.6: Activation overpotentials for the cathode for given current densities in this model compared to the values in Chan et al. [56].

Current Density ($\mathrm{A\,cm^{-2}}$)	This model (V)	Reference (V)	Difference %
1022	0.0467	0.0435	+7.356
1988	0.0885	0.0854	+3.618
2983	0.1276	0.1246	+2.327
4005	0.1632	0.1592	+2.513
5027	0.1944	0.1911	+1.727
6022	0.2215	0.2175	+1.839
7016	0.2455	0.2430	+1.029
7955	0.2660	0.2649	+0.415
9033	0.2873	0.2858	+0.525
10000	0.3046	0.3022	+0.794

3.5. Activation overpotential

In Chan et al. [56], the activation overpotential is given separately and individually per electrode. This allows for verification using this data. In addition to the verification done with Chan et al. [56], it is ensured that the switching to approximative models instead of solving the full Butler-Volmer equation produces acceptable errors.

As the procedure is the same for both electrodes, this procedure is only done once for the cathode. Given is that the exchange current density $j_0 = 2000\,\mathrm{A\,m^{-2}}$. This model uses a symmetrical exchange coefficient: both forwards and backwards terms are $\alpha = 0.5$, as used in Equation 2.7.

As it can be seen, there is good agreement between the values predicted by this model and the values from the reference model. This covers one specific case for the activation overpotential of the electrode, but as a general tool it is important that this part of the model holds for a larger span of the design space as well.

This can be done by checking whether the values calculated by this model are inherently consistent with the values calculated by the Butler-Volmer equation. Considering that all the activation overpotential model aims to solve the implicit Butler-Volmer equation $j = f(\eta)$ by using a surrogate function $g(j) \approx f^{-}1(j)$, then it must hold that $j = f(g(j))$. With the previous verification on the data of Chan et al. [56], it is proven that at least for some part of the domain the output of the function aligns with the expected data $g(j) = h(j)$, so such a procedure gives more confidence that $g(j)$ is a good function for the activation overpotential for the larger part of the domain as well.

To cover the greater domain, the error between the approximation used in this model versus the full Butler-Volmer equation is quantified for the following degrees of freedom:

1. Current density: samples are taken starting at very low current density ($j/j_0 = 0.05$) all the way up to very high current density ($j/j_0 = 20$).
2. Bias in charge transfer coefficient forwards (i.e. $\alpha_f > \alpha_b$ or the inverse).
3. imbalance in the charge transfer coefficient (i.e. $\alpha_f + \alpha_b$).

The entire span of these three variables was covered by considering all of their combinations: Symmetrical charge transfer coefficient ($\alpha = (0.5, 0.5)$), $\alpha = (0.2, 0.8)$, $\alpha = (0.7, 0.3)$, $\alpha = (0.5, 1.2)$, and $\alpha = (0.9, 0.5)$, for 20 current densities: $j/j_0 =$ 0.005, 0.08, 0.15, 0.2, 0.3, 0.5, 0.8, 1, 2, 3, 4, 5 6, 8, 10, 15, and 20. These cases were implemented as unit test in the codebase, and as such it was found that all of these cases are within an error margin of 1%.

3.6. Ohmic model

The part of the ohmic model responsible for calculating electric paths was verified by constructing several meshes where the shortest path could easily be determined analytically, and comparing the outcomes of this calculation with the results of the model.

1. If the entire mesh is only a straight line, the path to the closest current collector must simply follow said line.
2. When given two connections, which share the same path up to a vertex and then fork, it should correctly take the path to the closest one.
3. Over a cyclic boundary condition, it should still resolve to the closest one.
4. The resistance of the entire path should be equal to sum of all electrode parts in this path.
5. The inverted path (all the electrodes that need to have their electron path pass through this element) should be consistent for all nodes: If the path of A to the current collector passes through B, then the inverted path for B should contain all elements like A.

3.7. Electrical Conductivity

Geisler [94] presents an Arrhenius fit correlation for the experimentally determined electrical conductivity of Ni-8YSZ in Kornely [95]. This is given in Equation 3.1.

$$\sigma^{eff}_{\text{Ni-8YSZ}} = 82643 \exp\left(\frac{5.349 \times 10^3}{RT}\right) \tag{3.1}$$

This data can be used to compare the method used to estimate the electrical conductivity from purely the metallic phase to an effective electrical conductivity as experimentally determined. The electrical conductivity of pure nickel to be as given in Table 3.8. The porosity of the material is estimated based on the manufacturing process described in Kornely [95], and cross-referenced with literature for typical porosities being $0.1 < \varepsilon < 0.18$ [9], [47]. Evaluations between $800\,\mathrm{K}$ to $1200\,\mathrm{K}$ agreed within 15%, as shown in Table 3.7 for a porosity of 0.12.

Table 3.7: Electrical conductivity of Ni-8YSZ as a function of temperature as expected from the Arrhenius fit by Geisler [94] of experimental data of Kornely [95] versus the values reported by this model

Temp. (K)	This model $(\mathrm{S\,cm^{-1}})$	Reference $(\mathrm{S\,cm^{-1}})$	Difference %
800	1610	1847	-12.83
1000	1468	1573	-6.675
1200	1326	1413	-6.157

3.8. Fluid properties

For each individual mixture species, it is ensured that the conversion of moles to kilogram and vice versa is done correctly. Then, for the fluid mixtures consisting of multiple species, it is ensured that:

1. Setting the mass flow rate or mole rate for the combined fluid must also correctly balance out the mole rates, keeping the mole fractions consistent.
2. Several properties must be the mass-rate averaged enthalpy of its constituents: enthalpy, average molar mass, and thermal conductivity.
3. Partial quantities: partial pressure, activity, mole fraction, properly represent their individual states. This is done by creating unary- and binary fluids for which these states are known, and comparing the resulting resulting states.
4. Summed quantities (mass rate, mole rate) are actually summed properly. This is done by comparing the values to those for air as given in [96].
5. The fluid mixtures for pure hydrogen, pure water, a 10% hydrogen and water mixture, and air (21% oxygen, 79% nitrogen) are compared to the values calculated by Coolprop for temperatures of $800\,^{\circ}\mathrm{C}$

The fluid solver itself is also verified in detail. To ensure it works as intended, it is tested for the following:

1. If there is zero production of mass, the incoming fluid should be exactly equal to the leaving fluid.
2. If an additional flow of water at a higher temperature than the main flow enters, the temperature of the resulting fluid must be higher, and the mass should be equal to the sum of the two inflows.
3. If an additional flow of water at a higher temperature than the main flow enters, the, and there is a secondary outflow, the temperature must still increase to the same value as in the previous case, but the resulting mass flow for the primary outflow should be reduced.

A case representative for the air channel at inlet conditions is considered as well: One upstream air flow, with many oxygen secondary flows leaving. The outgoing flow does not heat up if the temperature of the incoming flow is the same as that of the PENs. It does heat up if the PENs are higher in temperature. If there is a reaction, the mass should have decreased, as oxygen is extracted from the flow.

The same is done, but now for a case representative of fuel at the inlet condition, but with one difference: Hydrogen leaves, but water enters. Since water is heaver, the mass flow should increase. In addition, this means that there is a second flux term that affects the temperature.

3.9. Thermal

For the convection at the wall of the PEN, it is validated that the model correctly switches between equations based on the Reynolds number of the flow. First is the heat transfer for a flow of air, hydrogen and water in at $20\,\mathrm{m\,s^{-1}}$. The values obtained from the model are compared to the values obtained to those in Greitzer [96], Reynolds and Colonna [78] and Poling et al. [61].

Then it is also tested that the sign of the heat transfer is in the right direction for a PEN element in a colder flow (towards the fluid).

The interaction between PEN and CC elements themselves is also verified. Since they share the same fundamental code, this is only tested once, but holds for both the element types.

1. An isolated element should solve to exactly the same temperature that it was at first, and there should be no heat flows going out.
2. If the fluids on both sides are colder and there is no source term, then the element should cool down. Conversely, if they are hotter, then the element should heat up.
3. If there is no source term and the neighbours are warmer, then the resulting temperature should be somewhere between its starting temperature and the neighbouring elements' temperatures.

For a PEN, there is additional functionality that must be ensured works as expected:

1. The thermal conductivity must be a weighted average of its components. It cannot be higher or lower.
2. The heating terms due to oxygen and hydrogen entering into the PEN from the bulk fluid should be positive.
3. The heating term due to water leaving the PEN back int the bulk fluid should be negative.
4. If a reaction takes place, the extra heating source term must be proportional to the current density.

3.10. Convection

The convection implementation was verified with known cases for air with channel flows of $10\,\mathrm{mm}$ for speeds of 0.1, 2, 20, 60, and 40 $\mathrm{m\,s^{-1}}$ at a pressure of $5\,\mathrm{bar}$ $40\,\mathrm{m\,s^{-1}}$ at $1\,\mathrm{bar}$ based on Greitzer [96] and Mills and Coimbra [79]. The same was done for hydrogen. It was also verified that the sign was as expected.

3.11. System-level Validation

The validation for the system level, including thermal and fluid model is based on the results reported in Su et al. [32].

This paper compares the performance of an anode-supported structure to that of a cathode-supported counterpart of otherwise identical geometry. The fuel cell considered has a rib-supported corrugated geometry. This analysis is carried out by performing a multiphysics CFD-like simulation implemented in COMSOL.

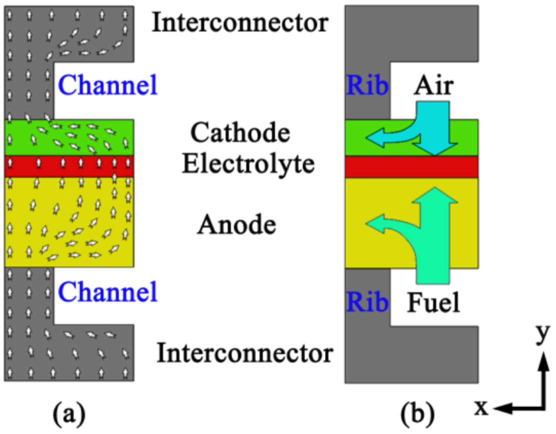

Figure 3.1: The mesh used in Su et al. [32].

3.11.1. Material and Operation Point Matching

To be able to compare the results of the model to the validation case, the configuration of the two cases must be matched as closely as possible.

The following properties are given for the anode material (Ni-YSZ):

As becomes apparent, the provided data is not directly enough to perfectly reproduce the case. For one, the paper does not explicitly state the name of the material of the anode and cathode. Based on the thermal conductivities, and the paper that is sourced for this value, the rough denominations of the materials could be determined as Ni-YSZ for the anode, LSM for the cathode, and YSZ for the electrolyte. This was considered acceptable identification, as with the provided data, exact doping degrees are hard to determine with this method.

The exchange current density is given as an equation in the form of 2.55. Here the activation energy is $120 \times 10^3\,\mathrm{J\,mol^{-1}}$, and the exponents for water and hydrogen is 1. The reference condition for the hydrogen partial pressure / activity is that of the bulk inflow. The equation also features a *reference temperature*, but this value is never elaborated upon. Considering that the reference condition for the other terms is that of the bulk inflow, it was originally assumed that this is the value intended to be referenced. In taking this value however, the exchange current densities generated at design conditions were very far off from what is to be expected from this kind of material [97], [98]. As a solution, this reference temperature was tuned to match the current densities found in Ueguchi et al. [98] and Fukumoto et al. [97] more closely. A value of $1280\,\mathrm{K}$ was set.

The electrical conductivity for the electrode is modeled in the form of 2.33, which relies on the probability of the particle to belong to a percolated cluster of current-carrying particles (p_{el}). This value is not provided in Su et al. [32]. This number varies significantly based on the material used. Based on the material being Ni-YSZ, a value of 0.52 was used [74].

The properties for the cathode material (LSM) are summarised in Table 3.9.

The cathode suffers from the same issues described above as the anode. The exchange current density is now in the form of 2.56 with an activation energy of $130 \times 10^3\,\mathrm{J\,mol^{-1}}$, and an exponent of 0.25. The same reference temperature is assumed as for the anode. A p_{el} of 0.48 is assumed [74]

Almost no information is given on the current collector/interconnect: The only value given is the thermal conductivity of $2\,\mathrm{W\,m^{-1}\,K^{-1}}$. Cross-referencing this value with Ong et al. [99], this is assumed to be a LaCrO3-like material. For such a material, an electric conductivity of $26\,\mathrm{S\,cm^{-1}}$ can be expected [99].

The dimensions of the individual volumes of components used in Su et al. [32] are given in Table 3.11. GOOSE works on a basis of *lines* however, so these volumes had to be represented as lines. The lines were instantiated in such a way that they would coincide with the centre lines of the volumes in the same way as done in Figure 4.2.

Table 3.8: The material parameters used in Su et al. [32] for the anode.

Variable	Symbol	Value
Pore diameter [1]	d_p	$1 \times 10^{-6}\,\mathrm{m}$
Tortuosity [1]	τ_p	3.5
porosity [1]	ε_p	0.3
Anodic charge transfer coefficient	α_a	1
Cathodic charge transfer coefficient	α_c	0.5
Electrical conductivity [2]	σ_e	$3.27 \times 10^6 - 1065.3T$
Thermal conductivity [3]	κ	$2\,\mathrm{W\,m^{-1}\,K^{-1}}$
Contact resistivity with current collector [4] [5]	r_{ASR}	$0.03\,\Omega\,\mathrm{cm}^2$

[1] A single value is given, and hence assumed to hold for both anode and cathode.

[2] The electrical conductivity given is for Nickel, implying that they assume all current is carried exclusively by the metallic phase.

[3] The dimension given in the source is incorrect, but verifying with the source Petruzzi et al. [89] shows that the value is correct.

[4] This is erroneously referred to as the *Area specific contact resistance*, but from their use in equation 23 it becomes clear they do in fact use it as a contact resistivity. To add to the confusion, at some points in the text the unit is mistyped as $\Omega\,\mathrm{cm}^{-2}$.

[5] It is not clear from their methodology and documentation whether this value is only taken once, accounting for both electrodes, or if this works per electrode. Here it is assumed this amount is per electrode.

The fuel inflow is given with an inflow speed of $0.3\,\mathrm{m\,s^{-1}}$ at $1\,\mathrm{bar}$ and $973.14\,\mathrm{K}$. The composition is given in terms of molar volume fractions (molality): Water with $0.375\,\mathrm{mol\,m^{-3}}$ and hydrogen with $12.147\,\mathrm{mol\,m^{-3}}$. This is converted to mole fractions by taking ratios, as done in Equation 3.2. The total mole rate is determined from the total molar density as given in Equation 3.3 where C is the molar volume fraction. The cross sectional area of the fluid channel $A_{channel}$ is constrained by the PEN and rib, amounts to $1.5\,\mathrm{mm}^2$.

$$Y = \frac{C}{\sum C_i} \tag{3.2}$$

$$\dot{N} = u_{in} A_{channel} \sum C_i \tag{3.3}$$

C_i	Molar volume fraction of species i in a mixture
u_{in}	Inflow speed of a fluid
$A_{channel}$	Cross-sectional area of a fluid channel

The air is treated the same way, but now with a composition of $9.893\,\mathrm{mol\,m^{-3}}$ nitrogen and $2.63\,\mathrm{mol\,m^{-3}}$ oxygen.

The last value that must be known is the operating voltage of $0.7\,\mathrm{V}$.

For the diffusion coefficient model, the *Chapman-Enskog* model was used. For the Knudsen model, the *Asaeda* model was used. The convergence criteria of all sub-solvers (electrochemical, thermal, fluid- and activation overpotential distribution, and the slice-level solver) were set to relative error of 10^{-7}.

3.11.2. Results

Su et al. [32] gives most of their data as three-dimensional colour plots, which introduces an error in interpretation. They have been digitised to the author's best ability. The uncertainty of the external data presented in Figure 3.2, and Figure 3.3 is added using error bars to indicate uncertainty in reading them off.

Table 3.9: The material parameters used in Su et al. [32] for the cathode.

Variable	Symbol	Value
Avg. pore diameter [1]	d_{pore}	$1 \times 10^{-6}\,\mathrm{m}$
Tortuosity [1]	τ_p	3.5
porosity [1]	ε_p	0.3
Anodic charge transfer coefficient	α_a	0.75
Cathodic charge transfer coefficient	α_c	0.5
Electrical conductivity	σ_e	$\frac{4.2\times10^7}{T}\exp\left(\frac{-1150}{T}\right)$
Thermal conductivity [3]	κ	$4\,\mathrm{W\,m^{-1}\,K^{-1}}$
Contact resistivity with current collector [4] [5]	r_{ASR}	$0.03\,\Omega\,\mathrm{cm}^2$

[1] A single value is given, and hence assumed to hold for both anode and cathode.

[3] The dimension given in the source is incorrect, but verifying with the source Petruzzi et al. [89] shows that the value is correct.

[4] This is erroneously referred to as the *Area specific contact resistance*, but from their use in equation 23 it becomes clear they do in fact use it as a contact resistivity. To add to the confusion, at some points in the text the unit is mistyped as $\Omega\,\mathrm{cm}^{-2}$.

[5] It is not clear from their methodology and documentation whether this value is only taken once, accounting for both electrodes, or if this works per electrode. Here it is assumed this amount is per electrode.

Table 3.10: Electrolyte material properties used in the validation case against Su et al. [32]

Variable	Symbol	Value
Ionic conductivity	σ_i	$6.25\times10^4\exp\left(-\frac{10300}{T}\right)$
Thermal conductivity [3]	κ	$6\,\mathrm{W\,m^{-1}\,K^{-1}}$

[3] The dimension given in the source is incorrect, but verifying with the source Petruzzi et al. [89] shows that the value is correct.

Table 3.11: Repeating stack dimensions in Su et al. [32]

Dimension	Size
Channel length	$20\,\mathrm{mm}$
Channel width	$1.5\,\mathrm{mm}$
Interconnect height	$2\,\mathrm{mm}$
Rib width	$1.5\,\mathrm{mm}$
Rib height	$1\,\mathrm{mm}$

Figure 3.2 shows a comparison of the temperature trend along the flow path. It is split up into two graphs for legibility. Figure 3.2a focuses on the temperatures of the air and fuel, and Figure 3.2b focuses on the solid elements (the PEN and current collectors).

Figure 3.3 shows the hydrogen fraction of the bulk flow along the flow path.

The main point of research in Su et al. [32] is a comparison of anode-supported cells and cathode-supported cells, as well as the effect of rib spacing. This can be replicated using this model as well.

Figure 3.4 shows that there is clear agreement between both models. There is a roughly constant offset, but the slopes of both curves is similar, indicating that the effect of the change in rib spacing is accurately represented in the model.

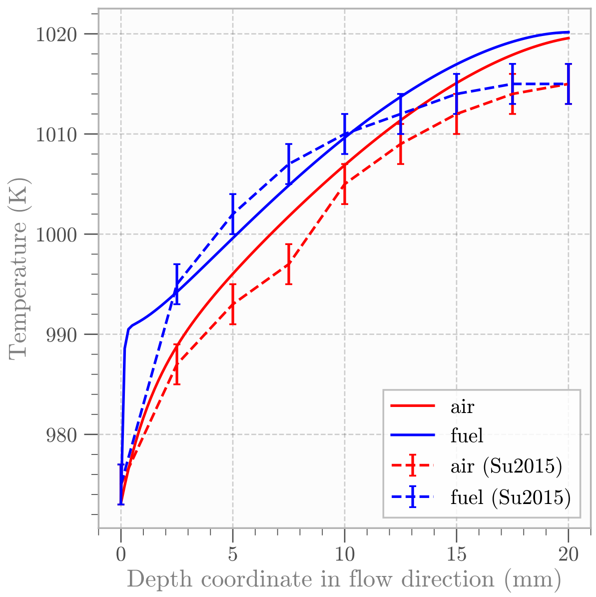

(a) Fluid temperatures (air and fuel) as determined by this model, compared to those obtained from Su et al. [32]. Displayed error bars are standard deviation in reading off colour plots.

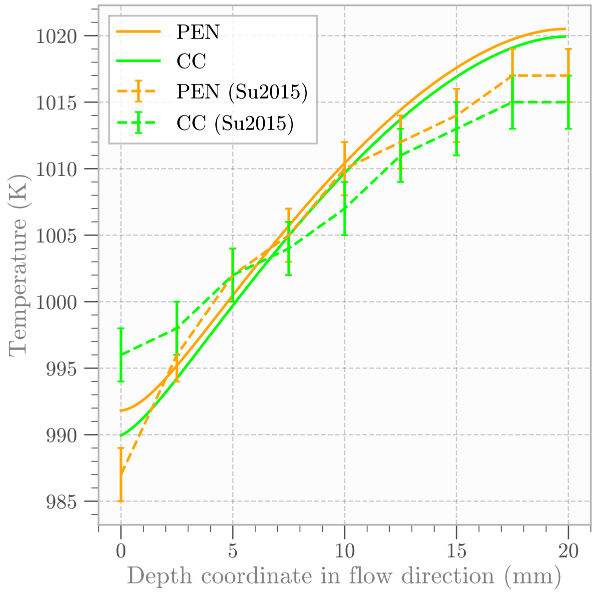

(b) Temperatures of solids (PEN and CC)

Figure 3.2: Comparison of the temperature trend along the flow path calculated by the model in this work as compared to that in Su et al. [32]. Displayed error bars are standard deviation in reading off colour plots.

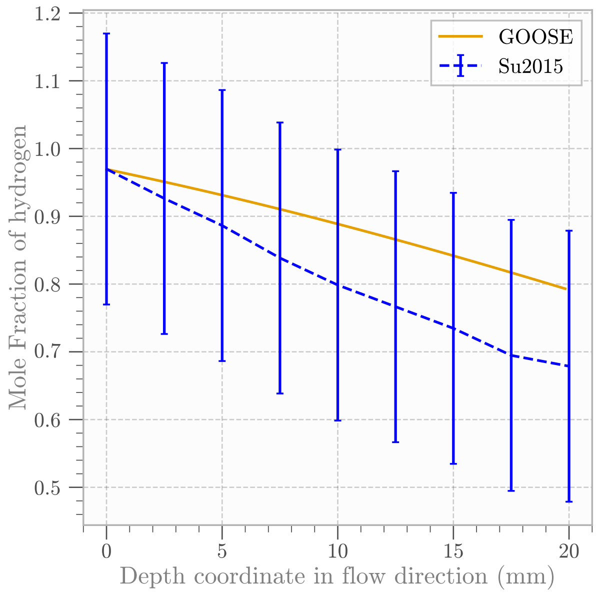

Figure 3.3: Comparison of the hydrogen fraction of the bulk flow along the flow path as calculated by this model, and as reported in Su et al. [32]. Displayed error bars are standard deviation in reading off colour plots.

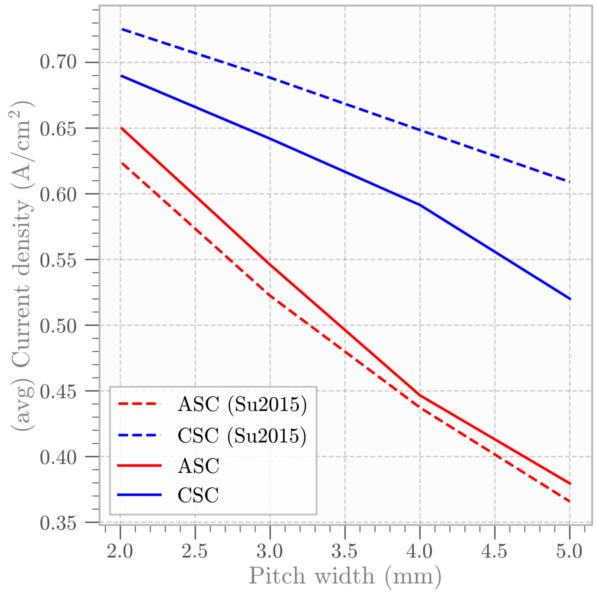

Figure 3.4: Comparison of the average current density as a function of changing rib spacing, as determined by this model and as reported in Su et al. [32]. Displayed error bars are standard deviation in reading off colour plots.

Because all the physical phenomena modeled are very strongly coupled, any difference in result compounds quickly. A small difference in result in one domain directly affects the result in another, which then again affects the first. With this in mind, overall agreement with the validation data is good, with overall relative errors being within 6%. With this, it is safe to conclude that the model is validated.

Looking into the origins of the difference in the results can still lead to insight however- Overall, the cause for difference in the obtained results can most likely be attributed to a difference in modelling strategy.

The energy balance solved in Su et al. [32] does not consider the extra mass flow leaving- and entering the anode and cathode. As such, it misses an enthalpy flux. The temperature of these flows are that of the bulk flows and closer to the PEN respectively, causing a net enthalpy flux. The net effect of this flow is cooling in the simulated case. As a result, GOOSE considers one extra method of dissipating heat into the bulk flow, which will cause the bulk fluids to heat up faster, and PENs to have a more flat temperature profile.

Another difference in how heat transfer between the solid elements and the bulk flow exists in the convection. The method described in Su et al. [32] uses Newton's law of cooling, but does not state any relations for the heat transfer coefficient h. Reverse-engineering the approach taken in this paper in the software suite that was used, Comsol [100], it was found that a relatively general method for determination of the heat transfer coefficient was used. This model is intended for use in relatively high Reynolds numbers, and might not be valid in the flow regime considered [1].

The yielded values are in the range of $h = 10$, which is very different from the values obtained with the dynamic approach taken in this model.

The difference in modelling methodology can be another cause for the difference in outcomes. The model presented in this work operates in a fundamentally different way, taking a hybrid approach somewhere between what a CFD model would, and a reduced order model. The reference paper is however fully a CFD multiphysics model, where all processes are resolved on a per-volume basis. If the mesh is fine enough, this means that some processes that are simplified in this model, such as diffusion, should be better resolved than they are in the validation CFD case. Conversely, if the mesh is not fine enough, this could also mean that some processes are not resolved with the same accuracy in the validation case, as gradients and profiles can only be represented to a scale as small as the element size (and no sub-grid scale modelling is done).

The mesh used in Su et al. [32] is comprised of only 6540 elements. With how their simulation is set-up, these cells are shared between fluids, anode, cathode, electrolyte, and current collector. Unlike in this model, where the entire PEN can be accounted for with a single element, in a CFD-based approach many elements are needed orthogonal to the flow path to accurately resolve species diffusion into the porous media. The only way this can be done is by severely limiting the resolution in the flow wise direction.

In setting up this validation case, the meshing was set up in such a way that it would resemble the mesh used in the validation case, to eliminate one set of variables. However, at meshes as coarse as the one proposed in Su et al. [32], the total amount of iterations needed to reach convergence were much higher ($\approx$12000) compared to those with a higher resolution ($\approx$6000). For this reason, the validation was done on a mesh that was already a much higher resolution than the one used in this paper.

To quantify this error, a mesh convergence study was carried out. Following the results of subsection 3.11.3, the mesh could have beer made even finer to get more accurate results.

This analysis is carried out and can be found in in the appendix. The comparison at a mesh with N times more elements is shown in Appendix C. The results of this study show that on an even finer mesh the gradients in temperature become even less pronounced than in Figure 3.2. This implies that the mesh used in Su et al. [32] was most likely not fully resolved, and the more pronounced temperature gradients can be a

---

[1] More details can be found in the COMSOL documentation at `https://doc.comsol.com/5.5/doc/com.comsol.help.heat/heat_ug_theory.07.76.html`

direct result of this.

3.11.3. Mesh Convergence Study

To demonstrate the internal consistency of the model, as well as its convergence behaviour, a mesh convergence study was performed. The method used is based on Slater [101]. The model is first run at a high resolution with a grid spacing h_{ref}, as a reference case. h_{ref} was set so that the resolution in the depth axis of the flow direction (z) was 600, the PEN resolution was 300, and CC resolution as 40. The model is then run at increasingly lower resolutions, with a new normalised grid spacing N,as given by Equation 3.4. This was done for $N = 2, N = 4, N = 8$. The relative error is then determined using Equation 3.5. Since the model aims to resolve multiple physical phenomena, the relative error is determined for two separate representative values: the average PEN temperature, and the average generated current density. The trend of these relative errors are plotted against normalised grid spacing on a log-log scale in Figure 3.5. This is done for both the current density in Figure 3.5a and for temperature in Figure 3.5b.

As it can be seen, the error decreases more than linearly for an increase in resolution. This is desirable for a solver, as it shows internal consistency as well as telling something about the expected computational time required for higher resolution meshes. It also shows the convergence of the discretisation error towards 0 on a hypothetical, infinitely fine, mesh.

$$N = \frac{h}{h_{ref}} \tag{3.4}$$

$$\varepsilon = \frac{f - f_{ref}}{f_{ref}} \tag{3.5}$$

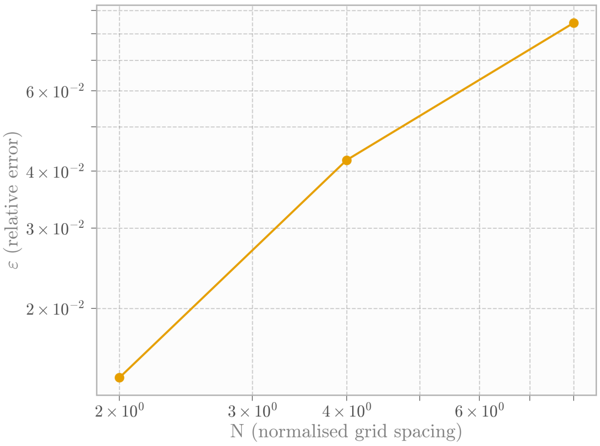

(a) Current density

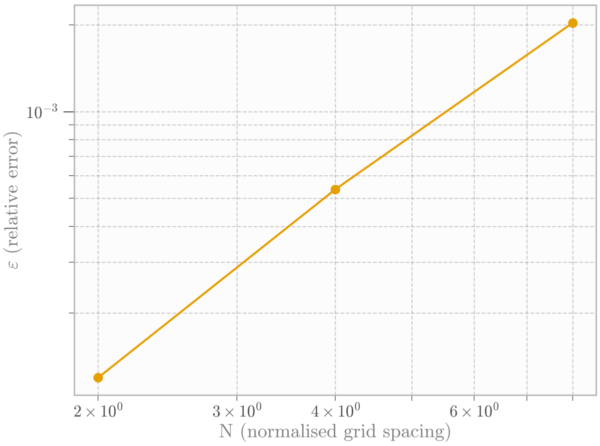

(b) Temperature

Figure 3.5: Mesh convergence for normalised grip spacing N. The relative errors to a very high-resolution mesh are given for two characteristic variables: temperature and current density.

4

Parametric Study

Research into optimisation of fuel cell stacks as a whole is scarce, and the body of literature focusing on geometrical studies is even smaller [102]. The model described in this work was built to focus on this gap, with exploration of the greater design space in mind. A parameter study is carried out for several geometries, comparing objective values for key performance characteristics. For application in aviation, there are three such performance criteria that are of special interest:

1. Volumetric power density, as engines are very constrained in size.
2. Stack temperature and its gradients, as this is an indicator for life expectancy and degradation.
3. Fuel utilisation, as it gives an indication of how efficiently the fuel cell operates in extracting energy out of the fuel.

SOFCs come in many shapes and sizes. In finding what is the '*optimal*' design for this application, the depth one can go into is enormous. However, the focus of this parameter study is not to give full coverage, but mainly to give a first taste, and show what is possible with modelling using this framework. Thusly, three archetypical geometries are chosen representative of their entire family of geometries to be compared:

A baseline will be set with a ribbed planar geometry. This is very similar to the case described in section 3.11. Representative for a monolithic geometry, a corrugated design is chosen. Finally, a tubular geometry will be considered. A variation on the tubular geometry with non-standard stacking will also be considered.

In these geometries, defining dimensions are parametrised. All cases will be simulated for a reference geometry, and then altered to identify the effect of change in cross-section geometry. This is done at points of 80%, 90%, 110% and 120% of their reference condition (e.g. if the reference length of a parameter a is $1\,\mathrm{mm}$, then it will be evaluated at $0.8\,\mathrm{mm}$, $0.9\,\mathrm{mm}$, $1.1\,\mathrm{mm}$, and $1.2\,\mathrm{mm}$ respectively). To isolate the effects of geometry alone, the materials will be shared among all three and not varied.

The depth of all meshes is the same at $2\,\mathrm{cm}$, comprising the area of the fuel cell stack where performance varies the most. All meshes are simulated at a similar resolution. A contact resistance between electrodes and current collector of $0.01\,\Omega\,\mathrm{cm}^2$ is assumed.

4.0.1. Humidity of Fuel

In addition to the geometries, one operating condition will be altered as well: the humidity of the fuel mixture. As the operating temperature of a fuel cell is very high, the hydrogen fuel needs to be pre-heated before entering the fuel cell to avoid thermal shock [103]. To be able to heat up the hydrogen in-situ in application of an aero-engine, the fuel is often mixed with hot water as this allows it to take up more heat in a heat exchanger, or alternatively the hydrogen itself is mixed in with partially combusted hydrogen with a much higher temperature. The presence of water in the fuel mixture is one that is not yet widely studied, but might have a great impact on local and overall performance of the fuel cell stack.

4.0.2. Ribbed Planar

The ribbed planar geometry is a de-facto standard in SOFC stack geometries, as it is easy to manufacture and easy to modularise [104]. A schematic overview of its geometry is depicted in Figure 4.1, with the parametrisation as given in Table 4.1.

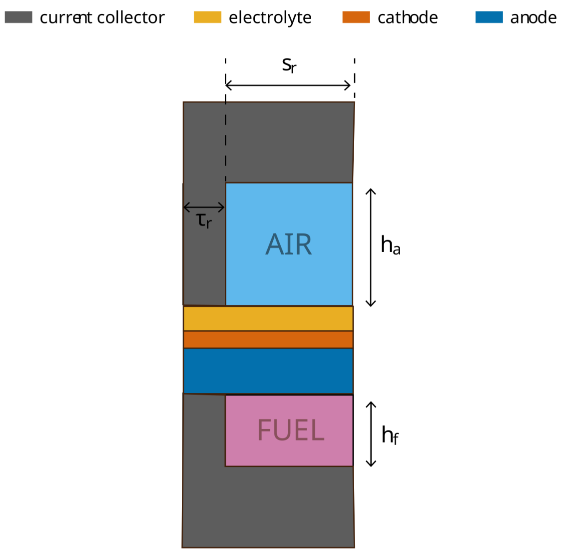

Figure 4.1: A schematic diagram of a planar cross-sectional geometry outfitted with ribs to connect to the current collectors. Also Indicated are the characteristic lengths used in its parametrisation.

Table 4.1: Parametrisation of the ribbed planar geometry, with reference values.

Parameter	reference value
h_a	$1.5\,\mathrm{mm}$
h_f	$1.5\,\mathrm{mm}$
s_r	$2.5\,\mathrm{mm}$
τ_r	$1.0\,\mathrm{mm}$
χ	0.9

h_a	Parametrised length of the air channel for a ribbed planar geometry
h_f	Parametrised length of the fuel channel for a ribbed planar geometry
s_r	Parametrised rib spacing for a ribbed planar geometry
τ_x	Thickness of the component x
χ	Parametrised humidity (vapour fraction) of fuel mixture. A value of 0.0 represents a fluid consisting purely of water, whereas a value of 1.0 represents a fluid consisting purely of hydrogen

This geometry can be altered in several ways: as air and fuel are not consumed one-to-one and their fluid mixture properties differ, their respective channel heights h_a and h_f can be altered to influence fluid mixing, heat transfer, and change overall size of the stack. The rib spacing s_r was already briefly touched upon in section 3.11, but its effect on temperature as well as its effect in overall power generation has not yet been explored. Placing the ribs further apart means that the dead PEN area is reduced, but the electron path now spans both the cathode and anode for longer.

It might be wise to use a different rib spacing on both the anode and cathode side, as the lower electrical conductivity of the cathode means that the impact on ohmic losses will be higher on this side. Staggering the ribs might also have an effect on this behaviour. However, both of these alterations would mean that the dead spots on the cathode and anode side are in different locations, meaning that the mesh would have to be more complicated. For the sake of brevity, this possible parametrisation is therefore not considered in this study, and only a non-staggered distribution is considered.

The mesh shown in Figure 4.1 is constructed in GOOSE as shown in Figure 4.2. The connections between nodes 1-2, 1-4, and 4-7 are current collectors. For simplicity, it is assumed that they are all the same thickness. The edges between 3-5 describe the dead zone where the rib covers both the anode and the cathode. The horizontal distance between 3 and 5 is then equal to the thickness of the rib. This leaves the edge between nodes 5 and 6 as the active PEN.

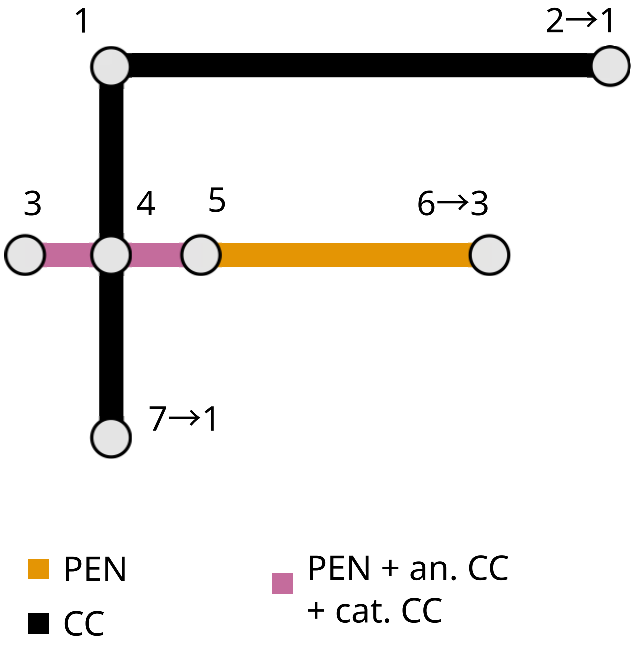

Figure 4.2: The mesh for the ribbed planar mesh as interpreted as a set of nodes to represent the geometry in GOOSE.

4.0.3. Corrugated Monolithic

Representative for a monolithic geometry, a corrugated design is used. It is one of the monolithic fuel cell stack designs that is relatively well-researched [5], [105]. Because of its similarity with planar fuel cells, it is easier to manufacture, and can be manufactured with many existing manufacturing processes [6], [16].

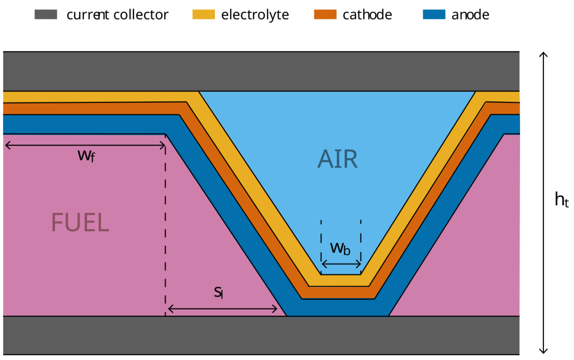

Figure 4.3: A schematic diagram of a corrugated-style monolithic cell cross-sectional geometry. Indicated are the characteristic lengths used in its parametrisation.

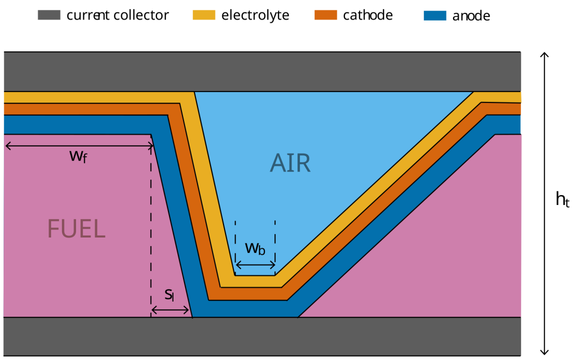

Figure 4.4: A schematic diagram of a corrugated-style monolithic cell cross-sectional geometry where the slant is larger than in Figure 4.3.

Table 4.2: Parametrisation of the corrugated monolithic geometry, with reference values

Parameter	reference value
w_f	$0.8\,\mathrm{mm}$
w_a	$0.8\,\mathrm{mm}$
h_t	$2.1\,\mathrm{mm}$
s_l	$2.1\,\mathrm{mm}$
χ	0.9

w_f	Parametrised flat straight section of the fuel channel for a corrugated monolithic geometry
w_a	Parametrised flat straight section of the air channel for a corrugated monolithic geometry
h_t	Parametrised total channel height for a corrugated monolithic geometry
s_l	Parametrised slant for corrugated monolithic geometry

Its cross-sectional geometry can be parametrised to four parameters:

1. The straight overlapping length between the cathode and the current collector, denoted by w_a.
2. The straight overlapping length between the anode and the current collector, denoted by w_f.
3. The slant, determining the difference in slopes for the two angled PEN sections. This is parametrised as a horizontal offset, denoted with s_l. The effect of changing this parameter becomes clear when comparing

Figure 4.3 to Figure 4.4.

4. The overall height of the two combined channels. This is set as h.

The reference conditions for a corrugated monolithic cell chosen are given in Table 4.2. As this is an exploratory study, the mesh is kept relatively simple:

The stacking is modelled by repeating the units as-is in the vertical and horizontal direction. This way, the parameters can all be modified individually and no coupling occurs. The total width w of the repeating section is kept constant, so only the distribution inside this limited volume is changed. Scaling the entire assembly in the vertical axis is already accounted for by altering h_t.

This mesh is constructed in GOOSE as shown in Figure 4.5. The edges between nodes 2-5 are set as current collectors. The edge between nodes 1-2 is set as a PEN+CC without air to represent the inability for air to into the PEN. The edge between nodes 6-7 is set as a PEN+CC without fuel to represent the inability for fuel to enter the anode. The edges 2-6 and 5-7 are PEN sections. Nodes 3 and 4 are separated so that stacking as described earlier in this section can be performed. They are set to coincide with nodes 3 and 4 respectively. The cyclic boundary condition in the horizontal direction by setting nodes 5 and 1 to coincide as well.

4.0.4. Tubular

Tubular SOFCs are an interesting alternative to corrugated and planar stacks, as they forego the need to use sealing materials needed to stop fuel and air mixing. There is no free lunch, as they incur larger ohmic losses as the electron path covers a large section of both the anode and the cathode [106].

Table 4.3: Parametrisation of the tubular geometry, with reference values

Parameter	reference value
τ_r	$0.6\,\mathrm{mm}$
r_t	$1.8\,\mathrm{mm}$
s_t	$2.6\,\mathrm{mm}$

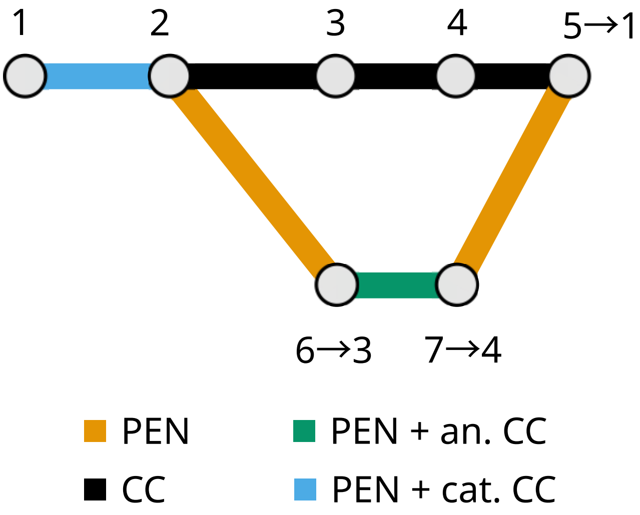

Figure 4.5: The corrugated mesh as seen in Figure 4.3 as interpreted as a set of nodes to represent the geometry in GOOSE.

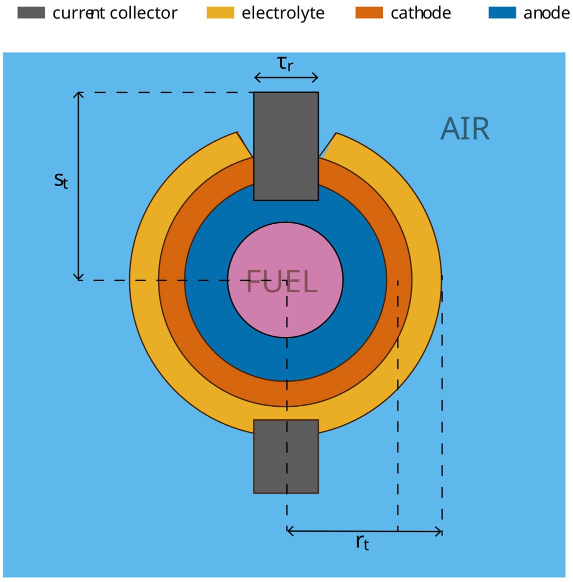

Figure 4.6: A schematic diagram of tubular cross-sectional geometry. Indicated are the characteristic lengths used in its parametrisation.

τ_x	Thickness of the component x
r_t	Parametrised mean radius of a tubular fuel cell
s_t	Parametrised spacing between two tubes in a tubular SOFC array

Its cross-sectional geometry can be parametrised with three parameters:

1. The overall radius of the tube. For clarity,

the outer diameter is chosen as r_t. On a line-based mesh, this would have to describe the center line: $r_t - \frac{1}{2}(\tau_{an} + \tau_{cat} + \tau_{elt})$.

2. The distance between two tubes can be correlated to the length of the current collector, s_t. This works analogous for the tube stacking density.
3. With the circular shape, the effect of shadowing is much larger. The rib thickness τ_r on the dead zones is therefore varied, just like in the ribbed planar case.

The fuel channel of a tubular fuel cell is simply circular, but the air channel has a much more complex profile. Using a single value for a hydraulic diameter for such a channel is reductionary, so instead the hydraulic diameter is varied between the regions where it is very close to another cathode wall, and where it has a larger void above it. For a hexagonal patterning, the channel height is lowest at radial coordinates $\frac{\pi}{3}\,\mathrm{rad}$, $\frac{2\pi}{3}\,\mathrm{rad}$, $\frac{4\pi}{3}\,\mathrm{rad}$, and $\frac{5\pi}{3}\,\mathrm{rad}$. Here the hydraulic diameter was taken to be one third of the nominal hydraulic diameter of a nested tube. At the points with the largest volume of air available, two thirds is used instead. In between, the values are linearly varied

This mesh is constructed in GOOSE as shown in Figure 4.7. The edge between nodes 1-2 is are set as current collectors to the anode and the cathode respectively. The edges between nodes 2-3 and 7-2 represent the inactive area without cathode covering. It is modeled as a PEN section that does not have an *air* target set. This means that it does not allow any reaction to occur. The edges between nodes 4 and 6 are the same, but now for the anode instead. A point of improvement for these two zones would be to actually allow a different mesh type without the cathode: right now, the cathode is merely set as inactive, but it still functions as a vessel for heat transport, and still has an effective conductive area. The connections between nodes 3 and 4, and 6 and 7 are subdivided into many more sections so that a circle is approximated as a regular n-gon, each segment set as PEN sections. There is no tooling in place yet to describe curved surfaces, so this is approximated by sectioning it as a regular n-gon.

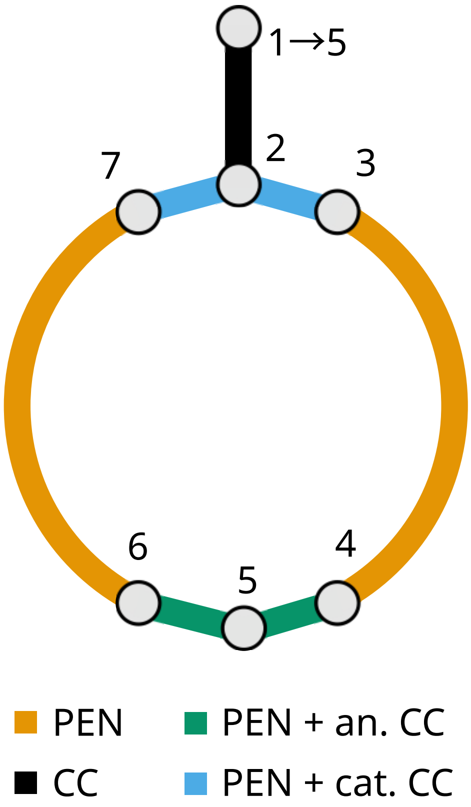

Figure 4.7: The mesh of the tubular cross-sectional geometry as depicted in Figure 4.7 interpreted as a set of nodes to represent the geometry in GOOSE.

4.1. Material Selection

It has already been established that there is a wide variety in materials used in SOFCs. However, the goal of this study is not to look for materials, but to look for the effect of geometry. Materials for this geometry study have therefore been chosen because they are relatively simple, and broadly established in literature. By choosing more well-researched materials, the introduced uncertainty due to materials is reduced– Something that will become apparent is a significant issue. A study like this can be repeated with more specific materials when material data and information becomes more widespread, or when specific materials are of interest.

Table 4.6 contains general information on the chosen material parameters. The sections following elaborate on the reasoning behind choosing these values in more detail. A symmetrical charge transfer coefficient is used. This means that all four forward/backward anode/cathode values are 0.5. Similarly, porous properties are assumed mostly the same, except that the anode material's porosity is changed to 34% so that an existing known source for thermal conductivity can be used.

4.1.1. Cathode

For the cathode, pure LSM is chosen. This material was chosen because it is one of the most widely used and best understood cathode materials, and therefore had the best coverage in terms of material data. Cathode materials suffer the greatest of the gaps in literature, with very little material information being reported on. It must be noted though, that pure LSM is known to have comparatively poor low-temperature performance. To improve its ionic conductivity, thereby extending its effective ETBP and raising exchange current density, LSM is usually co-doped with other materials [107]. Unfortunately, such co-doped materials are not covered reliably in literature, and therefore deliberately avoided to not give a skewed perspective of performance that can be expected. To compensate for this lower conductivity, the operating temperature is therefore set to a somewhat elevated value of $1000\,\mathrm{K}$. This has implications for the applicability of this study to the operating regime of an aircraft engine integrated SOFC. It should still give a good indication of the trends to expect however, as the results of different meshes all at the same inflow temperatures and materials will be compared with each other and normalised.

Its exchange current density can be parametrised with regards to species presence and temperature as given in Equation 4.1 [97].

$$j_{0_{\mathrm{LSM}}} = 7.5 \times 10^{7} \exp\left(-\frac{187}{RT}\right)\left(\frac{p_{\,\mathrm{O}_2}}{p_{\,\mathrm{O}_2\,ref}}\right)^{0.33} \tag{4.1}$$

The behaviour of electrical conductivity of LSM is not quite so clear-cut, unfortunately. There is a very large variation in the value reported by literature. The relation used in the validation case leads to values in the order of $13\,000\,\mathrm{S\,cm^{-1}}$ for a temperature of $1000\,\mathrm{K}$. Other literature reports on measurements of an electrical conductivity of $235\,\mathrm{S\,cm^{-1}}$ at this same temperature [108]. One would be inclined to attribute this difference to other unknown material parameters: Tortuosity, interaction with fluids, pore diameter– Even if these numbers are kept near-constant, values of a significant order of magnitude are still reported: $3.5\,\mathrm{S\,cm^{-1}}$ [109]. Confusingly, all of the above sources state that their values agree with literature. Only Paydar et al. [108], which proposes values of $235\,\mathrm{S\,cm^{-1}}$, provides citations for this claim, referencing another experimental study finding a value of $10\,\mathrm{S\,cm^{-1}}$ at $1000\,\mathrm{K}$ [110]. After weighing these factors, the experimental findings of Paydar et al. [108] were chosen for representing the electrical conductivity of LSM

Table 4.4: Electrical conductivity over various temperatures for LSM determined experimentally in Paydar et al. [108].

Temperature (K)	Electrical conductivity σ ($\mathrm{S\,cm^{-1}}$)
572	177
672	200
772	218
874	223
972	231
1074	241
1174	240

For thermal characteristics, the thermal conductivity κ is reported on at room temperature, but no sources could be found describing it at operating temperatures. At $300\,\mathrm{K}$, $La_{0.83}Sr_{0.17}$ is found to have a thermal conductivity of $2.32\,\mathrm{W\,m^{-1}\,K^{-1}}$[111]. It is implied, but not explicitly stated that this is for a non-porous sample. A porosity-dependent study was also found, stating its value to be between $1.45\,\mathrm{W\,m^{-1}\,K^{-1}}$ and $0.8153\,\mathrm{W\,m^{-1}\,K^{-1}}$ for porosities of $\varepsilon_p = 0.23$ and $\varepsilon_p = 0.39$ respectively [112]. With the desired porosity of $\varepsilon = 0.3$, the two values were linearly interpolated to a constant κ at $1.172\,\mathrm{W\,m^{-1}\,K^{-1}}$ for this porosity.

4.1.2. Anode

a Ni-YSZ cermet was chosen for the anode material. Its electrical conductivity is determined purely by the metallic phase (nickel). An experimentally determined relationship was already validated in section 3.7 by using the metallic phase of nickel. This relationship is reused as-is.

Values found for its exchange current density vary a bit in literature [98], [113], [114], [115]. Marina et al. [114] gives actual experimental results, but these are for low pressures, low temperatures, and very low hydrogen composition- not exactly representative of the conditions aimed for. The equations used in He et al. [115] and Ueguchi et al. [98] yielded values that are rather dissimilar to these experimental findings. The empirical relation used in in Costamagna et al. [84] has a similar order of magnitude, and is therefore used. It is accompanied with a symmetrical charge transfer coefficient.

$$i_{0_{\text{Ni-YSZ}}} = 5.5 \times 10^{8} a_{\mathrm{H_2}}\, a_{\mathrm{H_2O}}^{-0.5} \exp\left(-\frac{100 \times 10^{3}}{RT}\right) \tag{4.2}$$

Thermal conductivity of Ni-YSZ is obtained from Radovic et al. [91].

Table 4.5: Thermal conductivity of Ni-YSZ with a porosity of 34%. Data from Radovic et al. [91].

Temperature K	Thermal conductivity κ $\mathrm{W\,m^{-1}\,K^{-1}}$
687.3	4.72
739.6	4.73
778.9	4.74
812.1	4.75
859.7	4.78
889.4	4.76
925.1	4.75
969.0	4.75
995.2	4.67
1024.9	4.60

4.1.3. Electrolyte

The electrolyte material chosen is YSZ. Ionic conductivities for this material are relatively consistent [47], [116]. An Arrhenius-fit parametrisation based on Shi et al. [116] was used, given in Equation 4.3.

$$\sigma_{ion} = \frac{133117255.5}{T} \exp\left(-\frac{96611.97}{RT}\right) \tag{4.3}$$

The thermal conductivity spans the range of $1.8\,\mathrm{W\,m^{-1}\,K^{-1}}$ to $2.4\,\mathrm{W\,m^{-1}\,K^{-1}}$ in the operating range of SOFCs [86], [117]. It is given here as a function of porosity, but this is only relevant if it is co-doped and used as an electrode. For use as an electrolyte, the base material property can be used directly. It is also very weakly a function of temperature at lower temperatures, but at higher temperatures (> $600\,\mathrm{K}$) it remains very close to constant at a value of $2.04\,\mathrm{W\,m^{-1}\,K}$ for the bulk phase of YSZ with eight mole-percent doping.

4.1.4. Current Collector

The same LaCrO3-adjacent material as used in subsection 3.11.1 is used, with a thermal conductivity of $2\,\mathrm{W\,m^{-1}\,K^{-1}}$, and electric conductivity of $26\,\mathrm{S\,cm^{-1}}$ [99]

4.1.5. Inflow

A 90 mol% flow of hydrogen is used for the inflow, to emulate the humidification of hydrogen to make it easier to heat up as described in subsection 4.0.1. The oxidiser is simply air. Both fluids are compressed to a pressure of $8\,\mathrm{bar}$, and elevated to a temperature of $1000\,\mathrm{K}$.

4.2. Sensitivity of a Ribbed Planar Stack

The results of the parameter study for the ribbed planar stack design are shown in Figure 4.8. The raw data for this analysis is supplied in Table B.11.

All of the other plots show clearly defined trends, most close to being linear, others following stronger exponential or quadratic

Table 4.6: The parameters used in the geometry.

Variable	Symbol	Value
Cathode	LSM	
Avg. pore diameter	d_{pore}	$1 \times 10^{-6}\,\mathrm{m}$
Tortuosity	τ_p	3.5
Porosity	ε_p	0.3
Charge transfer coefficient	α	0.5
Contact resistivity	R_{ASR}	$0.01\,\Omega\,\mathrm{cm}^2$
Exchange current density	j_0	Equation 4.1
Electrical conductivity	σ	Table 4.4
Thermal conductivity	κ	$1.172\,\mathrm{W\,m^{-1}\,K^{-1}}$
Anode	Ni-YSZ	
Avg. pore diameter	d_{pore}	$1 \times 10^{-6}\,\mathrm{m}$
Tortuosity	τ_p	3.5
Porosity	ε_p	0.34
Charge transfer coefficient	α	0.5
Contact resistivity	R_{ASR}	$0.01\,\Omega\,\mathrm{cm}^2$
Exchange current density	j_0	Equation 4.2
Electrical conductivity	σ	Equation 3.1
Thermal conductivity	κ	Table 4.5
Electrolyte	YSZ	
Electrical conductivity	σ_{ion}	Equation 4.3
Thermal conductivity	κ	$2.04\,\mathrm{W\,m^{-1}\,K}$ [117], [118]

curves. The only outlier here is the fuel utilisation of the tubular geometry, which will be covered in more detail in section 4.4.

4.2.1. Fuel Channel Height

Reducing fuel channel height while keeping the fuel flux constant relatively decreases the total amount of fuel supplied, while also increasing the hydraulic diameter of the fuel channel. Intuitively one would expect the temperature to go down because of this. There appears to be only minimal coupling with the reaction rate, as the current density decreases slightly with an increase in fuel channel height, as does the total power generation. Most interestingly, the fuel utilisation goes up significantly as the fuel channel is decreased in height. With the constant flux approach, the air-to-fuel mass rate ratio is skewed further off-balance in doing so.

However, total power yield is dependent of the total size of the unit mesh, which itself changes as the fuel channel height is increased. To see the true effect it has on volumetric power density, it makes more sense to look at the power yield per cross-sectional surface area.

One would expect the geometric design to merely be a trade-off in (volumetric) power density and fuel economy, but the fuel channel height shows that this is not always so simple. At this design point, increasing the fuel channel height decreases the fuel utilisation, but it also decreases the power normalised to the cross-sectional area, and hence the power density. Normalising the change supplied fuel due to the constant flux relative to the actual fuel utilisation, we see that this trend still holds: the amount of fuel supplied is not what actually affects the characteristic performance here. This indicates that it is possible to optimise this design, regardless of performing such a trade-off. Through proper geometry optimisation, it appears you can have your cake, and eat it too.

4.2.2. Air Channel Height

In theory, changing the air channel height would have the same effect on temperature, but the opposite effect on the air-to-fuel ratio. The results indicate however, that the effect on fuel utilisation is actually relatively minor, while the total power (directly coupled to the average current density) goes down quite significantly for an enlarged air channel. With the constant mass flux condition, this causes a relatively similar effect on air-to-fuel ratio as changing the fuel channel height. The difference in magnitude shows that other effects play a big role here. The cooling effect on the temperature of the PENs is the largest of all the parameter changes. The mass flow of air is significantly larger than that of hydrogen. This also means that the convective heat transfer to air is much larger. As such, the change in air channel height has a large effect on PEN temperature

4.2.3. Rib Spacing

With larger rib spacing, the total power generated increases, as the cell section is now effectively increased in size. This is why this must be non-dimensionalised with respect to the cross-sectional area to give an accurate depiction of the volumetric power density. In increasing the rib spacing, you decrease the amount of shadowed area, effectively increasing the surface area. All of this added surface area is however further away from the ribs, meaning that the electron path is longer. As a result the *average* reactivity actually decreases, affecting the overall fuel utilisation. The extremes (the maximum current density and minimum current density) seem to be less affected, while the minimum current density decreases the strongest. Comparing the maximum and minimum locally observed current density, the extent of the range of valued in average current densities is noteworthy. It is much larger than half, which might be what one would intuit in a decoupled system. The effect on temperature is also notable, as the maximum temperature seems to be mostly unaffected, while the average temperature drops. This might be because of the relatively sizeable dissipative heating term due to increased convective heat transfer to air, while more PEN area with a lower reactivity is added. These conclusions align with the findings in Su et al. [32].

4.2.4. Rib Thickness

Similar to the rib spacing, the rib thickness plays a role in balancing the size of dead zones and reducing ohmic losses. A thinner rib purports less area covered, which can be seen in this parameter having the inverse effect of the rib spacing. All the effects of changing the rib thickness are exactly the opposite of increasing the rib spacing, as is expected. Altering the rib thickness is still changing the same exposed to dead surface area ratio, but in a different direction. Quite different from this intuition though is the finding that the overall effect of decreasing the thickness compared to increasing the spacing is considerably smaller in magnitude in all of the four performance criteria. This indicates that changing the ratio of exposed surface area to dead area does not work in isolation. Such behaviour can be attributed to the heat-carrying function of the current collector, as well as the overall effect that scale plays. Other scaling effects evidently play a strong role as well, and just looking at the ratio does not give the full picture. It might therefore not be a good candidate for normalisation when comparing planar cells with different geometries and sizes.

The effect of rib thickness on the temperature stands out compared to all the other results, as it seems to be more of a sigmoid shape than a linear or exponential function. This again underlines the strong secondary effect that current collectors have on the PEN assembly, in additional to their primary purpose of providing pathways for electrons.

As a final remark, it must be noted again that due to the assumption of zero reactivity in the shadowed regions, the absolute effect of rib presence will be smaller. The trend in changing the spacing will reflect this to some degree.

4.3. Sensitivity of a Corrugated Stack

The raw data for this analysis is supplied in Table B.11, with normalised results seen in Figure 4.10. Overall, the corrugated stack performs relatively similar to the planar stack.

The effects of changing the parameters is however not quite so large as they are on the ribbed planar geometry. Temperature only varies within a degree, indicating a strong thermal stability- albeit at a higher point than in the ribbed planar geometry. Other parameters stay within a 10% relative change, with the current density only varying marginally for all but the humidity.

4.3.1. Fuel Channel Flat Section Length

Decreasing fuel channel flat section length a correlates to a slight increase in both volumetric power density and fuel utilisation factor. Hence, a similar reasoning can be made as is done for the fuel channel height of the ribbed planar cell in subsection 4.2.1, and improvements in overall performance can be made by decreasing it as much as possible. This change is physically intuitive, as the flat channel section is always a dead zone for this stack type, and decreasing it also increases the diagonal section, which is much more exposed.

Using the current density as an indicator for power density is again exposed as unreliable. The results show that the trend of changing the fuel channel width on current density and normalised power are, although small in magnitude, opposite in sign. The power density follows a much more linear profile, decreasing as w_f is increased, whereas the average current density increases in a more incrementally.

Height

The height of the overall assembly (denoted by h_t) is used to control the overall aspect ratio of the mesh; increasing the height should have the same effect as decreasing all the other parameters, including the width. Such a change is a key driver for the largest differences in the parameter performance space for this mesh type, leading to strong decreases in power density and fuel utilisation. It can therefore be posed that for corrugated stacks too, miniaturisation is key, but in addition keeping the proportions of the mesh closer to unity is beneficial.

4.3.2. Slant

Slant determines the asymmetry in length of the two diagonal PEN sections. This was theorised to have a strong effect on the thermal behaviour of the assembly, but this did not appear to affect performance significantly. The effect of changing the slant at this design point proves to be nigh zero for all performance characteristics. As using the differently angled channel edges associated with slant might introduce additional complexity for the manufacturing process, the findings suggest it is better to focus on symmetrically angled channels instead.

The small magnitude of change in performance characteristics that does exist appears to be closely symmetrical for the fuel utilisation, power density, and current density. Such a change is an expected, albeit interesting emerging behaviour, as increasing the slant on one side inherently means the decrease in slant for another. If performed at an otherwise symmetrical geometry, the sign of alteration of the slant is effectively a mirroring operation. This makes the result of temperature at -10% an outlier, perhaps the result of numerical inaccuracy, considering the relative change to the design condition.

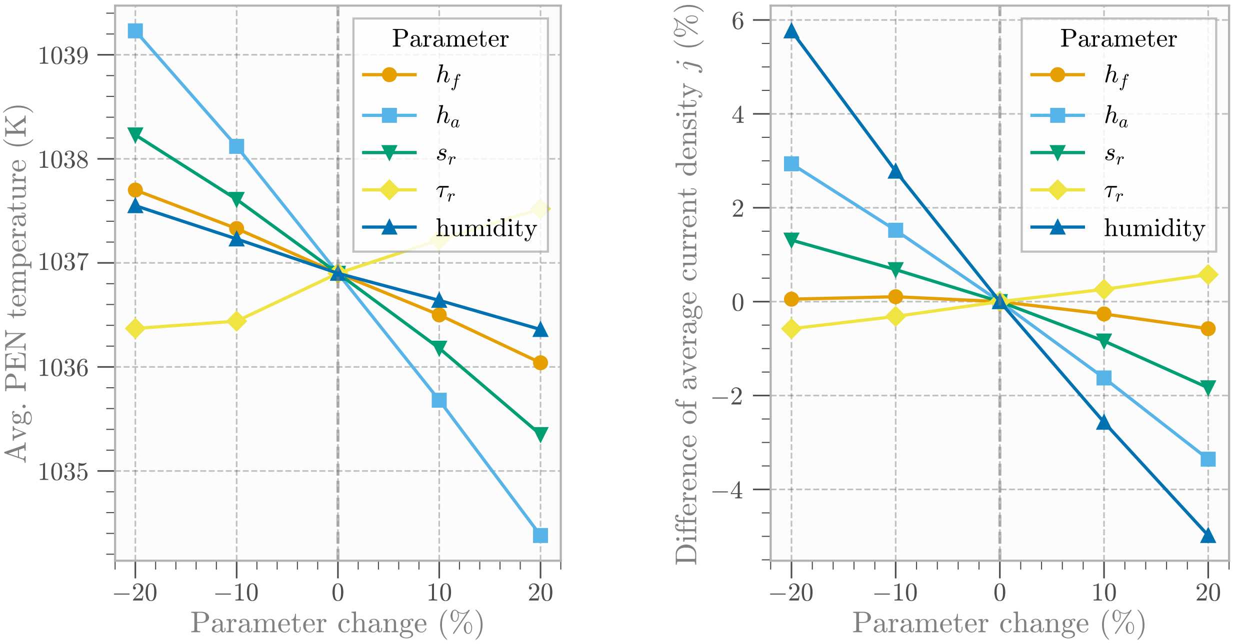

(a) Average PEN temperature.

(b) Relative difference in average PEN current density.

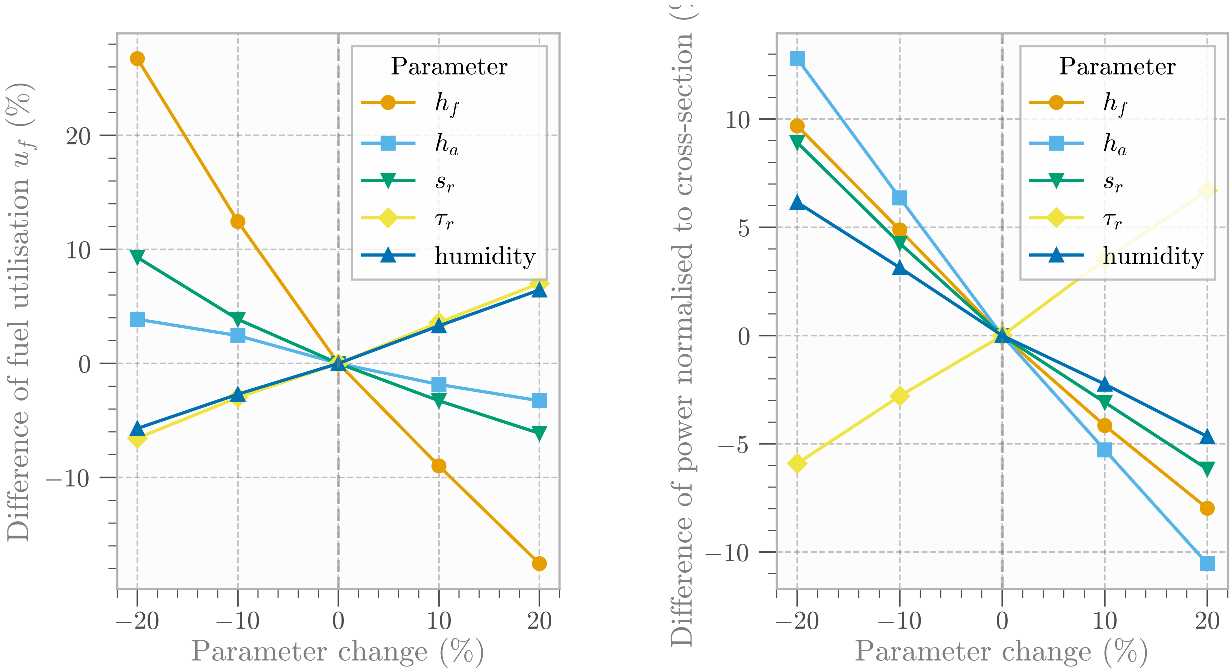

(c) Relative difference in fuel utilisation.

(d) Relative difference in power density.

Figure 4.8: Effects of varying fuel channel height h_f, air channel height h_a, rib spacing s_r, rib thickness τ_r, and inlet fuel vapour fraction on PEN temperature (4.8a), average PEN current density (4.8b), fuel utilisation (4.8c), and power density (4.8d), for a **ribbed planar** geometry relative to operational conditions described in subsection 4.0.2, as simulated using GOOSE.

4.4. Sensitivity of a Tubular Design

The raw data for this analysis is supplied in Table B.11, with normalised results seen in Figure 4.10.

Analysis shows that the tubular geometry proves to be the most sensitive design to changes in geometry for the chosen performance indicators. The magnitude of change due to changing the spacing and the diameter is consistently the largest for all of the performance characteristics.

4.4.1. Rib Thickness

The rib thickness affects the size of the dead zone on a tubular design, much like in a ribbed planar stack design. However, the practical effect of making the rib thinner is negligible, suggesting that optimisation efforts are best directed elsewhere.

4.4.2. Diameter

A significant body of literature focuses on reducing the diameter of tubular SOFCs. The effect that this alteration has is undeniable, even at the scale where they would conventionally already be considered 'micro'. Unlike for the two other meshes, the radius has a much stronger effect than the humidity of the fuel. The same as with the ribbed stack assembly, exclusively positive correlation is found between an increase in current density and power density for this cell type, said increase is significantly larger for the power than it is for the current density. This intuitively makes sense due to the ratio of exposed surface area to cross-sectional area following the cube-square-law, but it is interesting just how much stronger this effect is than on the other geometries.

As the diameter functions mostly analogous to the height of the fuel channel (and implicitly as a decrease in height of air channel) in the corrugated and ribbed planar cases, it is interesting to see that correlation between power density and fuel utilisation is now inverted. The fuel utilisation now decreases, while the power increases. Even after normalisation for the total fuel inflow increase due to the constant flux assumption, this behaviour holds.

This signifies a change in behaviour relative to the previous two cases; there, the behaviour is exactly opposite, even when normalising for the mass flow due to the constant mass flux setting. With the available data, it is unclear whether this is because of the design point, or because of how tubular fuel cells work at large. This itself gives speaks of a higher-level insight: One cannot represent design rules or trends for a broad category. Such 'rules of thumb', albeit useful, have only very small validity regions, making them unfit for top-down use in making design considerations. The overall geometry has such a strong effect on the change in performance relative to small changes in dimensions that comparison and generalisation of trends is really only possible inside of ones own class, not between stacks as a whole. This further reinforces the need for dedicated parameter studies near every type of design and operation point one might be interested in, and not taking the results of this very study as gospel for general design guide rules.

The change in trend for power density as a function of radius is also interesting. If changed in isolation, exclusively focusing on changing the radius of the tube itself might actually detriment the performance of a fuel cell- locally, increasing the radius increases the power density and average current density. This likely has to do with the added cooling effect that the relatively larger air mass flow introduced has: the temperatures depicted in Figure 4.10a vary much more greatly than its analogies in the other cases, indicating a significant change in operating point. This might also explain the change in fuel utilisation as a result of changing this parameter.

4.4.3. Spacing

How widely two tubes are spaced apart (denoted with s in this study) is not something that is often mentioned in microtubular research. Either they are stacked loosely, or very tightly, often without much second thought, as the air-to-fuel ratio is expected favour the air side of the chemical balance anyway. The results of this

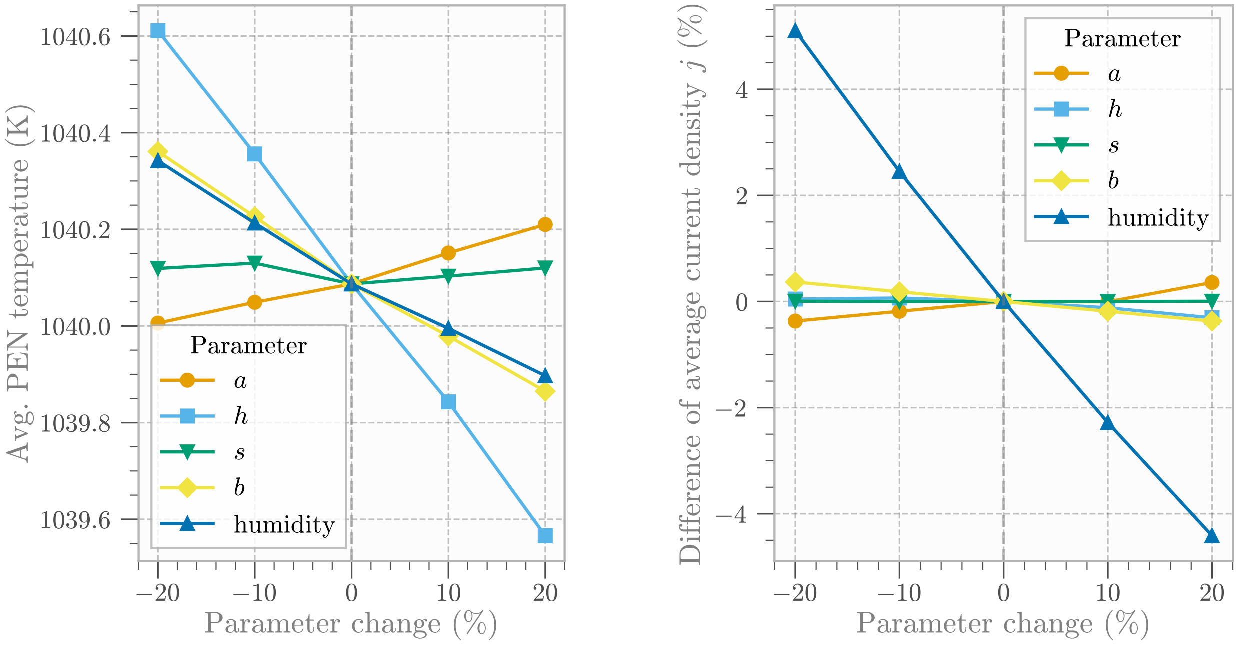

(a) Average PEN temperature.

(b) Relative difference in average PEN current density.

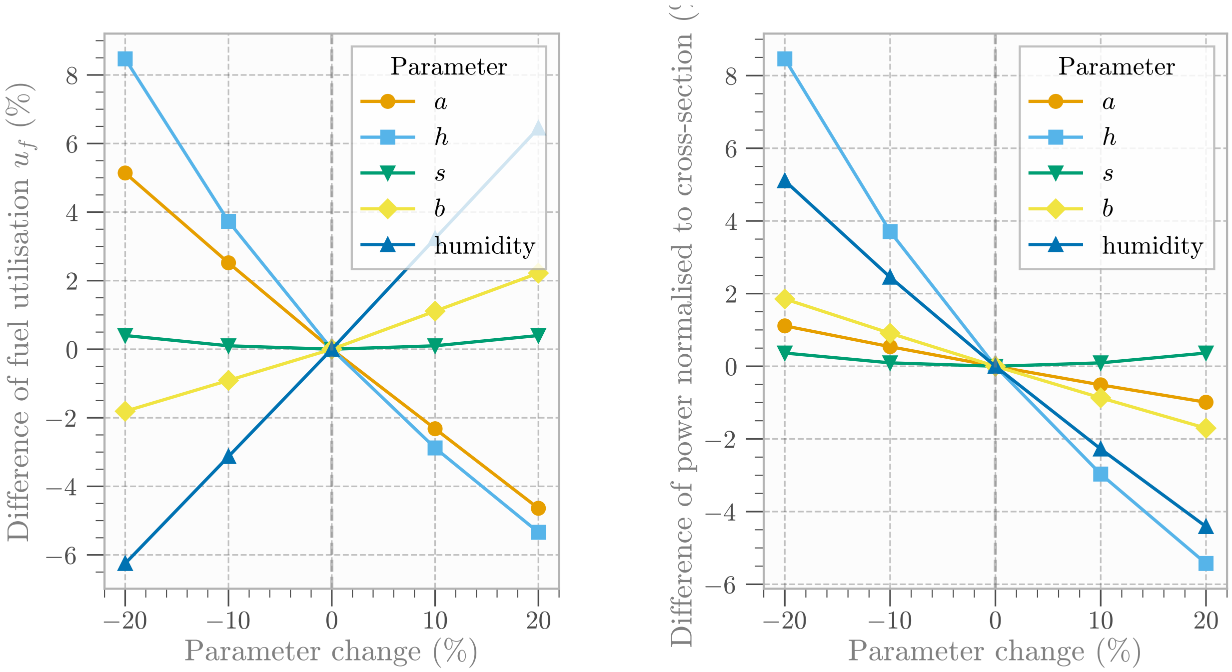

(c) Relative difference in fuel utilisation.

(d) Relative difference in power density.

Figure 4.9: Effects of varying fuel channel height h_f, air channel height h_a, rib spacing s_r, rib thickness τ_r, and inlet fuel vapour fraction on PEN temperature (4.9a), average PEN current density (4.9b), fuel utilisation (4.9c), and power density (4.9d), for a **corrugated monolithic** geometry relative to operational conditions described in subsection 4.0.3, as simulated using GOOSE.

study however show that this parameter might be the most important one yet. Its effect on power density is very large- effectively, one merely removes excess air space between the tubes. This has the side-effect of lowering the available air, and lowering the effective hydraulic diameter, causing reduced cooling with the air. All of these effects seem to follow a similar exponential relation, indicating that they likely reinforce each other, rather than working in isolation or balancing each other out. It is hard to generalise this observation into a trend or design consideration, but it does emphasise that considering geometrical tweaking cannot always be done linearly due to the inherent non-linearity of the processes being modelled.

4.5. Overall Effect of Changing Geometries

The previous sections covered the effects of changing parameters, and comparing the results to some reference case of the same mesh. Using a general tool like the one applied in this simulation also opens up the ability to compare *between* two different geometries. From such an analysis, one thing immediately becomes clear: The results of the parameter studies for the different geometries described in the previous section presented at the end of this section all have one commonality: They have *barely anything* in common.

Generally, humidity appears to be the strongest parameter, affecting all of the major performance characteristics the most. An exception for this it the tubular cell, where spacing became the most influential parameter– And that is truly the only parameter that exhibits any sign of universal correlation. No consistent correlations between parameter variations and perceived performance are found across geometries. Because they are fundamentally different meshes, the parametrisation is different, meaning true direct analogies are hard to draw. It truly is important to look at fuel cell geometries on a case-by-case basis, and not take a trend in one geometry as a promise for another.

However great the irregularity in parameter space, inverting the question to be one on a basis of performance characteristics, some trends do emerge for the cases considered. Temperature does not seem to change rapidly. This holds ground in the fact that heat is merely excess (waste) energy that must come from any of the processes modelled. It will also be distributed over fluid flow as well as solid components. With the operating temperature of an SOFC already being rather high, the effect of this small change in temperature is not nearly as critical as the deviations in other performance indicators.

As a final performance characteristic, the relative humidity of the inflowing hydrogen mix was altered for all three meshes. As this parameter change does not affect the geometry, the relation between the change in current density and the power generated is close to one-to-one. Despite the benefits that accompany an increased humidity brings outside of the stack, its effect is unanimous on all stack geometries: Decreased volumetric power density, directly as a result of overall decreased current density. Contrasting this, increasing the humidity appears to be good for the fuel utilisation. On the contrary, fuel utilisation increases, indicating a better fuel economy (notwithstanding the internalisation of the sources of such water, which itself often comes from hydrogen in pre-combustion). This confirms a global trend: for humidity, the hypothesis that an power density and fuel efficiency are inversely proportional holds ground.

According to Figure 4.8b, humidity has the strongest effect on the current density out of all parameters for the ribbed planar geometry. However, the influence it has on the volumetric power density is one of the weakest. A key finding of this is that the current density, which is traditionally taken as the most important performance characteristic, cannot be taken as an indicative surrogate value for the volumetric power density.

The other performance characteristics still change as a function of the humidity of the hydrogen mixture for the ribbed planar mesh, but its impact is small compared to the other parameters.

Similarly, but much more pronounced is the same observation for the corrugated stack for a change in humidity. Here it seems to be the only parameter that strongly affects the current density, but sinks in rank for the effect on volumetric power density.

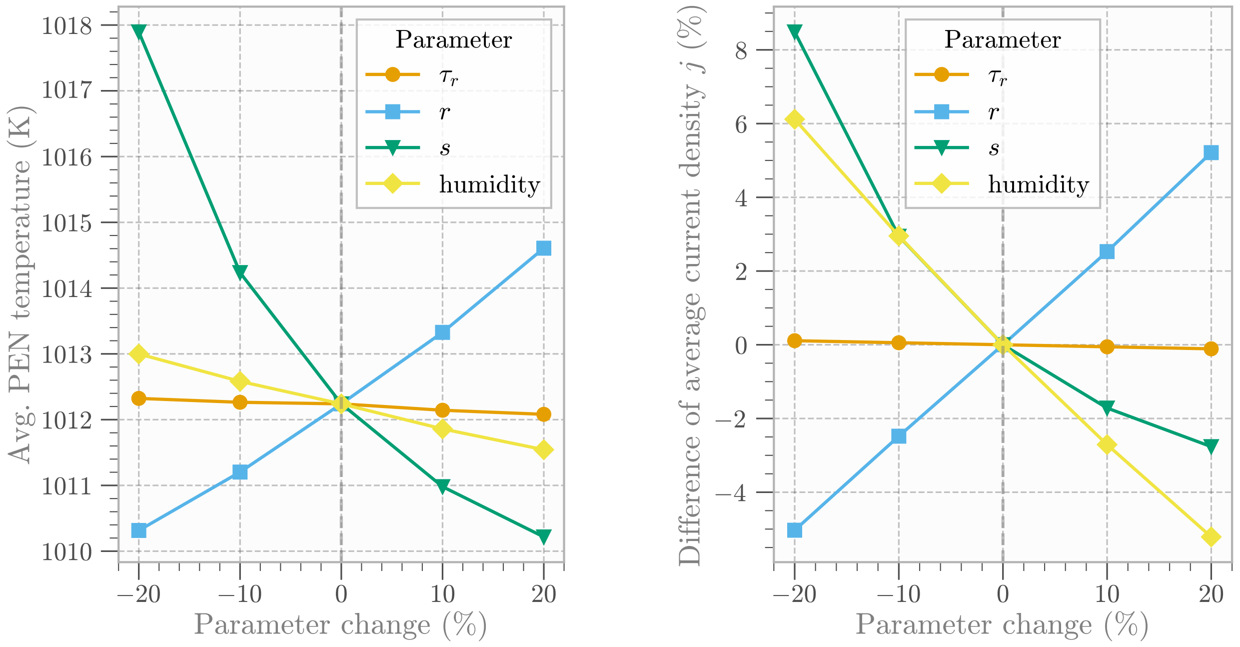

(a) Average PEN temperature.

(b) Relative difference in average PEN current density.

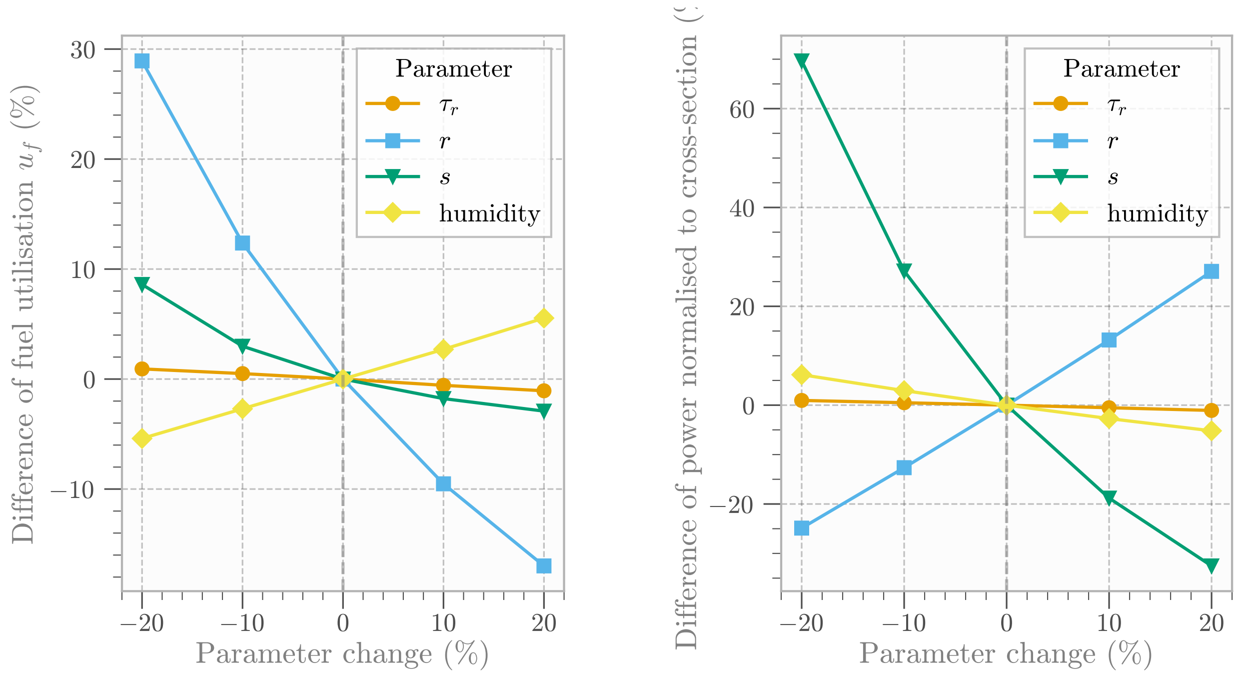

(c) Relative difference in fuel utilisation.

(d) Relative difference in power density.

Figure 4.10: Effects of varying fuel channel height h_f, air channel height h_a, rib spacing s_r, rib thickness τ_r, and inlet fuel vapour fraction on PEN temperature (4.10a), average PEN current density (4.10b), fuel utilisation (4.10c), and power density (4.10d), for a **tubular** geometry relative to operational conditions described in subsection 4.0.4, as simulated using GOOSE.

5

Conclusion

To fulfil the promise of an aviation sector based on hydrogen, it is important to assess the viability of the application of Solid Oxide Fuel Cell (SOFC) in hybrid engine architectures. Little is known on how SOFCs operate in this environment, and designs have to be made optimising for completely new performance criteria: not just fuel efficiency and cost efficiency, but now power density as a driving factor. This ties into the geometric design of complete stacks. Existing research on this topic is nigh non-existent, and the design space is huge. New tooling must be developed to start the endeavour to be able to find what are truly the driving design constraints, and how they can best be optimised.

The Geometric Oxide-cell Operating-point Simulation Environment (GOOSE) software was built with the exploration of this new field in mind, allowing rapid iteration, easy integration into existing pipelines, all the while providing a solid modular foundation to build on in the future. Great effort was put into ensuring that the model is validated, despite the general lack of available literature in this field, the greater field of fuel cell simulation, and the availability of material data relevant to such a simulation. The model was verified in parts using over 100 individual unit tests, covering over 1000 checks, spanning the implementation of models deployed (verification) up to running parts of the model in isolation where (experimental) validation data *was* available. The model was also successfully validated against an existing high-fidelity CFD simulation, and achieved great similarity in results in only a fraction of the runtime, with GOOSE completing a simulation in a few minutes, rather than several hours

The software was put to the test in a case study on performing a parameter sweep on three archetypical SOFC geometries: Planar, monolithic corrugated, and tubular. All three were had their geometries parametrised, and comparative studies were done by altering these parameters around a certain point. Studied were the general trends within these geometries, as well as those amongst each other.

From this, several critical pieces for focusing the design space were found for the geometric design of a fuel cell where power density is important;

Firstly, designing a fuel cell is not merely a trade-off between volumetric power density and fuel utilisation- there are changes which actually improve both. For both ribbed planar and corrugated architectures, this was the case for the fuel channel size parameters. It is impossible to generalise this finding for specific parameters in specific geometries, but it does emphasise the need for detailed multi-parameter optimisation studies.

Second is that the geometry does not have a strong effect on the operating temperature of fuel cells. This is much more the domain of a change in fluid inflow temperature and potentially other operational conditions. Upon altering the geometry, minor changes in overall magnitude of the temperature arise, but compared to other performance characteristics such as the volumetric power density or the fuel utilisation, the temperature remains relatively constant. The intensity of temperature gradients within the stack are also only weakly affected.

Overall, existing gradients remain, but they are not significant.

Third is a finding on what to look out for when trying to compare different geometries: current density is not always a good metric for volumetric power density, while the two are often conflated and used interchangeably in literature. For all the meshes considered, the two are proportional, but never are they identical. The current density is merely one piece of the puzzle, one factor in the volumetric power density. The integrand power density can increase much more strongly or weakly than the average current density itself, all as a function of geometry. Changing the geometry of a fuel cell affects local performance. Keeping in mind that some changes in geometry are not accompanied with differences in active surface area, translating this into a reduced normalised variable such as current density discards this information.

Fourth is a confirmation of the general trend seen in fuel cell production: overall, miniaturisation still appears to be the way forward to increase volumetric power density. However, there appear to be diminishing returns in many parameters on all three geometries, as well as optima such as in the radius of a tubular geometry, or the slant of a corrugated stack. It is likely that these patterns would also emerge for other parameters at different design points. Adding to this: for all of the observed cases, it appears that operating point shifts towards higher temperatures for finer stacks as well.

Fifth and final is a word of warning for those ready to dip their toes into the world of SOFC geometric design: Even though a trend holds for one geometry at a given design- and operating point, one cannot with certainty say it holds for another unequivocally. One such example is that of the fuel utilisation and cross-sectional power density, which both change in opposite directions for an increase in radius of the tubular cell, seem to be able to both increase hand in hand for a decrease in fuel channel size for both the planar and the corrugated geometry classes.

This work aims to function as a guidepost, a cornerstone in finding how SOFCs can be designed in such a way that they can be applied in the aviation sector, or other sectors where volumetric power density and fuel efficiency are important design factors. By opening up the use of GOOSE for everyone to use, and providing a first venture into the design space, concluding on high-level design considerations and exploration pointers, a bold step is set in this young frontier.

6

Discussion

In the production of a large model like GOOSE, as well as the analyses following, reductions in scope have to be made. That does not imply that the parts that have been cut off are insignificant however. Listed below is a discussion on features, considerations, and studies that would make excellent follow-up projects to the work that has been done in this report.

6.1. Metal-Supported cells

Right now, GOOSEs PEN representation assumes a three-component mesh. This prohibits the modelling of metal-supported cells, which allow drastic reduction of ohmic losses [119]. Adding support for this could be done by generalising the code for the PEN elements more, and implementing specific implementation overrides for the diffusion process, average material property calculations, etcetera.

6.2. Dusty Gas Model

The model used for representing the diffusion processes in the porous electrodes is sufficient, but more accurate models exist that might be more applicable to the modelling problem. One such model is the Dusty Gas Model (DGM) [120]. With the modular nature of the presented software, switching out this part of functionality should be relatively straightforward.

6.3. Multi-layer PENs

In present research, anodes and cathodes made out of multiple layers (or doping factors) are sometimes used so that diffusivity can be preferred in the upper layers, while ease of activation can be prioritised at the layer containing the TBP [74]. PENs in the presented model have electrolytes that consist of a single material only, and hence such structures cannot be represented. Similarly, **metal-supported** cells can also not be represented. Both of these shortcomings can be fixed with a relatively simple change in how PENs are represented: Instead of having only a single electrode component for each side, an array of (electrode) components can be used, ordered in the way they are physically aligned. Only the lowest layer (the one in contact with the electrolyte), contains the TBP, and should therefore need electrochemical properties. The layers above are only considered for thermal conduction, electrical pathfinding , and convection with bulk fluid. This means that the same implementation could be used for the metallic support as could be used for the non-active electrode layer. This could be implemented using dynamic dispatch. Electrical pathfinding should also need to be altered to now prefer the layer with the lowest resistivity, and take the diagonal paths split over two.

6.4. Improved Shadowing

Shadowing due to overlap of two components is currently modelled by artificially superimposing a different edge type on the shadowed part of the PEN element. This means that this element must manually be made as wide as the thickness of the current collector. This is prone to error. There is a second shortcoming to this approach: In reality, these elements will still have some activity, not zero. The species availability is reduced, but not zero.

This can be solved by changing the way shadowing is represented: Instead of having different explicit edge types, the mesher can be changed to set 'adjacent edges', that act like as if two lines of elements they are just touching. The overlap can then actually be modelled using the neighbour relationship. A check can be implemented to ensure that they are exactly the same length and resolution. Horizontal diffusion can also be implemented if desired, as described in subsection 2.8.6.

6.5. Radiative Heat Transfer

As it was alluded to in subsection 2.10.1, the simulation software could be modified to also consider radiative heat transfer. This would require a line-of-sight code to be implemented. Because all elements already have spatial information available, including normals, this should be possible to implement.

6.6. Detailed Parameter Studies Based on a Single Geometry

In the work presented, three fundamentally different geometries are investigated. This was done to both show the capabilities of GOOSE, as well as to give an indication of the degree of variability between geometries, showing that the performance cannot simply be summarised as a trade-off between power density and fuel efficiency for SOFCs as a whole. One of the found limitations of this explorative study was that such trends appear to be follow a clear trend close to some reference point, but might spiral out of control in terms of non-linearity moving further away from it. In addition to that, performance might very well be dependent on operating point as well. It would be highly insightful to explore this in more detail for a single mesh, where now the operating point (inflow temperature, pressure, air humidity) as well as the stack geometry parametrisation are varied to a much larger degree to verify these presumptions, all the while yielding more insight into the inner workings of this highly complex design space.

6.7. Novel tubular geometry variations

In addition to the current parametrisation, a third difference in tubular fuel cells can be described as a *shape factor* s, which is a term often used in geometry to denote how 'rounded' something is. A picture says more than a thousand words, and Figure 6.1 is no different. This shape factor describes the change in shape as a continuous function, but to not keep the amount of cases considered down, it was decided to only look at the two extremes: Perfectly round, corresponding to a shape factor of $s = 1$, and perfectly straight, with the corners at the current collectors and the sides respectively.

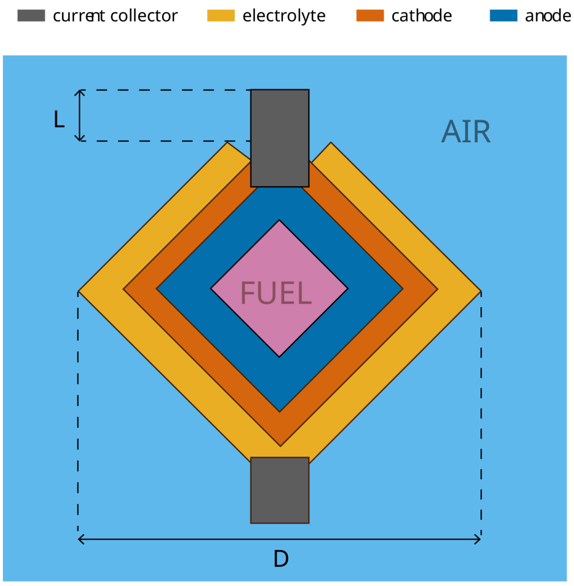

Figure 6.1: A schematic diagram of tubular cross-sectional geometry with shape factor $s = 0$. Indicated are the characteristic lengths used in its parametrisation.

6.8. Alternative tubular stacking

Albeit not really a difference in geometry, a different stacking method for tubular fuel cells could be considered. Traditionally, tubular SOFCs are stacked linearly in series: One cathode connecting to one anode, often along a single principle axis [47]. The anode side of the PEN is connected exclusively to the current collector at the top, and the cathode side is connected only to the bottom current collector.

Figure 4.6 shows the deliberate gap between the cathode and the current collector at the top. In disconnecting these two components, the electron path can only traverse towards the TBP in the PEN, and not bypass to the next cell. This type of stacking is also what is considered in the geometries presented in this work.

The resulting electron path through the electrodes to close the circuit is however, rather long. This path can be made shorter by using a different stacking paradigm. Instead of connecting the tubes vertically, they can be connected alternating as vertical-horizontal (in a *zig-zag*). This will half the (average) length of the electron path inside the cathode, leading to lower ohmic losses at the cost of introducing another dead zone. The average path length through the anode is unaffected, as the path needs to *overshoot* and backtrack through the cathode to reach the parts of the PEN closer to the opposing current collector. Note that the cells appear oriented in 90° intervals: The anode must be connected to another cathode, and vice versa. There is one other caveat for this type of stacking: Some sort of diode or other electron flow direction control device needs to be placed between two tubes to make sure that no cyclical flows occur. Without it, a full circuit would not have to leave the fuel cell, meaning that no useful power can actually be extracted.

The mesh described is shown in Figure 6.2. No parametrisation will be considered for it. It will only be simulated at shape factor $s = 1$ (round) and the same diameter as the base tubular cell, so that it can be compared to a traditional tubular geometry in isolation.

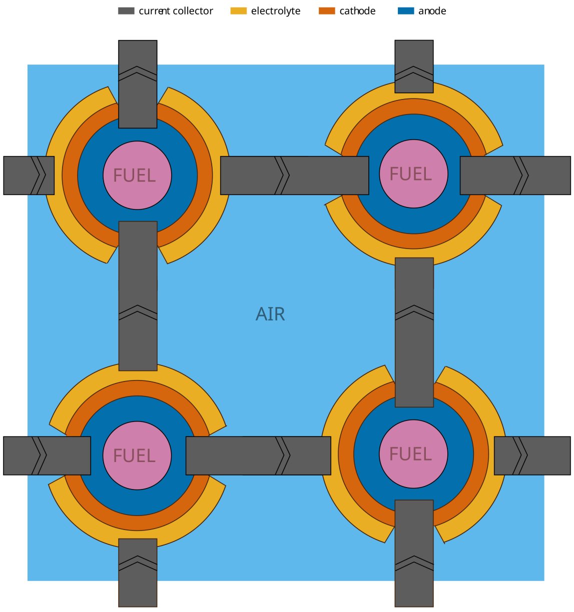

Figure 6.2: A schematic diagram of a tubular cross-sectional geometry, stacked in a *zig-zag* pattern.

References

[1] K. Calvin et al., "Ipcc, 2023: Climate change 2023: Synthesis report. contribution of working groups i, ii and iii to the sixth assessment report of the intergovernmental panel on climate change [core writing team, h. lee and j. romero (eds.)]. ipcc, geneva, switzerland.," Intergovernmental Panel on Climate Change (IPCC), Jul. 2023. DOI: 10.59327/ipcc/ar6-9789291691647.

[2] P. Fragiacomo, F. Piraino, M. Genovese, O. Corigliano, and G. D. Lorenzo, "Strategic overview on fuel cell-based systems for mobility and electrolytic cells for hydrogen production," *Procedia Computer Science*, 3rd International Conference on Industry 4.0 and Smart Manufacturing, vol. 200, pp. 1254–1263, 2022, ISSN: 1877-0509. DOI: 10.1016/j.procs.2022.01.326.

[3] H. Europe et al., *Hydrogen electrical engine novel architecture proposal*, 2023.

[4] P. G. Gonzalez, "Preliminary sizing methodologies for regional aircraft with liquid hydrogen fuel and sofc-gt-battery hybrid-electric powertrain," M.S. thesis, 2022.

[5] K. Kuterbekov et al., "Classification of solid oxide fuel cells," *Nanomaterials*, vol. 12, p. 1059, 2022. DOI: 10.3390/nano12071059.

[6] S. Pirou et al., "Production of a monolithic fuel cell stack with high power density," en, *Nature Communications*, vol. 13, no. 1, p. 1263, 2022, ISSN: 2041-1723. DOI: 10.1038/s41467-022-28970-w. [Online]. Available: https://www.nature.com/articles/s41467-022-28970-w.

[7] S. Kawasaki et al., "Long monolithic planar cell: A new sofc design for high power density generation," Japanese, *ECS Proceedings Volumes*, vol. 1997-40, no. 1, p. 171, 1997, ISSN: 2576-1579. DOI: 10.1149/199740.0171PV. [Online]. Available: https://dx.doi.org/10.1149/199740.0171PV.

[8] O. Yamamoto, "高温固体電解質燃料電池用材料," Japanese, **資源と素材**, vol. 105, no. 15, pp. 1119–1124, 1989. DOI: 10.2473/shigentosozai.105.1119.

[9] Y. Du and O. S. Fatoba, "Additive manufacturing of advanced solid oxide fuel cells - a review," *ECS Transactions*, vol. 91, no. 1, p. 277, 2019, ISSN: 1938-5862. DOI: 10.1149/09101.0277ecst. [Online]. Available: https://dx.doi.org/10.1149/09101.0277ecst.

[10] K. Jia et al., "A new and simple way to prepare monolithic solid oxide fuel cell stack by stereolithography 3d printing technology using 8 mol% yttria stabilized zirconia photocurable slurry," *Journal of the European Ceramic Society*, vol. 42, no. 10, pp. 4275–4285, 2022, ISSN: 0955-2219. DOI: 10.1016/j.jeurceramsoc.2022.03.060.

[11] J. W. Fergus, "Sealants for solid oxide fuel cells," *Journal of Power Sources*, vol. 147, no. 1, pp. 46–57, 2005, ISSN: 0378-7753. DOI: 10.1016/j.jpowsour.2005.05.002.

[12] D. H. Huang and D. K. Huzel, "Dynamic seals for high-temperature surface," in American Institute of Aeronautics and Astronautics, 1992, p. 242.

[13] S. E. Hosseini, *Fundamentals of Hydrogen Production and Utilization in Fuel Cell Systems*, en. Elsevier, 2023, p. 378. [Online]. Available: `https://books.google.nl/books?id=_np5EAAAQBAJ`.

[14] A. Hafsia, Z. Bariza, H. Djamel, B. M. Hocine, G. M. Andreadis, and A. Soumia, "SOFC fuel cell heat production: Analysis," *Energy Procedia*, Impact of Integrated Clean Energy on the Future of the Mediterranean Environment? Vol. 6, pp. 643–650, Jan. 2011, ISSN: 1876-6102. DOI: `10.1016/j.egypro.2011.05.074`. Accessed: Feb. 24, 2025. [Online]. Available: `https://www.sciencedirect.com/science/article/pii/S1876610211014858`.

[15] A. De Bernardinis, E. Frappé, O. Bethoux, and C. Marchand, "Multi-port power converter for segmented pem fuel cell in transport application," *European Physical Journal Applied Physics*, vol. 58, p. 20 901, 2012. DOI: `10.1051/epjap/2012120056`.

[16] T. Yamaguchi, S. Shimizu, T. Suzuki, Y. Fujishiro, and M. Awano, "Fabrication and evaluation of a novel cathode-supported honeycomb sofc stack," *Materials Letters*, vol. 63, no. 29, pp. 2577–2580, 2009, ISSN: 0167-577X. DOI: `10.1016/j.matlet.2009.09.009`.

[17] P. B. Balbuena, "Electrolyte materials - issues and challenges," en, 2014, pp. 82–97. DOI: `10.1063/1.4878481`. [Online]. Available: `https://pubs.aip.org/aip/acp/article/1597/1/82-97/800012`.

[18] R. Bove and S. Ubertini, *Modeling Solid Oxide Fuel Cells*, N. P. Bansal, Ed. Dordrecht: Springer Netherlands, 2008, Also ISBN 978-1-4020-6995-6, ISBN: 978-1-4020-6994-9. [Online]. Available: `http://link.springer.com/10.1007/978-1-4020-6995-6`.

[19] D. Andersson, E. Åberg, J. Eborn, J. Yuan, and B. Sunden, "Dynamic modeling of a solid oxide fuel cell system in modelica," 2011, pp. 593–602. DOI: `10.3384/ecp11063593`.

[20] L. van Biert, M. Godjevac, K. Visser, and P. V. Aravind, "Dynamic modelling of a direct internal reforming solid oxide fuel cell stack based on single cell experiments," *Applied Energy*, vol. 250, pp. 976–990, 2019, ISSN: 0306-2619. DOI: `10.1016/j.apenergy.2019.05.053`. [Online]. Available: `http://www.scopus.com/inward/record.url?scp=85065518240&partnerID=8YFLogxK`.

[21] N. F. Harun, L. Shadle, D. Oryshchyn, and D. Tucker, "Fuel utilization effects on system efficiency and solid oxide fuel cell performance in gas turbine hybrid systems," presented at the GT2017, 2017. DOI: `10.1115/GT2017-64055`. [Online]. Available: `https://doi.org/10.1115/GT2017-64055`.

[22] J. Kupecki, J. Milewski, A. Szczesniak, R. Bernat, and K. Motylinski, "Dynamic numerical analysis of cross-, co-, and counter-current flow configuration of a 1 kw-class solid oxide fuel cell stack," *International Journal of Hydrogen Energy*, vol. 40, no. 45, pp. 15 834–15 844, 2015, ISSN: 0360-3199. DOI: `10.1016/j.ijhydene.2015.07.008`.

[23] J. Kupecki, K. Motylinski, and J. Milewski, "Dynamic analysis of direct internal reforming in a sofc stack with electrolyte-supported cells using a quasi-1d model," en, *Applied Energy*, vol. 227, no. C, pp. 198–205, 2018.

[24] J. Milewski and A. Miller, "Influences of the type and thickness of electrolyte on solid oxide fuel cell hybrid system performance," *Journal of Fuel Cell Science and Technology*, vol. 3, no. 4, pp. 396–402, 2006, ISSN: 1550-624X. DOI: `10.1115/1.2349519`.

[25] J. Milewski, "A mathematical model of sofc: A proposal," en, *Fuel Cells*, vol. 12, no. 5, pp. 709–721, 2012, ISSN: 1615-6854. DOI: `10.1002/fuce.201100150`.

[26] Z. Qu, P. V. Aravind, N. J. J. Dekker, A. H. H. Janssen, N. Woudstra, and A. H. M. Verkooijen, "Three-dimensional thermo-fluid and electrochemical modeling of anode-supported planar solid oxide fuel cell," *Journal of Power Sources*, Selected Papers from the, Eleventh Grove Fuel Cell Symposium London, United Kingdom and Selected Papers from E-Mrs Spring Meeting 2009, Strasbourg, France, vol. 195, no. 23, pp. 7787–7795, 2010, ISSN: 0378-7753. DOI: 10.1016/j.jpowsour.2010.02.016.

[27] M. Riedel, M. P. Heddrich, A. Ansar, Q. Fang, L. Blum, and K. A. Friedrich, "Pressurized operation of solid oxide electrolysis stacks: An experimental comparison of the performance of 10-layer stacks with fuel electrode and electrolyte supported cell concepts," *Journal of Power Sources*, vol. 475, p. 228 682, 2020, ISSN: 0378-7753. DOI: 10.1016/j.jpowsour.2020.228682.

[28] A. Sciacovelli and V. Verda, "Entropy generation minimization in a tubular solid oxide fuel cell," en, American Society of Mechanical Engineers Digital Collection, 2009, pp. 809–818. DOI: 10.1115/IMECE2008-68910. [Online]. Available: https://dx.doi.org/10.1115/IMECE2008-68910.

[29] S. C. Singhal and K. Kendall, *High-temperature Solid Oxide Fuel Cells: Fundamentals, Design and Applications*, en. Elsevier, 2003, p. 423. [Online]. Available: https://books.google.nl/books?id=go_m4Hf2uPoC.

[30] H. L. Lee, N. G. Han, M. S. Kim, Y. S. Kim, and D. K. Kim, "Studies on the effect of flow configuration on the temperature distribution and performance in a high current density region of solid oxide fuel cell," *Applied Thermal Engineering*, vol. 206, p. 118 120, 2022, ISSN: 1359-4311. DOI: 10.1016/j.applthermaleng.2022.118120.

[31] A. B. Lambe and J. R. R. A. Martins, "Extensions to the design structure matrix for the description of multidisciplinary design, analysis, and optimization processes," *Structural and Multidisciplinary Optimization*, vol. 46, pp. 273–284, 2012. DOI: 10.1007/s00158-012-0763-y.

[32] S. Su, X. Gao, Q. Zhang, W. Kong, and D. Chen, "Anode- versus cathode-supported solid oxide fuel cell: Effect of cell design on the stack performance," *International Journal of Electrochemical Science*, vol. 10, pp. 2487–2503, 2015.

[33] S. Lu, M. Zhang, J. Wu, and W. Kong, "Performance investigation on mono-block-layer build type solid oxide fuel cells with a vertical rib design," en, *Energies*, vol. 15, no. 3, p. 979, 2022, ISSN: 1996-1073. DOI: 10.3390/en15030979. [Online]. Available: https://www.mdpi.com/1996-1073/15/3/979.

[34] J. Fleig, "Solid oxide fuel cell cathodes: Polarization mechanisms and modeling of the electrochemical performance," en, *Annual Review of Materials Research*, vol. 33, no. 1, pp. 361–382, 2003, ISSN: 1531-7331, 1545-4118. DOI: 10.1146/annurev.matsci.33.022802.093258. [Online]. Available: https://www.annualreviews.org/doi/10.1146/annurev.matsci.33.022802.093258.

[35] S. P. Jiang and Q. Li, *Introduction to Fuel Cells: Electrochemistry and Materials*, en. Singapore: Springer, 2022, ISBN: 978-981-10-7625-1. DOI: 10.1007/978-981-10-7626-8. [Online]. Available: https://link.springer.com/10.1007/978-981-10-7626-8.

[36] K. W. Harrison, R. Remick, and G. D. Martin, "Hydrogen production: Fundamentals and case study summaries," en, presented at the NREL, 2010.

[37] PalmSens. "Origins of electrochemical potentials," PalmSens. [Online]. Available: https://www.palmsens.com/knowledgebase-article/origins-of-electrochemical-potentials/.

[38] F. Mulder, *Set3085 hydrogen technology electrolysis 1*, Kluyverweg 1, 2629 HS Delft, 2022. [Online]. Available: `https://brightspace.tudelft.nl/d2l/le/content/401575/viewContent/2379071/View`.

[39] A. Burcat and B. Ruscic, "Third millennium ideal gas and condensed phase thermochemical database for combustion (with update from active thermochemical tables).," Argonne National Lab. (ANL), Argonne, IL (United States), Tech. Rep., Jul. 2005. DOI: `10.2172/925269`. [Online]. Available: `https://www.osti.gov/biblio/925269`.

[40] R. P. Brent, *Algorithms for minimization without derivatives* (Prentice-Hall series in automatic computation), eng. Englewood Cliffs, N.J.: Prentice-Hall, 1972, OCLC: 515987, ISBN: 9780130223357. Accessed: Jun. 18, 2025. [Online]. Available: `http://www.gbv.de/dms/hbz/toc/ht000499427.pdf`.

[41] I. EGnG Technical Services, "Fuel cell handbook (seventh edition)," en, Morgantown, West Virginia, Tech. Rep., 2004. [Online]. Available: `https://doi.org/10.2172/834188`.

[42] R. Guidelli et al., "Defining the transfer coefficient in electrochemistry: An assessment (iupac technical report)," en, *Pure and Applied Chemistry*, vol. 86, no. 2, pp. 245–258, 2014, ISSN: 1365-3075. DOI: `10.1515/pac-2014-5026`. [Online]. Available: `https://www.degruyter.com/document/doi/10.1515/pac-2014-5026/html?lang=en`.

[43] A. J. Bard and L. R. Faulkner, *Electrochemical methods: fundamentals and applications*, en, 2nd. New York: Wiley, 2001, p. 833, ISBN: 978-0-471-04372-0.

[44] H. Zhu and R. J. Kee, "Modeling Distributed Charge-Transfer Processes in SOFC Membrane Electrode Assemblies," en, *Journal of The Electrochemical Society*, vol. 155, no. 7, B715, May 2008, ISSN: 1945-7111. DOI: `10.1149/1.2913152`. Accessed: Feb. 19, 2025. [Online]. Available: `https://iopscience.iop.org/article/10.1149/1.2913152/meta`.

[45] E. J. F. Dickinson and A. J. Wain, "The Butler-Volmer equation in electrochemical theory: Origins, value, and practical application," *Journal of Electroanalytical Chemistry*, Dr. Richard Compton 65th birthday Special issue, vol. 872, p. 114 145, Sep. 2020, ISSN: 1572-6657. DOI: `10.1016/j.jelechem.2020.114145`. Accessed: Feb. 19, 2025. [Online]. Available: `https://www.sciencedirect.com/science/article/pii/S1572665720303283`.

[46] D. A. Noren and M. A. Hoffman, "Clarifying the butler-volmer equation and related approximations for calculating activation losses in solid oxide fuel cell models," *Journal of Power Sources*, vol. 152, pp. 175–181, 2005, ISSN: 0378-7753. DOI: `10.1016/j.jpowsour.2005.03.174`. [Online]. Available: `https://www.sciencedirect.com/science/article/pii/S037877530500563X`.

[47] R. García, "Production of micro-tubular solid oxide fuel cells," Ph.D. dissertation, University of Trento, Milan, 2011. [Online]. Available: `https://www.semanticscholar.org/paper/Production-of-Micro-Tubular-Solid-Oxide-Fuel-Cells-Garc%C3%ADa/4852178054cca8746c3d8602d6141fc6d29aa8bd`.

[48] T. Horita, K. Yamaji, N. Sakai, H. Yokokawa, T. Kawada, and T. Kato, "Oxygen reduction sites and diffusion paths at la0.9sr0.1mno3 $-$ x/yttria-stabilized zirconia interface for different cathodic overvoltages by secondary-ion mass spectrometry," *Solid State Ionics*, vol. 127, no. 1, pp. 55–65, 2000, ISSN: 0167-2738. DOI: `10.1016/S0167-2738(99)00276-3`.

[49] J. Fehribach and R. O'Hayre, "Triple phase boundaries in solid-oxide cathodes," *SIAM Journal of Applied Mathematics*, vol. 70, pp. 510–530, 2009. DOI: `10.1137/080722667`.

[50] C. W. Thurner, K. Ploner, D. Werner, S. Penner, E. Portenkirchner, and B. Klötzer, "New Insights into the Hydrogen Evolution Mechanism near the Ni/YSZ Triple Phase Boundary during Steam Electrolysis: A patterned Model Electrode Study," *ACS Electrochemistry*, vol. 1, no. 3, pp. 315–327, Nov. 2024, ISSN: 2997-0571. DOI: `10.1021/acselectrochem.4c00031`. Accessed: Jul. 9, 2025. [Online]. Available: `https://www.ncbi.nlm.nih.gov/pmc/articles/PMC11891889/`.

[51] W. Kong, H. Zhu, Z. Fei, and Z. Lin, "A modified dusty gas model in the form of a fick's model for the prediction of multicomponent mass transport in a solid oxide fuel cell anode," *Journal of Power Sources*, vol. 206, pp. 171–178, 2012, ISSN: 0378-7753. DOI: `10.1016/j.jpowsour.2012.01.107`.

[52] M. Ni, M. K. H. Leung, and D. Y. C. Leung, "An electrochemical model of a solid oxide steam electrolyzer for hydrogen production," en, *Chemical Engineering & Technology*, vol. 29, no. 5, pp. 636–642, 2006, ISSN: 0930-7516, 1521-4125. DOI: `10.1002/ceat.200500378`. [Online]. Available: `https://onlinelibrary.wiley.com/doi/10.1002/ceat.200500378`.

[53] P. Aguiar, C. S. Adjiman, and N. P. Brandon, "Anode-supported intermediate temperature direct internal reforming solid oxide fuel cell. i: Model-based steady-state performance," *Journal of Power Sources*, vol. 138, no. 1, pp. 120–136, 2004, ISSN: 0378-7753. DOI: `10.1016/j.jpowsour.2004.06.040`.

[54] A. Sorce, A. Greco, L. Magistri, and P. Costamagna, "Fdi oriented modeling of an experimental sofc system, model validation and simulation of faulty states," *Applied Energy*, vol. 136, pp. 894–908, 2014, ISSN: 0306-2619. DOI: `10.1016/j.apenergy.2014.03.074`.

[55] J. H. Nam and D. H. Jeon, "A comprehensive micro-scale model for transport and reaction in intermediate temperature solid oxide fuel cells," *Electrochimica Acta*, vol. 51, no. 17, pp. 3446–3460, Apr. 2006, ISSN: 0013-4686. DOI: `10.1016/j.electacta.2005.09.041`. Accessed: Jan. 17, 2025. [Online]. Available: `https://www.sciencedirect.com/science/article/pii/S0013468605011631`.

[56] S. H. Chan, K. A. Khor, and Z. T. Xia, "A complete polarization model of a solid oxide fuel cell and its sensitivity to the change of cell component thickness," *Journal of Power Sources*, vol. 93, no. 1, pp. 130–140, 2001, ISSN: 0378-7753. DOI: `10.1016/S0378-7753(00)00556-5`.

[57] R. Krishna and J. M. van Baten, "Investigating the validity of the bosanquet formula for estimation of diffusivities in mesopores," *Chemical Engineering Science*, vol. 69, no. 1, pp. 684–688, 2012, ISSN: 0009-2509. DOI: `10.1016/j.ces.2011.11.026`.

[58] H. Yakabe, M. Hishinuma, M. Uratani, Y. Matsuzaki, and I. Yasuda, "Evaluation and modeling of performance of anode-supported solid oxide fuel cell," *Journal of Power Sources*, vol. 86, no. 1, pp. 423–431, 2000, ISSN: 0378-7753. DOI: `10.1016/S0378-7753(99)00444-9`.

[59] F. Zhao, T. J. Armstrong, and A. V. Virkar, "Measurement of o 2 n 2 effective diffusivity in porous media at high temperatures using an electrochemical cell," en, *Journal of The Electrochemical Society*, vol. 150, no. 3, A249, 2003, ISSN: 1945-7111. DOI: `10.1149/1.1540156`. [Online]. Available: `https://iopscience.iop.org/article/10.1149/1.1540156/meta`.

[60] E. L. Cussler, *Diffusion: Mass Transfer in Fluid Systems*, en, Jan. 2009. DOI: `10.1017/CBO9780511805134`. Accessed: Jun. 6, 2025. [Online]. Available: `https://www.cambridge.org/highereducation/books/diffusion/52ADCBD2746CA771AFF0CC572CE190A6`.

[61] B. E. Poling, J. M. Prausnitz, and J. P. O'Connell, *The properties of gases and liquids*, en, 5th ed. New York: McGraw-Hill, 2001, p. 1.

[62] C. F. C. J. O. Hirschfelder and R. B. Bird, “Molecular theory of gases and liquids.,” en, *Journal of Polymer Science*, vol. 17, no. 83, pp. 116–116, 1955, ISSN: 1542-6238. DOI: 10.1002/pol.1955.120178311. Accessed: Jun. 20, 2025. [Online]. Available: https://onlinelibrary.wiley.com/doi/abs/10.1002/pol.1955.120178311.

[63] M. Asaeda, N. Morio, and T. Ryozo, “Isobaric diffusion of gases in packed beds of fine particles,” *Journal of Chemical Engineering of Japan*, vol. 7, pp. 173–180, 1974. DOI: 10.1252/jcej.7.173.

[64] T. Glenn, “Chemistry 101a general college chemistry,” en, in City College of San Francisco, Aug. 2019, ch. 5 Molecular Speed Distribution, p. 9. Accessed: Jun. 20, 2025. [Online]. Available: https://chem.libretexts.org/Courses/City_College_of_San_Francisco/Chemistry_101A/Topic_C%3A_Gas_Laws_and_Kinetic_Molecular_Theory/05%3A_Gases/5.09%3A_Molecular_Speeds.

[65] J. Moore, “Chemprime,” en, in E. Vitz, Ed. University of Wisconsin-Madison, May 2016, ch. 9 Kinetic Theory of Gases, p. 15. Accessed: Jun. 20, 2025. [Online]. Available: https://chem.libretexts.org/Bookshelves/General_Chemistry/ChemPRIME_(Moore_et_al.)/09%3A_Gases/9.15%3A_Kinetic_Theory_of_Gases-_Molecular_Speeds.

[66] S. Liu, C. Song, and Z. Lin, “The effects of the interconnect rib contact resistance on the performance of planar solid oxide fuel cell stack and the rib design optimization,” *Journal of Power Sources*, vol. 183, no. 1, pp. 214–225, Aug. 2008, ISSN: 0378-7753. DOI: 10.1016/j.jpowsour.2008.04.054. Accessed: Mar. 20, 2025. [Online]. Available: https://www.sciencedirect.com/science/article/pii/S0378775308008288.

[67] J. Zhang, C. Lenser, N. H. Menzler, and O. Guillon, “Comparison of solid oxide fuel cell (SOFC) electrolyte materials for operation at 500 degrees celsius,” *Solid State Ionics*, vol. 344, p. 115 138, Jan. 2020, ISSN: 0167-2738. DOI: 10.1016/j.ssi.2019.115138. Accessed: Mar. 20, 2025. [Online]. Available: https://www.sciencedirect.com/science/article/pii/S0167273819307039.

[68] J. C. Bachman et al., “Inorganic solid-state electrolytes for lithium batteries: Mechanisms and properties governing ion conduction,” *Chemical Reviews*, vol. 116, no. 1, pp. 140–162, 2016, ISSN: 0009-2665. DOI: 10.1021/acs.chemrev.5b00563. [Online]. Available: https://doi.org/10.1021/acs.chemrev.5b00563.

[69] J. Fergus, “Electrolyte for solid oxide fuel cells,” *Journal of Power Sources - J POWER SOURCES*, vol. 162, pp. 30–40, 2006. DOI: 10.1016/j.jpowsour.2006.06.062.

[70] D. E. Knuth, *The Art of Computer Programming, Volume 1: Fundamental Algorithms*, en, 3rd ed. Addison-Wesley, 1997, vol. 1, ISBN: 978-0-201-89683-1. Accessed: Jun. 20, 2025. [Online]. Available: https://www.book-info.com/isbn/0-201-89683-4.htm.

[71] D. Vignesh, E. Rout, and B. P. Swain, *Proton Conductors: Physics and Technological Advancements for PC-SOFC*. Singapore: Springer Nature Singapore, 2023. [Online]. Available: https://doi.org/10.1007/978-981-99-3866-7_1.

[72] D. Chen, Z. Lin, H. Zhu, and R. J. Kee, “Percolation theory to predict effective properties of solid oxide fuel-cell composite electrodes,” *Journal of Power Sources*, vol. 191, no. 2, pp. 240–252, Jun. 2009, ISSN: 0378-7753. DOI: 10.1016/j.jpowsour.2009.02.051. Accessed: Jan. 20, 2025. [Online]. Available: https://www.sciencedirect.com/science/article/pii/S0378775309003681.

[73] P. Costamagna, P. Costa, and V. Antonucci, "Micro-modelling of solid oxide fuel cell electrodes," *Electrochimica Acta*, vol. 43, no. 3, pp. 375–394, 1998, ISSN: 0013-4686. DOI: `10.1016/S0013-4686(97)00063-7`. [Online]. Available: `https://www.sciencedirect.com/science/article/pii/S0013468697000637`.

[74] D. H. Jeon, J. H. Nam, and C.-J. Kim, "Microstructural Optimization of Anode-Supported Solid Oxide Fuel Cells by a Comprehensive Microscale Model," en, *Journal of The Electrochemical Society*, vol. 153, no. 2, A406, Jan. 2006, ISSN: 1945-7111. DOI: `10.1149/1.2139954`. Accessed: Feb. 3, 2025. [Online]. Available: `https://iopscience.iop.org/article/10.1149/1.2139954/meta`.

[75] J. Stam, D. Roekaerts, and P. V. Aravind, "Modeling of radiative heat transfer in solid oxide fuel cells," M.S. thesis, 2017.

[76] T. Ota, M. Koyama, C. J. Wen, K. Yamada, and H. Takahashi, "Object-based modeling of sofc system: Scientific advances in fuel cell systems," *Journal of Power Sources*, vol. 118, no. 1-2, pp. 430–439, 2003, ISSN: 0378-7753. DOI: `10.1016/S0378-7753(03)00109-5`. [Online]. Available: `http://www.scopus.com/inward/record.url?scp=0038823758&partnerID=8YFLogxK`.

[77] F. Mulder, *Set3085 hydrogen technology fuel cells*, Kluyverweg 1, 2629 HS Delft, 2022.

[78] W. C. Reynolds and P. Colonna, *Thermodynamics: Fundamentals and Engineering Applications*, en. 2018, ISBN: 9780521862738. [Online]. Available: `files/156/4F53402087B26F32BC8DC00DEE5ED068.html`.

[79] A. F. Mills and C. F. M. Coimbra, *Basic heat and mass transfer*, eng, Third edition. San Diego, California: Prentice Hall, 2015, p. 1001.

[80] J. M. Perkel, "Why scientists are turning to Rust," en, *Nature*, vol. 588, no. 7836, pp. 185–186, Dec. 2020. DOI: `10.1038/d41586-020-03382-2`. Accessed: Jun. 24, 2025. [Online]. Available: `https://www.nature.com/articles/d41586-020-03382-2`.

[81] M. Barker et al., "Introducing the FAIR Principles for research software," en, *Scientific Data*, vol. 9, no. 1, p. 622, Oct. 2022, ISSN: 2052-4463. DOI: `10.1038/s41597-022-01710-x`. Accessed: Jun. 24, 2025. [Online]. Available: `https://www.nature.com/articles/s41597-022-01710-x`.

[82] A. Connolly et al., "Software Engineering Practices in Academia: Promoting the 3rs—Readability, Resilience, and Reuse," *Harvard Data Science Review*, vol. 5, no. 2, Apr. 2023, https://hdsr.mitpress.mit.edu/pub/f0f7h5cu.

[83] R. L. committe. "The rust book - validating references with lifetimes. "[Online]. Available: `https://doc.rust-lang.org/book/ch10-03-lifetime-syntax.html`.

[84] P. Costamagna, A. Selimovic, M. Del Borghi, and G. Agnew, "Electrochemical model of the integrated planar solid oxide fuel cell (ip-sofc)," *Chemical Engineering Journal*, vol. 102, no. 1, pp. 61–69, 2004, ISSN: 1385-8947. DOI: `10.1016/j.cej.2004.02.005`.

[85] Y. M. Barzi, A. Raoufi, and H. Lari, "Performance analysis of a SOFC button cell using a CFD model," *International Journal of Hydrogen Energy*, vol. 35, no. 17, pp. 9468–9478, Sep. 2010, ISSN: 0360-3199. DOI: `10.1016/j.ijhydene.2010.05.086`. Accessed: Feb. 19, 2025. [Online]. Available: `https://www.sciencedirect.com/science/article/pii/S0360319910010554`.

[86] L. Wehrle, Y. Wang, P. Boldrin, N. P. Brandon, O. Deutschmann, and A. Banerjee, "Optimizing solid oxide fuel cell performance to re-evaluate its role in the mobility sector," *ACS Environmental Au*, vol. 2, no. 1, pp. 42–64, 2022. DOI: `10.1021/acsenvironau.1c00014`. [Online]. Available: `https://doi.org/10.1021/acsenvironau.1c00014`.

[87] P. Costamagna and K. Honegger, "Modeling of solid oxide heat exchanger integrated stacks and simulation at high fuel utilization," *Journal of The Electrochemical Society*, vol. 145, no. 11, p. 3995, Nov. 1998. DOI: `10.1149/1.1838904`. [Online]. Available: `https://dx.doi.org/10.1149/1.1838904`.

[88] M. Hering, J. Brouwer, and W. Winkler, "Evaluation and optimization of a micro-tubular solid oxide fuel cell stack model including an integrated cooling system," *Journal of Power Sources*, vol. 303, pp. 10–16, 2016, ISSN: 0378-7753. DOI: `10.1016/j.jpowsour.2015.09.036`.

[89] L. Petruzzi, S. Cocchi, and F. Fineschi, "A global thermo-electrochemical model for SOFC systems design and engineering," *Journal of Power Sources*, Scientific Advances in Fuel Cell Systems, vol. 118, no. 1, pp. 96–107, May 2003, ISSN: 0378-7753. DOI: `10.1016/S0378-7753(03)00067-3`. Accessed: Jan. 20, 2025. [Online]. Available: `https://www.sciencedirect.com/science/article/pii/S0378775303000673`.

[90] A. Yahya, D. Ferrero, H. Dhahri, P. Leone, K. Slimi, and M. Santarelli, "Electrochemical performance of solid oxide fuel cell: Experimental study and calibrated model," *Energy*, vol. 142, pp. 932–943, Jan. 2018, ISSN: 0360-5442. DOI: `10.1016/j.energy.2017.10.088`. Accessed: Jul. 9, 2025. [Online]. Available: `https://www.sciencedirect.com/science/article/pii/S0360544217317930`.

[91] M. Radovic, E. Lara-Curzio, R. M. Trejo, H. Wang, and W. D. Porter, "Thermophysical Properties of YSZ and Ni-YSZ as a Function of Temperature and Porosity," en, in *Advances in Solid Oxide Fuel Cells II: Ceramic Engineering and Science Proceedings*, John Wiley & Sons, Ltd, 2006, ch. 8, pp. 79–85, ISBN: 9780470291337. DOI: `10.1002/9780470291337.ch8`. Accessed: Jan. 15, 2025. [Online]. Available: `https://onlinelibrary.wiley.com/doi/abs/10.1002/9780470291337.ch8`.

[92] L. van Biert, P. Segovia Castillo, A. Haseltalab, and R. R. Negenborn, "A reduced-order model of a solid oxide fuel cell stack for model predictive control," en, *Proceedings of the International Ship Control Systems Symposium*, vol. 16, 2022, ISSN: 2631-8741. DOI: `10.24868/10727`. [Online]. Available: `https://repository.tudelft.nl/islandora/object/uuid%3Ab3dc1792-0cc5-412c-ba9d-6336cfc619b9`.

[93] N. G. C. Astrath et al., "The effect of relative humidity on binary gas diffusion," eng, *The Journal of Physical Chemistry. B*, vol. 113, no. 24, pp. 8369–8374, Jun. 2009, ISSN: 1520-6106. DOI: `10.1021/jp900796w`.

[94] H. I. Geisler, "Finite Element Method (FEM) Model and Performance Analysis of Solid Oxide Fuel Cells," de, Ph.D. dissertation, Fakultät für Elektrotechnik und Informationstechnik – Institut für Werkstoffe der Elektrotechnik (IWE), 2019, ISBN: 9783731508953. DOI: `10.5445/KSP/1000090508`. Accessed: Jan. 21, 2025. [Online]. Available: `https://publikationen.bibliothek.kit.edu/1000090508`.

[95] M. Kornely, "Elektrische Charakterisierung und Modellierung von metallischen Interkonnektoren (MIC) des SOFC-Stacks," de, Ph.D. dissertation, Karlsruher Institut für Technologie, 2012, ISBN: 9783866448339. DOI: `10.5445/KSP/1000027170`. Accessed: Jul. 10, 2025. [Online]. Available: `https://publikationen.bibliothek.kit.edu/1000027170`.

[96] E. M. Greitzer, *Internal Flow: Concepts and Applications*. Cambridge: Cambridge University Press, 2004. [Online]. Available: `https://www.cambridge.org/core/product/14285A6FF068386CF4A1EBBA835319DE`.

[97] T. Fukumoto et al., "Exchange current density of reversible solid oxide cell electrodes," *International Journal of Hydrogen Energy*, vol. 47, no. 37, pp. 16 626–16 639, 2022, ISSN: 0360-3199. DOI: `10.1016/j.ijhydene.2022.03.164`.

[98] S. Ueguchi, M. Kishimoto, and H. Iwai, "Quantitative evaluation of exchange current density in Ni-YSZ patterned electrode in SOCs using oxygen isotope water," *Journal of Power Sources*, vol. 629, p. 235 890, Feb. 2025, ISSN: 0378-7753. DOI: `10.1016/j.jpowsour.2024.235890`. Accessed: Feb. 18, 2025. [Online]. Available: `https://www.sciencedirect.com/science/article/pii/S0378775324018421`.

[99] K. P. Ong, P. Wu, L. Liu, and S. P. Jiang, "Optimization of electrical conductivity of LaCrO3 through doping: A combined study of molecular modeling and experiment," *Applied Physics Letters*, vol. 90, no. 4, p. 044 109, Jan. 2007, ISSN: 0003-6951. DOI: `10.1063/1.2431780`. Accessed: Feb. 3, 2025. [Online]. Available: `https://doi.org/10.1063/1.2431780`.

[100] Comsol. "Heat transfer coefficients — internal natural convection. "[Online]. Available: `https://doc.comsol.com/5.5/doc/com.comsol.help.heat/heat_ug_theory.07.77.html#559203`.

[101] J. W. Slater. "Examining spatial (grid) convergence," NPARC Alliance. [Online]. Available: `https://www.grc.nasa.gov/WWW/wind/valid/tutorial/spatconv.html`.

[102] S. P. S. Badwal, S. Giddey, C. Munnings, and A. Kulkarni, "Cheminform abstract: Review of progress in high temperature solid oxide fuel cells," *ChemInform*, vol. 46, no. 31, 2015, ISSN: 0931-7597. DOI: `10.1002/chin.201531316`. [Online]. Available: `https://doi.org/10.1002/chin.201531316`.

[103] J. Wei, *Mechanical Characterization of Solid Oxide Fuel Cells and Sealants*, en. Forschungszentrum Jülich GmbH, 2016, ISBN: 978-3-95806-266-5.

[104] N. A. Baharuddin, A. Muchtar, A. B. Sulong, and H. Abdullah, "Fabrication methods for planar solid oxide fuel cells: A review," *Advanced Materials Research*, vol. 662, pp. 396–401, 2013, ISSN: 1662-8985. DOI: `10.4028/www.scientific.net/AMR.662.396`. [Online]. Available: `https://www.scientific.net/AMR.662.396`.

[105] AiResearch, "Monolithic solid oxide fuel cell technology advancement for coal- based power generation. quarterly report, december 1991," English, Tech. Rep., 1992. [Online]. Available: `https://www.osti.gov/biblio/10162432`.

[106] K. S. Howe, G. J. Thompson, and K. Kendall, "Micro-tubular solid oxide fuel cells and stacks," *Journal of Power Sources*, vol. 196, no. 4, pp. 1677–1686, 2011, ISSN: 0378-7753. DOI: `10.1016/j.jpowsour.2010.09.043`, K. Kendall, "Progress in microtubular solid oxide fuel cells," en, *International Journal of Applied Ceramic Technology*, vol. 7, no. 1, pp. 1–9, 2010, ISSN: 1744-7402. DOI: `10.1111/j.1744-7402.2008.02350.x`.

[107] G. J. la O' , B. Yildiz, S. McEuen, and Y. Shao-Horn, "Probing oxygen reduction reaction kinetics of sr-doped lamno3 supported on y2o3-stabilized zro2 : Eis of dense, thin-film microelectrodes," *Journal of The Electrochemical Society*, vol. 154, no. 4, B427, 2007, ISSN: 1945-7111. DOI: `10.1149/1.2508887`. [Online]. Available: `https://dx.doi.org/10.1149/1.2508887`.

[108] S. Paydar, M. H. Shariat, and S. Javadpour, “Investigation on electrical conductivity of LSM/YSZ8, LSM/Ce0.84Y0.16O0.96 and LSM/Ce0.42Zr0.42Y0.16O0.96 composite cathodes of SOFCs,” *International Journal of Hydrogen Energy*, vol. 41, no. 48, pp. 23 145–23 155, Dec. 2016, ISSN: 0360-3199. DOI: 10.1016/j.ijhydene.2016.10.092. Accessed: Mar. 20, 2025. [Online]. Available: https://www.sciencedirect.com/science/article/pii/S036031991630194X.

[109] C.-C. T. Yang, W.-C. J. Wei, and A. Roosen, “Electrical conductivity and microstructures of La0.65Sr0.3MnO3 – 8 mol% yttria-stabilized zirconia,” *Materials Chemistry and Physics*, vol. 81, no. 1, pp. 134–142, Jul. 2003, ISSN: 0254-0584. DOI: 10.1016/S0254-0584(03)00158-5. Accessed: Jun. 10, 2025. [Online]. Available: https://www.sciencedirect.com/science/article/pii/S0254058403001585.

[110] Y. Ji, J. A. Kilner, and M. F. Carolan, “Electrical properties and oxygen diffusion in yttria-stabilised zirconia (YSZ) – La0.8Sr0.2MnO3± δ (LSM) composites,” *Solid State Ionics*, vol. 176, no. 9, pp. 937–943, Mar. 2005, ISSN: 0167-2738. DOI: 10.1016/j.ssi.2004.11.019. Accessed: Jun. 10, 2025. [Online]. Available: https://www.sciencedirect.com/science/article/pii/S016727380400894X.

[111] J. Cohn and J. Neumeier, “Local lattice distortions and thermal transport in perovskite manganites,” *Physical Review B - Condensed Matter and Materials Physics*, vol. 56, no. 14, R8495–R8498, 1997. DOI: 10.1103/PhysRevB.56.R8495.

[112] T. Nishikawa, D. Ogawa, S. Honda, and H. Awaji, “作動温度下での多孔質ランタンストロンチウムマンガナイトの機械的および電気的特性,” Japanese, **材料**, vol. 52, no. 6, pp. 587–591, 2003. DOI: 10.2472/jsms.52.587.

[113] B. de Boer, “Sofc anode: Hydrogen oxidation at porous nickel and nickel/zirconia electrodes,” English, PhD Thesis - Research UT, graduation UT, University of Twente, Netherlands, Oct. 1998, ISBN: 9036511909.

[114] O. Marina et al., “Electrode performance in reversible solid oxide fuel cells,” *Journal of The Electrochemical Society*, vol. 154, B452–B459, 2007. DOI: 10.1149/1.2710209.

[115] A. He, J. Gong, J. Onishi, and N. Shikazono, “Three-dimensional topology optimization of Ni-YSZ anode for solid oxide fuel cells via multiphase level-set method,” *Nano Energy*, vol. 103, p. 107 817, Dec. 2022, ISSN: 2211-2855. DOI: 10.1016/j.nanoen.2022.107817. Accessed: Jul. 10, 2025. [Online]. Available: https://www.sciencedirect.com/science/article/pii/S2211285522008941.

[116] H. Shi, C. Su, R. Ran, J. Cao, and Z. Shao, “Electrolyte materials for intermediate-temperature solid oxide fuel cells,” *Progress in Natural Science: Materials International*, vol. 30, no. 6, pp. 764–774, 2020, ISSN: 1002-0071. DOI: 10.1016/j.pnsc.2020.09.003.

[117] K. W. Schlichting, N. P. Padture, and P. G. Klemens, “Thermal conductivity of dense and porous yttria-stabilized zirconia,” en, *Journal of Materials Science*, vol. 36, no. 12, pp. 3003–3010, Jun. 2001, ISSN: 1573-4803. DOI: 10.1023/A:1017970924312. Accessed: Jun. 10, 2025. [Online]. Available: https://doi.org/10.1023/A:1017970924312.

[118] T. Shimonosono, T. Ueno, and Y. Hirata, “Mechanical and thermal properties of porous yttria-stabilized zirconia,” *Journal of Asian Ceramic Societies*, vol. 7, no. 1, pp. 20–30, Jan. 2019, ISSN: null. DOI: 10.1080/21870764.2018.1547248. Accessed: Jul. 21, 2025. [Online]. Available: https://doi.org/10.1080/21870764.2018.1547248.

[119] D. Udomsilp et al., “Metal-supported solid oxide fuel cells with exceptionally high power density for range extender systems,” *Cell Reports Physical Science*, vol. 1, no. 6, p. 100 072, 2020, ISSN: 2666-3864. DOI: 10.1016/j.xcrp.2020.100072.

[120] A. Spekreijse, “Solid oxide fuel cell modeling,” M.S. thesis, Delft University of Technology, 2023. [Online]. Available: `https://repository.tudelft.nl/record/uuid:112cc0fa-2299-46c5-9bb0-fdac67ce02a2`.

[121] A. van de Wetering, *Goose (geometric oxide-cell operating-point simulation environment)*, version 1.0.0, Nov. 2025. DOI: `10.4121/f956617c-aaca-486d-ac85-8d4bb4d3c66b`. [Online]. Available: `https://codeberg.org/aidavdw/goose-sofc`.

A

Using GOOSE

The GOOSE software is published as open source software. It is accessible on the repository at `https://codeberg.org/aidavdw/goose-sofc` [121].

A.1. Interaction and Integration

Geometric Oxide-cell Operating-point Simulation Environment (GOOSE) is designed to be easily integrated into any workflow. Not everyone will use Rust, nor will they have the Rust toolchain installed. To this end, the main way to use the software is through an Application Programming Interface (API), which functions as an interface through various languages. At the time of writing, three such bindings are made for the Python- Rust and C languages respectively.

The API exposes data types, as well as functions to communicate and transform into a data format that GOOSE can use.

Examples of how to use GOOSE can be found in the source repository for the Rust and Python bindings.

A.2. The Mesher

Meshes in GOOSE are a hybrid of conventional grid-based and graph-based. As such, tooling was created to help construct such meshes. The general workflow revolves around defining vertices, between which edges are created. The actual structure parameters exists on these edges, which will be subdivided into elements.

The mesher is implemented using the factory pattern; you create a `MeshMaker`, which has functions to add new vertices, elements, or set coincidence. When done, this `MeshMaker` can construct a fully formed mesh.

Vertices are set as a coordinate with a label. These do not truly exist in the final mesh, but are still stored for ease of identification. They only function to help instantiating edges.

Edges are where are the information is stored. An edge can be a PEN or a CC, which will then be subdivided into n elements, whose neighbours are dynamically set. For the outermost two elements, additional neighbours are set based on what other edges touch the vertex.

In addition to the main two types of edges, variants on the PEN to compensate for component overlap are also available: a dead PEN variant for the anode side, cathode side, and both sides. These components do not partake in any reaction, but they do transmit heat and current like a

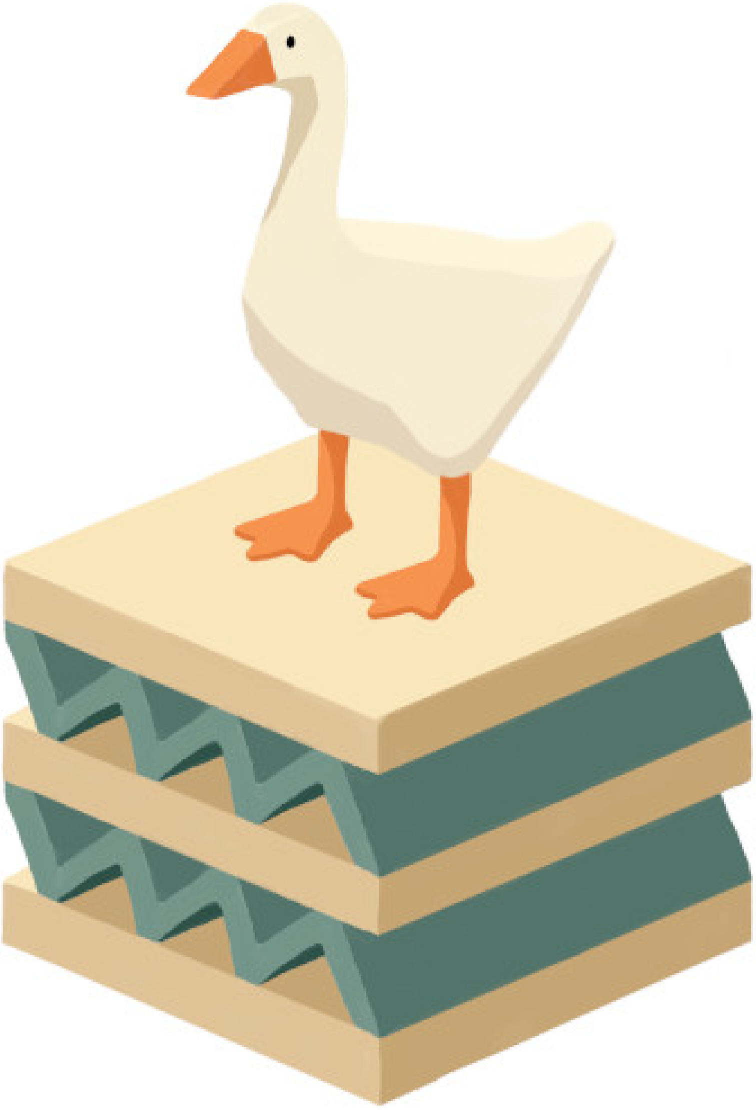

Figure A.1: The logo for the GOOSE software, depicting a member of a certain bird species on top of a part of a mesh of a corrugated monolithic SOFC

normal PEN would.

Handling cyclic boundary conditions is done by setting vertices to be coinciding. If vertex A is coincident to vertex B, Any element connected to vertex A will also be connected to all elements connected to vertex B.

As a final remark: The mesh created by a `MeshMaker` is still not initialised, so it needs to be transformed by an initialisation function before it can be solved.

A.3. Inputs

This section gives an overview of all the inputs that are required in addition to the mesh described in section A.2 to set up a simulation case using GOOSE.

A.3.1. Operational Conditions

First, you need to define your operational conditions. These are contained in `OperationalConditions`, whose contents are the following:

1. Target cell voltage. As described in the introduction of section 2.6, this model requires a target cell potential to be chosen, and not a current density.
2. for every fluid present in the mesh, an inflow condition needs to be given. These are in the form of subsection A.3.4

A.3.2. Model Parameters

A lot of control is given to the invoker on how the solving is to be performed. Settings related to this are retained in `ModelParameters`. All of the values here also have default values that can be used, but to optimise runtime users are encouraged to tweak them.

1. Convergence criterion for overall convergence. If all the deltas are within this margin, the simulation is considered finished, and the result is returned. Its default value is 1×10^{-5}.
2. the maximum amount of iterations that the high-level solver is allowed to take. Iterations are disjoint and very fast, so this number can be very high. The default is $50\,000$ iterations.
3. Root finding settings for the electrochemical model.
4. Root finding settings for the thermal model.
5. Root finding settings for the fluid model.

The root finding settings for the sub-models are all instances described in subsection A.3.3.

At the time of writing, the settings for `knudsen_model` and `diffusion_coefficient_model` do not do anything. In previous versions of the program, the user could also choose the methods used to calculated the Knudsen and binary diffusion coefficients. This functionality has since been integrated, but the option is still exposed so that different methods can again be implemented at a later point and directly exposed.

A.3.3. Root Finder Solver

The general-use root-finder as described in subsection 2.13.4 requires four inputs (in addition to a univariate single function to solve):

1. Convergence criterion: If the relative change with the previously found value is smaller than this criterion, the root is considered found. This defaults to a value of 1×10^{-6}.
2. The maximum amount of iterations that the root-finder is allowed to take. This is equal to the amount of function evaluations after the initial setup, which requires an additional two function evaluations. The default value for this is 50.
3. A lower bound.
4. An upper bound.

A.3.4. Fluid Mixture

There are multiple ways to construct fluid mixtures, but the most important one is based on mole fractions.

1. Static pressure.
2. Temperature.
3. oxygen mole fraction (0-1).
4. nitrogen mole fraction (0-1).

5. water mole fraction (0-1).
6. hydrogen mole fraction (0-1).
7. Cross-sectional area of the fluid section. It is planned to calculated this from the mesh, but right now this still needs to be input manually.

A.3.5. Electrode Material

Both anode and cathode get their material data in the same format.

The material data relating to the porous structure are handled as constants.

1. Mean pore diameter, describing the size of the cavities in the porous medium.
2. Tortuosity, a value describing the indirectness of the path taken by particles diffusing into the porous medium.
3. Porosity, which is the ratio of empty space to solid material.
4. Charge transfer coefficient, with its own datatype as written in subsection 2.13.6.

The following material characteristics can be parametrised using the `EmpiricalFunction` method described in subsection 2.13.6.

1. Exchange current density.
2. Electric conductivity.
3. Thermal conductivity.
4. Contact resistivity at the current collector - electrode interface.

A.3.6. Electrolyte Material

Only two material parameters are required. Both are implemented as an `EmpiricalFunction`.

- The ionic conductivity.
- Thermal conductivity.

A.3.7. Current Collector Material

Again, a mere two material parameters are required. Both are implemented as an `EmpiricalFunction`.

- The electrical conductivity.
- Thermal conductivity.

A.4. Outputs

This section details what exactly you can expect as an output from the GOOSE model. Firstly, there are some system-level quantities. These are integral quantities, used for integrating the entire stack with the environment.

1. Current delivered, which in combination with the voltage returns to total electrical power.
2. Total heat to the environment through conduction.
3. The outflow fluids, in the same format as subsection A.3.4.

Output of the state is available per element.

1. Breakdown of the cell voltage and all the individual overpotentials as given in. subsection 2.6.2
2. Current density.
3. Local TBP specie presence.

4. All the terms in its heat balance.

The fluids in every z-slice are also individually inspectable, again as per subsection A.3.4.

In addition to the outputs mentioned so far, the model gives logs which can be inspected for more intermediate model values, as well as a convergence history.

A.4.1. Polarisation Curves

Equation 2.7 has a degree of freedom: for any given current density j, a solution with an overpotential η_{act} exists. The power extracted is the product of the cell voltage and the current density. This means that in this solution space, a combination of the two with the highest power point can be chosen. For this reason, a *polarisation curve* (alternatively found in literature as I-V curve or I-U curve) is often generated to get an idea of the performance of a fuel cell. In a polarisation curve, the cell voltage is given for any current density drawn. As these curves are most often used to describe entire stacks, I is just the current density multiplied with the active surface area to get an extensive property instead of a cell-size independent j.

It is important to realise that the actual performance of a fuel cell is dependent on many factors: the temperature, the local species concentration, etc. A single polarisation curve contains information for exactly one operating condition. By considering the performance of a fuel cell as a single polarisation curve, all these operational parameters are implicitly assumed. Aside from operating conditions, the polarisation curve also obfuscates sizing and geometrical information. The operating conditions and species concentration are not uniform inside of a fuel cell. Finally, the cell can contain spots of highly varying temperature, as well as gradients in concentration of the reacting species along the flow path as fuel is used up. The polarisation curve holds for one cell, but it describes a solution for the integrand reaction taking place over the active surface area. By changing the size of the cell, the integrand operation conditions change, and hence the performance may also change.

Caution is warranted when representing a fuel cell with polarisation curves. A fuel cell can only be realistically represented by a polarisation curve if the polarisation curve is generated for the same operating conditions and the same geometry as the conditions that is is being interpreted for.

In using GOOSE, one must pick the operating point specifically, which includes the desired cell voltage. For this reason, GOOSE does not directly output a polarisation curve, but one can simply create a script that evaluates a mesh at different desired voltages to construct one.

B

Mixture Specie Properties

Table B.1: Thermal conductivity of water as a function of temperature. Data obtained from `https://www.engineeringtoolbox.com/water-liquid-gas-thermal-conductivity-temperature-pressure-d_2012.html`, extended using RefProp.

Temperature K	Thermal conductivity κ $\mathrm{W\,m^{-1}\,K^{-1}}$
373.15	0.02457
398.15	0.02666
423.15	0.02883
448.15	0.03109
473.15	0.03343
498.15	0.03585
523.15	0.03834
548.15	0.04091
573.15	0.04353
623.15	0.04898
673.15	0.05465
723.15	0.06052
773.15	0.06658
823.15	0.07281
873.15	0.07917
973.15	0.09228
1073.15	0.10581
1173.15	0.11967
1300.00	0.13800
1400.00	0.15200
1500.00	0.16700
1600.00	0.18100

Table B.2: Dynamic viscosity of water as a function of temperature. Data from Coolprop.

Temperature K	Dynamic viscosity μ $\mathrm{Pa\,s}$
600	2.143×10^{-5}
1200	4.519×10^{-5}

Table B.3: Thermal conductivity of hydrogen as a function of temperature. Data obtained from `https://www.engineeringtoolbox.com/hydrogen-H2-thermal-conductivity-temperature-pressure-d_2106.html`, extended using RefProp.

Temperature K	Thermal conductivity κ $\mathrm{W\,m^{-1}\,K^{-1}}$
100	0.0683
200	0.1324
300	0.1858
400	0.2331
500	0.2751
600	0.3176
700	0.3608
800	0.4047
900	0.4492
1000	0.4943
1100	0.5000
1200	0.5400
1300	0.5810
1400	0.6220
1500	0.6640

Table B.4: Dynamic viscosity of hydrogen as a function of temperature. Data from Coolprop.

Temperature K	Dynamic viscosity μ $\mathrm{Pa\,s}$
600	1.447×10^{-5}
1200	2.358×10^{-5}

Table B.5: Thermal conductivity of oxygen as a function of temperature. Data obtained from `https://www.engineersedge.com/heat_transfer/thermal-conductivity-gases.htm` and RefProp.

Temperature K	Thermal conductivity κ $\mathrm{W\,m^{-1}\,K^{-1}}$
100	0.0093
200	0.0184
300	0.0263
400	0.0337
500	0.0410
600	0.0481
700	0.0540
800	0.0600
900	0.0659
1000	0.0715
1100	0.0771
1200	0.0825
1300	0.0878
1400	0.0930
1500	0.0982
1600	0.1030

Table B.6: Dynamic viscosity of oxygen as a function of temperature. Data from Coolprop.

Temperature K	Dynamic viscosity μ $\mathrm{Pa\,s}$
600	3.473×10^{-5}
1200	5.534×10^{-5}

Table B.7: Thermal conductivity of nitrogen as a function of temperature. Data from `https://www.engineeringtoolbox.com/nitrogen-N2-thermal-conductivity-temperature-pressure-d_2084.html` and RefProp.

Temperature K	Thermal conductivity κ $\mathrm{W\,m^{-1}\,K^{-1}}$
373	0.03104
398	0.03269
423	0.03430
448	0.03587
473	0.03742
573	0.04332
623	0.04613
673	0.04886
773	0.05414
800	0.05551
900	0.06052
1000	0.06536
1100	0.07016
1200	0.07470
1300	0.07920
1400	0.08360
1500	0.08800
1600	0.09240

Table B.8: Dynamic viscosity of nitrogen as a function of temperature. Data from Coolprop.

Temperature K	Dynamic viscosity μ $\mathrm{Pa\,s}$
600	2.958×10^{-5}
1200	4.677×10^{-5}

Table B.9: Constant thermophysical properties of selected fluid species.

Property	Water	Hydrogen	Oxygen	Nitrogen
Lennard-Jones potential over Boltzmann ε/k [61]	$809.1\,\mathrm{K}$	$59.7\,\mathrm{K}$	$106.7\,\mathrm{K}$	$71.4\,\mathrm{K}$
Lennard-Jones characteristic length σ [61]	$2.641\,\text{Å}$	$2.827\,\text{Å}$	$3.467\,\text{Å}$	$3.798\,\text{Å}$
Molar mass M	$18.015\,28\,\mathrm{g\,mol^{-1}}$	$2.015\,88\,\mathrm{g\,mol^{-1}}$	$31.998\,80\,\mathrm{g\,mol^{-1}}$	$28.013\,40\,\mathrm{g\,mol^{-1}}$
Prandtl number Pr [1]	0.915	0.676	0.744	0.73

[1] The values obtained for temperatures between $600\,\mathrm{K}$ and $1100\,\mathrm{K}$ as reported by Coolprop were averaged. A constant Prandtl number is a commonly used assumption in thermofluid simulations [79].

Parameter Matrices

Table B.10: Parameter study data raw data for the ribbed planar geometry

Param	Value	PEN temperature K			current density $\mathrm{A\,cm^{-2}}$			u_f	P	Unit area
		min.	avg.	max.	min.	avg.	max.		W	mm^2
ref	-	1021.8	1036.9	1047.8	0.161	0.1907	0.2113	0.071	0.09311	8.9
h_f	1.65	1021.28	1036.5	1047.32	0.1598	0.1902	0.2113	0.067	0.093	9.275
h_f	1.8	1020.76	1036.04	1046.82	0.1586	0.1896	0.2111	0.061	0.0929	9.65
h_f	1.35	1022.28	1037.33	1048.19	0.1621	0.1909	0.2108	0.082	0.09354	8.525
h_f	1.2	1022.77	1037.7	1048.56	0.1632	0.1908	0.2099	0.092	0.09352	8.15
h_a	1.65	1020.75	1035.68	1046.29	0.1585	0.1876	0.2076	0.072	0.09191	9.275
h_a	1.8	1019.74	1034.38	1044.72	0.1561	0.1843	0.2037	0.071	0.09032	9.65
h_a	1.35	1022.84	1038.12	1049.17	0.1635	0.1936	0.2147	0.075	0.09486	8.525
h_a	1.2	1023.91	1039.23	1050.46	0.116	0.1963	0.2177	0.076	0.9617	8.15
s_r	2.75	1020.39	1036.18	1047.6	0.1576	0.1891	0.2114	0.071	0.09926	9.79
s_r	3	1019.01	1035.35	1047.3	0.1543	0.1872	0.211	0.069	0.10484	10.68
s_r	2.25	1023.22	1037.61	1047.84	0.1645	0.192	0.2108	0.076	0.8737	8.01
s_r	2	1024.67	1038.23	1047.81	0.168	0.1932	0.2099	0.0798	0.08113	7.12
τ_r	1.1	1021.77	1037.22	1048.36	0.1609	0.1912	0.2124	0.0758	0.09638	8.9
τ_r	1.2	1021.75	1037.52	1048.96	0.1608	0.1918	0.2136	0.0782	0.09935	8.9
τ_r	0.9	1021.82	1036.44	1047.2	0.1611	0.1901	0.2102	0.0712	0.09051	8.9
τ_r	0.8	1021.86	1036.37	1046.64	0.1612	0.1896	0.2091	0.0687	0.08761	8.9
χ	11	1021.64	1036.64	1047.34	0.1569	0.1858	0.2057	0.0756	0.09102	8.9
χ	12	1021.5	1036.36	1046.93	0.1531	0.1812	0.2005	0.0778	0.08877	8.9
χ	9	1021.94	1037.23	1047.22	0.1654	0.196	0.2172	0.0714	0.09603	8.9
χ	8	1022.09	1037.55	1048.7	0.1703	0.2017	0.2236	0.0693	0.09884	8.9

Table B.11: Parameter study data raw data for the corrugated monolithic geometry

Param	Value	PEN temperature K			current density $\mathrm{A\,cm^{-2}}$			u_f	P	Unit area	P/A
		min.	avg.	max.	min.	avg.	max.		W	$\mathrm{mm^2}$	$\mathrm{W\,mm^{-2}}$
ref	-	1030.091	1040.087	1048.208	0.1813	0.19549	0.20651	0.0992	0.14844	8.82	16829.93
w_f	0.88	1030.18	1040.151	1048.236	0.18155	0.19548	0.20696	0.0969	0.14768	8.82	16743.76
w_f	0.96	1030.225	1040.21	1048.24	0.18182	0.19619	0.20732	0.0946	0.14697	8.82	16663.27
w_f	0.72	1030.01	1040.049	1048.164	0.18112	0.19513	0.20601	0.1017	0.14924	8.82	16920.63
w_f	0.64	1029.936	1040.006	1048.115	0.18095	0.19477	0.20547	0.1043	0.15009	8.82	17017.01
h_t	2.31	1029.306	1039.843	1048.314	0.17951	0.19526	0.20747	0.09634	0.15844	9.702	16330.65
h_t	2.52	1028.502	1039.566	1048.386	0.17755	0.19489	0.20823	0.0939	0.16846	10.584	15916.48
h_t	1.89	1031.004	1040.356	1047.893	0.18349	0.19562	0.20486	0.1029	0.13855	7.938	17454.02
h_t	1.68	1031.943	1040.611	1047.569	0.18573	0.19558	0.20301	0.1076	0.1288	7.056	18253.97
s_r	1.43	1030.041	1040.103	1048.247	0.18123	0.19549	0.20661	0.0993	0.14858	8.82	16845.8
s_r	1.56	1029.99	1040.12	1048.294	0.18116	0.1955	0.20668	0.0996	0.14898	8.82	16891.16
s_r	1.17	1030.04	1040.13	1048.246	0.18123	0.19549	0.20661	0.0993	0.14858	8.82	16845.8
s_r	1.04	1029.988	1040.119	1048.293	0.18116	0.1955	0.20668	0.0996	0.14898	8.82	16891.16
w_a	0.88	1029.898	1039.979	1048.099	0.18085	0.19513	0.20615	0.1003	0.14715	8.82	16683.67
w_a	0.96	1029.724	1039.865	1047.982	0.18044	0.19477	0.20575	0.1014	0.14591	8.82	16543.08
w_a	0.72	1030.323	1040.226	1048.226	0.18198	0.19585	0.20663	0.0983	0.14979	8.82	16982.99
w_a	0.64	1030.572	1040.361	1048.216	0.18266	0.19621	0.20664	0.0974	0.15119	8.82	17141.72
χ	11	1030.057	1039.995	1048.034	0.1771	0.19103	0.20183	0.1024	0.14506	8.82	16446.71
χ	12	1030.02	1039.897	1047.87	0.17319	0.18686	0.19743	0.1056	0.14189	8.82	16087.3
χ	9	1030.207	1040.213	1048.302	0.18608	0.20028	0.21127	0.0961	0.15208	8.82	17242.63
χ	8	1030.349	1040.342	1048.385	0.19137	0.20547	0.21632	0.093	0.15602	8.82	17689.34

Table B.12: Parameter study data raw data for the tubular geometry

Parameter	Value	PEN temperature K			Current density $\mathrm{A\,cm^{-2}}$			u_f	P	Unit area
		min	avg	max	min	avg	max		W	$\mathrm{mm^2}$
ref	-	1003.492	1012.240	1019.182	0.11971	0.12701	0.13159	0.1407	0.3461	6.76
τ_r	0.66	1003.479	1012.143	1019.055	0.11968	0.12694	0.13147	0.1399	0.3443	6.76
τ_r	0.72	1003.471	1012.081	1018.925	0.11966	0.12687	0.13134	0.1392	0.3424	6.76
τ_r	0.54	1003.511	1012.264	1019.306	0.11976	0.12708	0.13172	0.1414	0.34781	6.76
τ_r	0.48	1003.536	1012.323	1019.426	0.11982	0.12715	0.13186	0.1420	0.34941	6.76
r_t	1.98	1003.416	1013.327	1021.674	0.11968	0.13022	0.13797	0.1273	0.39174	6.76
r_t	2.16	1003.366	1014.607	1024.638	0.11965	0.13363	0.14525	0.1168	0.43979	6.76
r_t	1.62	1003.587	1011.203	1017.024	0.11955	0.12386	0.12634	0.1581	0.30231	6.76
r_t	1.44	1003.703	1010.315	1015.168	0.11625	0.12062	0.12579	0.1814	0.2600	6.76
s_t	2.86	1003.593	1010.981	1016.708	0.11969	0.12483	0.12766	0.1382	0.34003	8.1796
s_t	3.12	1003.752	1010.217	1015.052	0.11951	0.12350	0.12722	0.1366	0.33628	9.7344
s_t	2.34	1003.499	1014.236	1023.107	0.11985	0.13075	0.13838	0.1449	0.35645	5.4756
s_t	2.08	1003.735	1017.896	1029.981	0.12040	0.13779	0.15131	0.1528	0.37580	4.3264
χ	11	1003.939	1011.859	1018.624	0.11665	0.12357	0.12784	0.1445	0.33670	6.76
χ	12	1003.303	1011.543	1018.112	0.11384	0.12039	0.12437	0.1485	0.32814	6.76
χ	9	1003.601	1012.582	1019.793	0.12307	0.13076	0.13567	0.1369	0.35627	6.76
χ	8	1003.723	1012.999	1020.467	0.12679	0.13478	0.14013	0.1331	0.36743	6.76

C

Validation at very high resolution mesh

Re-running the validation procedures at much higher resolution shows that the results achieved in Su et al. [32] are most likely not fully resolved.

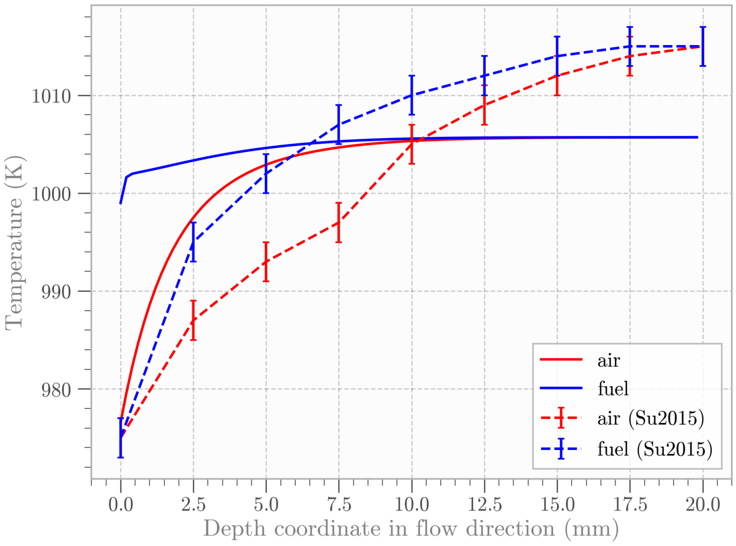

(a) Fluid temperatures (air and fuel) presented in Su et al. [32] and this model, run at a high resolution mesh (40000 nodes)

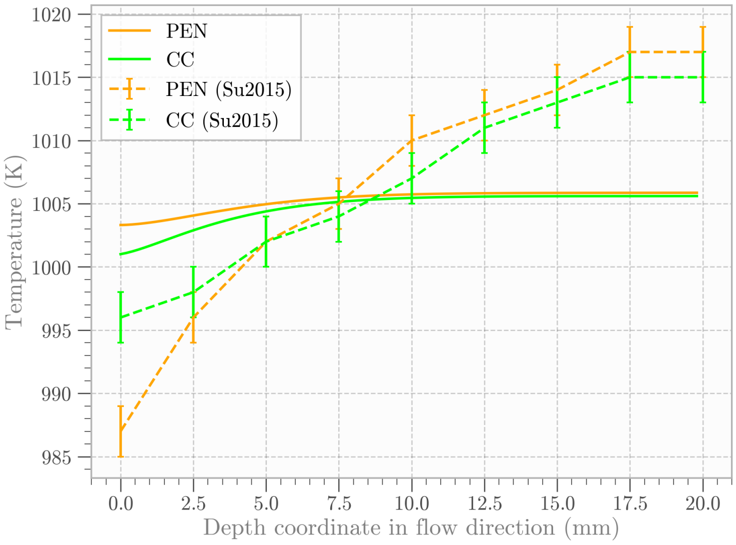

(b) Temperatures of solids (PEN and CC)

Figure C.1: Comparison of the temperature trend along the flow path calculated by the model in this work run at a high resolution mesh (40000 nodes), as compared to that in Su et al. [32].

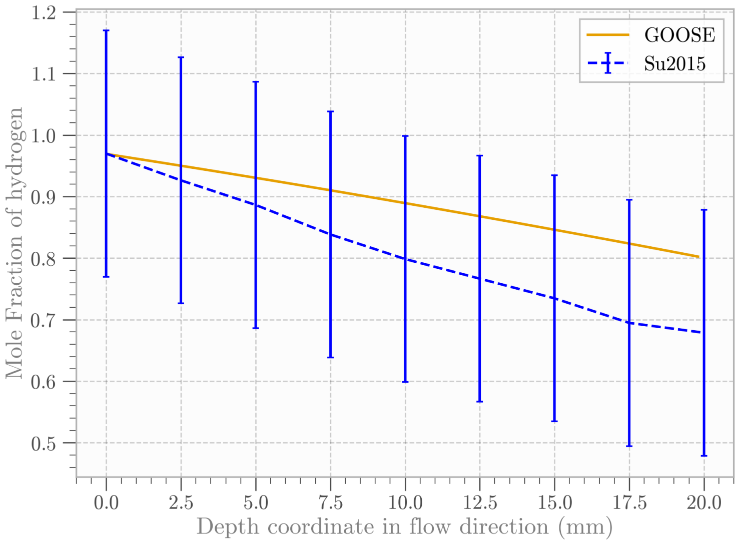

Figure C.2: Comparison of the hydrogen fraction of the bulk flow along the flow path as calculated by this model run at a high resolution mesh (40000 nodes), and as reported in Su et al. [32].